UNIVERSITEIT VAN PRETORIA
UNIVERSITY OF PRETORIA
YUNIBESITHI YA PRETORIA
Denkleiers • Leading Minds • Dikgopolo tša Dihlalefi

EFFECT OF MOULD FLUX ON SCALE ADHESION TO REHEATED STAINLESS STEEL SLABS

By

Ndiabintu Mukadi Jean-Jacques

Submitted in partial fulfilment of the requirements for the degree

Master of Applied Science

(Metallurgical)

Department of Materials Science and Metallurgical Engineering,
Faculty of Engineering, Built Environment and Information Technology,
University of Pretoria, South Africa

Supervisor: Professor P.C. Pistorius

2008

UNIVERSITEIT VAN PRETORIA
UNIVERSITY OF PRETORIA
YUNIBESITHI YA PRETORIA

TITLE: EFFECT OF MOULD FLUX ON SCALE ADHESION TO REHEATED STAINLESS STEEL SLABS

STUDENT: NDIABINTU MUKADI JEAN-JACQUES

NUMBER: 25494555

DEGREE: MASTER OF APPLIED SCIENCE (METALLURGY)

DEPARTMENT: DEPARTMENT OF MATERIALS SCIENCE AND METALLURGICAL ENGINEERING, FACULTY OF ENGINEERING, BUILT ENVIRONMENT AND INFORMATION TECHNOLOGY

UNIVERSITY: UNIVERSITY OF PRETORIA,
SOUTH AFRICA

SUPERVISOR: PROF. P.C. PISTORIUS

STUDY YEAR: 2006-2008

ABSTRACT

Effects of mould flux contaminant on scale-steel adhesion and hydraulic descaling of scale formed on slabs were investigated. In this investigation, stainless steel type 304 (austenitic with 18% Cr and 8% Ni) and specific mould fluxes were used when growing the scale on contaminated samples under simulated industrial reheating conditions, with subsequent high pressure water hydraulic descaling.

The basic hypothesis was that the steel-scale adhesion depends on the microstructure of different phases present in the scale, the segregation of specific elements at the interface and the interfacial morphology of the scale after reheating.

It was found that mould flux contaminant decreases scale-steel adhesion and therefore improved the descaling effectiveness significantly compared to non contaminated stainless steel.

The descaling effectiveness of contaminated and uncontaminated slab was dependent to the presence of metal free paths (chromite layers along the austenite grains boundaries) and the presence of unoxidized metal in the scale due to nickel enrichment at the interface.

Compared to the uncontaminated samples, the descaling of contaminated samples was efficient which could be due to the fact that some mechanisms which increase scale–steel adhesion (notably nickel enrichment at the interface) were considerably reduced.

For all contaminated samples, the descaling effectiveness after visual observation were close to 100% and it was found that mould flux type 832 (low basicity) gave a high descaling efficiency with better steel surface quality after descaling compared to mould fluxes type 810 and RF1.

Key words: Stainless steel, mould flux, reheating, hydraulic descaling, internal oxidation, chromite, scale, tendrils of nickel-rich filigree, austenite grain boundaries, interfacial morphology, free oxygen

AKNOWLEDGEMENTS

I would like to express my sincere gratitude to my supervisor Prof. P.C. Pistorius for identifying the project, his valuable directions, suggestions, discussions and continuous encouragement during our investigations.

I would also like to express my gratitude to Columbus Stainless for providing financial and material support of the project.

I am greatly indebted to Mr. Carel Coetzee for his assistance during all experimental running and for scanning electron microscope analysis (SEM).

I am grateful to all professors and personnel of the Department of Materials Science and Metallurgical Engineering and IMMRI, especially Prof. Tom von Moltke, Marius Biermann and Albert Venter, for their friendly support and help with X-ray photo-electron spectroscopy.

Thanks also to Dr. Sabine Verryn (XRD) and Mrs Maggi Loubser (XRF), both of the Department of Geology, for their help with the X-ray analysis and discussions during the experimental work.

I wish to thank gratefully my brothers Richard Kady, Kabwika Bodouin, Eric Mujanayi, Olivier Kabengele, Freddy Kayembe and my wife Mukadi Ntumba Veronique for their unconditional support during the project.

I would like to finish in expressing thanks and gratitude to all colleagues and friends who directly or indirectly helped me in preparing this dissertation. Special thanks to Philippe Maweja, Michel Lonji, Daudet Tshikele, Alain Mwamba, Faustin Kalenda and Ghislain Tshilombo; they were omnipresent during the completion of this dissertation, to such an extent that I do not have words to express my gratitude towards them.

DEO GLORIA

TABLE OF CONTENTS

LIST OF FIGURES

LIST OF TABLES

NOMENCLATURE

Symbol

ΔG^o	Gibbs free energy change under standard conditions (J/mol)
M	Metal
MO	The lowest oxide of the metal M
P_{O_2}	Oxygen partial pressure (Atmosphere – atm)
SEN	Submerged Entry Nozzle
X_{Fe}	Molar fraction of Iron
X_{Cr}	Molar fraction of Chromium
X_{Ni}	Molar fraction of Nickel
X_{CaO}	Molar fraction of calcium oxide
X_{SiO2}	Molar fraction of silicon dioxide
I	Maximum jet impact pressure (N/mm^2)
SP	System pressure (Pascal - Pa)
T	Temperature (Kelvin - K)
K_p	Parabolic rate constant (kg^2/m^4s)
R	Gas constant
Q	Water flow rate (litres/min)
t	Time (hour - h)
v	Speed of steel under jet (m/s)
m_i	Slab steel mass before reheating(Kg)
m_a	Slab steel mass after reheating(Kg)
m_F	Mass of mould flux powder (Kg)
f_l	Average thickness of the liquid flux film in the mould (m)
S_s	Slab steel surface (m^2)
e	Slab steel thickness (m)
Δm	Mass variation of the slab after reheating (Kg)
Gm	Gain of sample weight after reheating (Kg/m^2)
C_f	Surface concentration of mould flux on the sample surface (g/cm^2)
B_S	Slag basicity in steelmaking

B_F	Basicity of mould powder
P_r	Dry air regulator pressure (Pa)
P1s	Pressure at the first digital transmitter (%)
P1	Pressure at the first digital transmitter (Pa)
P2s	Pressure at the second digital transmitter (%)
P2	Pressure at the second digital transmitter (Pa)
ΔPs	Difference in pressure between two digital transmitters (%)
ΔP	Difference in pressure between two digital transmitters (Pa)
Qt	Water flow rate measured at the first transmitter (l/min)
Qb	Water flow rate measured at the second transmitter (l/min)
Qav	Average water flow rate (l/min)
P_s	Powder consumption per unit area of mould (kg/m^2)
P_t	Powder consumption per steel mass (kg/Tonne of steel)
f	Fraction of the powder producing slag.
R_m	Ratio of surface area to volume of the cast profile
e_m	Width of the mould (m)
l_m	Thickness of the mould (m)
A	Jet length (m)
B	Jet width (m)
D	Overlap (m)
E	Nozzle distance (m)
H	Distance from mid-spray beam to lower edge of strip (m)
S	Strip thickness (m)
d	Outer diameter of pipe (m)
C	Jet width in jet direction (m)
h_1	Vertical height of nozzle (m)
h_2	Vertical spray height (m)

U	Specific water impingement (litre/m^2)
l	Scale thickness(mm)
Δp	Descaling header pressure (Pa)

Greek symbols

ρ_{flux}	Density of the melted liquid flux (Kg/m^3)
β	Angle of inclination of the descaling Nozzle (º)
α	Nozzle spray angle (º)
γ	Offset angle of nozzle against pipe roll axis (º)
δ	Thermal diffusivity of the scale (m^2/s)

Abbreviations

AES	**A**uger **E**lectron **S**pectroscopy
EDS, EDX	**E**nergy-**D**ispersive **X**-ray **S**pectroscopy
ICP-AES	**I**nductively **C**oupled **P**lasma-**A**tomic **E**mission **S**pectroscope
SEM	**S**canning **E**lectron **M**icroscope
SEM -BSE	**S**canning **E**lectron **M**icroscope **B**ack-**S**cattered **E**lectron
SEM-SEI	**S**canning **E**lectron **M**icroscope **S**econdary **E**lectron **I**mage
SMF	**S**ynthetic **M**ould **F**lux
XRD	**X**-Ray **P**owder **D**iffraction
XRF	**X**-Ray **F**luorescence **S**pectroscopy
XPS	**X**-Ray **P**hotoelectron **S**pectroscopy
FWHM	**F**ull **W**idth **H**alf **M**aximum

Chapter 1: INTRODUCTION

Reheating slabs in an oxidising furnace atmosphere at high temperature is a common step before hot rolling. Since the steel is treated for an extended duration, surface oxidation is inevitable. The resulting oxide scale is hydraulically removed by water sprays at high pressure before hot rolling to ensure good surface quality of the hot-rolled strip.

The product surface quality is strongly linked to the upstream operations such as continuous casting, reheating and descaling before hot rolling (Kizu *et al.,* 2002).
The occurrence of rolled-in-scale defects strongly depends on the adhesion of scales formed on steel surface during reheating, and the residual thin scale after descaling seriously deteriorates surface quality defect in the final product (Kizu *et al*., 2002).

Riquier and Dumortier (1997) reported that the steels (316L, 316LN and 347) that oxidise the most are easily descaled and the steels that oxidised less (304, 304 LN and 321) develop sticky scales with nodules deeply encrusted in the underlying alloy. These nodules cannot be removed by water descaling and generate sliver defects during hot rolling (Riquier & Dumortier, 1997).

Hence for efficient removal of the scale, the effects of the slab surface contaminants on the scale-metal adhesion have to be well understood.

1.1 Background and Motivation

The oxidation of slabs in the reheating furnace is the first and determining process of the scaling of hot rolled flat products. The structure of the scale formed during reheating and the width of the internal oxidation zone are not only influenced by the heating parameters, but also by the chemical composition of the steel (Dénes *et al*., 2003). The primary scale formed on the slab has to be efficiently removed by hydraulic descaling.

Previous studies showed that, under mechanical descaling conditions, the entanglement that arose at the steel-scale interface was in fact effective to maintain steel-scale adhesion. In the case of type 304, descaling proceeds by fracture along chromite layers, which formed on the austenite grain boundaries; for this steel, the extend of descaling depended most strongly on austenite grain structure and the presence of unoxidized metal tendrils at the interface and not primarily on the conditions in the reheating furnace (Pistorius *et al*., 2003).

1.2 Problem Statement

Steel-scale adhesion is expected to be dependent not only on the thickness of the scale but also on the nature of the different phases present in the scale and interfacial morphology of the scale.

The work carried out in this study attempted to:

- Identify and understand possible effects of residual mould flux contamination on the scale-steel adhesion,

1.3. Aims of Investigation

The main aim of this project is to improve the descaling effectiveness of the stainless steel. The study focused on the issue of descaling of reheated slabs, and specifically the possible effects of residual mould flux contaminant on the scale-metal adhesion, because it was found that oxide dispersions on the steel surface may affect phase formation at the interface, mechanical properties of the scale and the interfacial morphology, all of which influence the adhesion between scale and steel (Nagai, 1989).

The approach was hence to contaminate steel surface with mould flux, then grow scale under simulated reheating furnace conditions where temperature, gas atmosphere and mass transfer to the sample surface are controlled; determining the effects of steel composition (alloying elements, impurities on and in the steel) and the effect of reheating conditions on the scale-steel adhesion.

1.4. Approach

The basic hypothesis is that the microstructure of different phases present in the scale, the segregation of specific elements at the interface and the degree of interfacial roughening affect the adhesion between steel and scale and so influence the descaling effectiveness.

The main parameters considered in this study were:

- Reheating conditions (time, temperature and gas atmosphere)
- Descaling parameters (water flow rate, system pressure, nozzle height, water spray angle, stock velocity)

Chapter 2: LITERATURE SURVEY

2.1 THERMODYNAMIC CONSIDERATIONS

2.1.1 Introduction

Reheating before hot rolling is performed in an oxidising atmosphere which forms by reacting fuel with an excess of oxygen, necessary to ensure complete combustion of fuel. Under these conditions surface damage due to oxidation or scaling is inevitable. The oxide layer must be removed before hot rolling.

In order to minimise or prevent surface deterioration and to avoid surface reactions (carburising or nitriding), one possible option is to control the gas composition (Birks & Meier, 1983).

Prevention or control of scale layer formation would then be a question of controlling the oxygen partial pressure to value low enough to avoid the oxidation reactions:

$$M+1/2O_2 = MO;\ \Delta G^\circ \qquad (1)$$

where MO is the lowest oxide of M. The oxygen partial pressure must be controlled so as not to exceed a value:

$$\left(P_{O_2}\right)_{M/MO} = \exp(2\Delta G^\circ / RT) \qquad (2)$$

For stainless steel containing iron, chromium and nickel as a major elements, the followings reactions may be envisaged:

$$Fe + 1/2O_2 = FeO \qquad (3)$$
$$2Cr + 3/2O_2 = Cr_2O_3 \qquad (4)$$
$$Ni + 1/2O_2 = NiO \qquad (5)$$

If we assume that stainless steel type 304 has the composition 18% Cr, 8% Ni and Fe balance (mass basis), the mole fractions of these three elements are X_{Fe}= 0.733, X_{Cr}= 0.192 and X_{Ni}= 0.075.

Taking as a first approximation the activities of Fe, Cr and Ni in the steel to be ideal, and the oxide products to have unit activities, the oxygen pressure at equilibrium can be estimated; the package FactSage was used to perform these calculations, and the results are given in Figure 2.1.

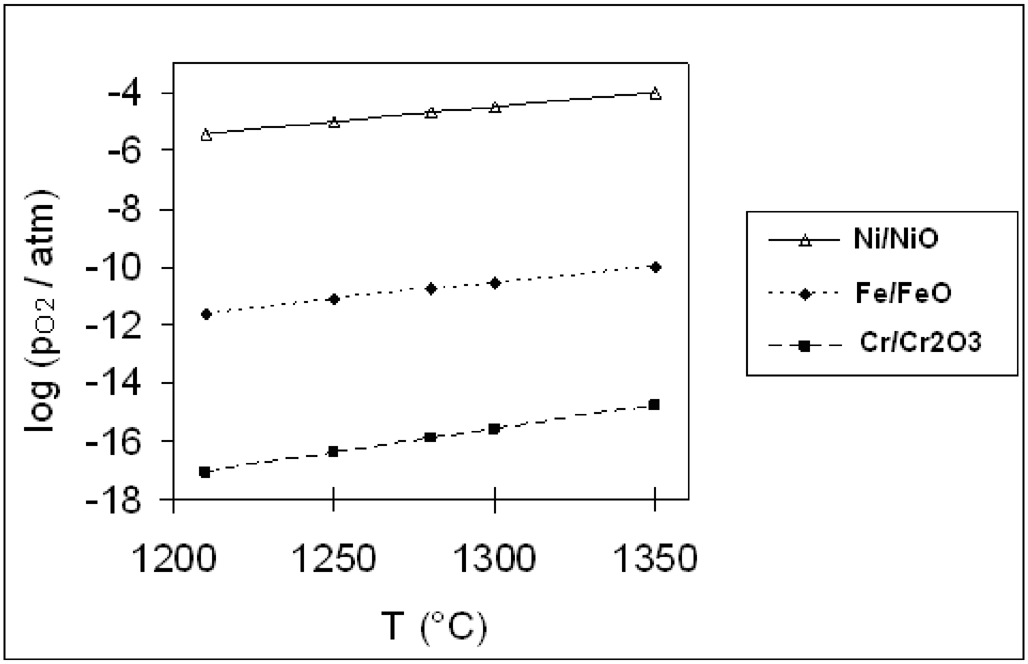

FIGURE 2.1: Variation of the equilibrium oxygen partial pressure with temperature, for the dissociation of iron oxide, chromium oxide and nickel oxide respectively.

It is obvious that the oxygen partial pressures are very low, especially in the case of chromium. To avoid steel surface oxidation, partial oxygen pressure in the furnace atmosphere must be less than 10^{-16} atm which is not realisable for industrial reheating. From the Ellingham diagram for oxides, it is be seen that mould flux oxides such as CaO, MgO, Al_2O_3 and SiO_2 are more stable than are the oxides of iron, nickel and chromium since their equilibrium oxygen potentials are much lower than those of oxide scales under reheating conditions.

However, at reheating temperature, basic mould flux oxides and fluorides (CaF_2, Na_2O and K_2O) may release oxygen and fluorine anions (O^{2-} and F^-) which can influence the oxidation of steel alloying elements (Lee *et al.*, 2002).

Some possible reactions between mould flux and alloying elements under reheating conditions are as follows:

$$Cr_2O_3 + 2CaO + 1.5O_2 = 2CaCrO_4 \quad (6)$$

$$Cr + 1.5O_2 + Na_2O = Na_2CrO_4 \quad (7)$$

$$Ni + 1/2O_2 + O^{-2} = NiO_2^{-2} \quad (8)$$

$$3\ Na_2O + 6\ CaF_2 + Cr_2O_3 = 2Na_3CrF_6 + 6\ CaO \quad (9)$$

$$Na_2O + 3CaF_2 + 2NiO = 2NaNiF_3 + 3\ CaO \quad (10)$$

$$3\ Na_2O + 6\ CaF_2 + Al_2O_3 = 2\ Na_3AlF_6 + 6\ CaO \quad (11)$$

Reactions (6), (7) are solid-gas reactions (Ma & Garbers-Craig, 2005) and reaction (8) is a solid-gas-liquid reaction (Lee *et al.*, 2002).

These reactions may enhance the chromium and nickel oxidation at the interface and in the scale. The chromium oxidation state in the reheating furnace atmosphere can be (+3), (+6) or (0). For stainless steels chromium (+6) is not desired because hexavalent chromium is soluble in water and is hazardous (Ma & Garbers-Craig, 2005). Sano *et al.* (1997) reported that the equilibrium ratio Cr^{6+}/Cr^{3+}increases when the slag basicity increases.

Reactions (9) and (10) seem to be not likely due to the very small amount of mould flux contaminant on the steel surface, and expected fluoride volatilization at high reheating temperature.

At reheating temperatures mould flux components (Na_2O, CaF_2 and Al_2O_3) can melt and form cryolite-alumina according to reaction (11). Jentoftsen *et al.* (2002) noticed that this reaction is likely to happen at high temperature and the melting cryolite-alumina formed may dissolve some transition metal oxides (NiO, FeO) at 1020ºC**.** They also found that the concentration of Fe and Ni in cryolite-alumina melts in equilibrium with solid FeO and NiO decrease when the Al_2O_3 wt% increases. The solubility of iron (1.70wt% for 5.9 wt% Al_2O_3) was higher than that of nickel (0.021wt% for 6.26wt% Al_2O_3).

2.1.2 Mechanisms of Metal-Scale Interfacial Roughening

2.1.2.1 Oxidation of Pure Metals

Pure metals generally oxidize by cationic diffusion mechanism (Kofstad, 1988). Since iron is the major element of steel, the classical scale growth mechanism of iron is briefly reviewed as follows: due to oxidising atmosphere in the furnace iron is oxidized to (Fe^{2+}) at the scale-metal interface, releasing two electrons. The iron ions and electrons migrate outwards through the scale. At the scale-gas interface, the electrons react with oxygen to produce O^{2-} ions, which in turn react with the Fe^{2+} ions to form new FeO.

During high temperature oxidation of iron in air, a muti-layered scale is formed in parallel. This scale consists of wustite, magnetite and haematite (Abuluwefa *et al.*, 1997). For oxidation in high temperature range 700-1250°C, the average FeO/ Fe_3O_4/ Fe_2O_3 thickness ratios are 95:4:1 [(Sheasby *et al.*, 1984), (Ajersch, 1992)]. At lower temperatures (below 570°C), wustite is not stable and magnetite grows at the expense of the wustite (Sheasby *et al.*, 1984).

2.1.2.2 Kinetics of Oxidation

During initial industrial reheating condition of steel, oxygen mass transfer to the outer scale surface controls the rate of scale growth (for small scale thicknesses) since Fe^{2+} ion transfer is relatively efficient. The rate of scale growth is then linear- the thickness of the scale formed is directly proportional to time. The maximum thickness of FeO where this holds varies between 0.4 and 0.5 mm; beyond this thickness the scale growth rate changes from linear to parabolic and the rate- controlling step becomes the arrival of Fe^{2+} at the interface (Sachs & Tuck, 1968). The parabolic rate law can simply be represented by the following equation: $x^2 = k_p t$ (Garber, 1959).

During simulated industrial reheating conditions of the stainless steel type 304, the scale thickness was about 2mm after 6h of reheating. The scale consisted of two layers with similar thicknesses. The inner layer was mainly an iron-chromium spinel layer and the outer layer was mainly an iron oxide layer (Pistorius *et al.*, 2003).

The classic Wagner theory predicts parabolic kinetics for oxidation rate controlled by cationic diffusion mechanism through the scale and good agreement between the calculated and experimental parabolic rate constants is found, for temperatures greater than approximately 0.75 times the absolute melting point of the scale (Rapp, 1984). The parabolic oxidation mechanism should favour the formation of a scale with smooth interfaces and uniform thickness, since the scale grows more rapidly at points where it is locally thinner.

Pieraggi *et al.* (1988) suggested that vacancies are created at the interface metal-scale due to the removal of cations from the metal surface during parabolic oxidation (Pieraggi *et al.*, 1988). They also observed that roughening can occur at the scale-metal interface even in the case of pure metals undergoing parabolic oxidation. As oxidation progresses, there is continual removal of the cations (in the case, Fe^{2+}) at the metal-scale interface, which means that vacancies are continually created. Hirth *et al.* (1995) and Taniguchi (1985) suggested that vacancies are generally eliminated by climb of the misfit or miss-orientation dislocations within the metal formed as a result of the epitaxial relationship generally maintained between the scale and the underlying substrate. [(Hirth *et al.*, 1995), (Tanguchi, 1985)].
Void formation at the interface appears inevitable for the conditions during reheating. The extent of void formation is expected to increase as the extent of scaling increases, but it is not clear what the effect on descalability will be. Void formation and location depend, among other things, on oxidation temperature, which means that it is dependent on scaling rate (Taniguchi, 1985).

2.1.2.3 Effects of Alloying Elements

Generally, the oxidation rate of steels is much lower than that of pure iron. The presence of even small additions of alloying elements (impurities) to iron modifies its oxidation behaviour considerably i.e. making it complex (Lee *et al.*, 2005). This complexity may result from the different affinities of alloying elements for oxygen, the different mobility of metal ions in the oxide phase, internal oxidation of one or more elements in the alloy, or solid solubility between oxides, or ternary and higher oxides which can be formed (Abuluwefa *et al.*, 1992).

Interfacial roughening may occur when the alloying element (or impurity) is less likely to be oxidized (is noble) than the iron matrix, or equally when it is more likely to be oxidized (is more reactive) (Pistorius *et al.*, 2003).

2.1.2.4 Internal Oxidation

Internal oxidation is the process by which oxygen diffuses into an alloy and causes sub-surface precipitation of oxides of one or more alloying elements (Birks & Meier, 1983). This result in oxide particles distributed within the metal grains, with often higher concentrations at grain boundaries. These oxides may themselves be deleterious to surface quality, and can also lead to further destabilization of the interface (Whitle & Wood, 1967). The internally oxidized zone extends to the depth at which the concentration of dissolved oxygen becomes too small for formation of oxide (Kofstad, 1966). The depth of the internal oxidation increases with increase in oxidation temperature and time and with decreasing oxygen partial pressure (Kizu *et al.*, 2001).

During oxidation of steels, chromium and aluminium have similar behaviour. In stainless steels where they are present in large quantities, they form protective films of Cr_2O_3 or Al_2O_3 at the metal/scale interface. These films are protective and they inhibit outward diffusion of Fe ions. However, the film often breaks down and a spinel ($FeCr_2O_4$) forms at the scale/metal interface, which allows some oxidation to occur, although the rate is much lower than with ordinary steels (Fujii & Meussner, 1964).

For stainless steel Type 304, the ability to form Cr_2O_3 scales depends on the chromium concentration available at the alloy surface. This concentration can be lowered below that of the bulk alloy by internal precipitation of chromium-rich compounds (Hänsel *et al.*, 2003).

2.1.2.5 Nickel Enrichment

Nickel and other metallic alloying elements that are nobler, that is, less oxidized than iron, are rejected at the metal/scale interface. At the metal/scale interface, iron and chromium enter the chromite lattice while the nickel is rejected. It therefore follows that nickel becomes concentrated at that interface and the surface layer of the metallic core becomes enriched in the nickel (Pickens, 1984).

The nickel does not diffuse rapidly back into the core; the Ni-rich filigree (filaments of unoxidised metal) is more resistant to oxidation. The overall increase in scale thickness leads to particles and filaments of Ni-rich metal being entangled in the scale (Sachs & Tuck, 1968).

The presence of this entanglement in the scale increases scale adhesion to the substrate making descaling quite difficult to perform (Morris *et al.*, 1996) - and give sometimes rise to surface defects (Zittermann *et al.*,1982). This problem is observed in steels with Ni concentrations from 0.05 mass % (Asai *et al.*, 1997).

2.1.2.6 Effects of Minor Alloying Elements and Reactive Element Dispersions

a) Reactive Element Impurities at the Metal-Scale Interface

The behaviour and effects of reactive element impurities have been investigated by others researchers. The following is inferred from their studies:

- For Cr_2O_3-forming alloys, both oxygen-active metal and oxide dispersions at even very small additions can increase or decrease the scale adherence depending on the nature of the interaction of these dispersions with the scale (Nagai, 1989).
- It was suggested that sulphur at normal concentration segregates to the alloy-scale interface where it could promote decohesion of the scale from the alloy (Luthra & Briant, 1989).
- Dispersions of SiO_2, CaO and Cr_2O_3 in the inner layer may inhibit oxygen diffusion along grain boundaries. It was suggested that CaO so enhances the opportunity for outward chromium migration to establish the protective scale at the surface of the Fe-18Cr (Nagai, 1989).
- Oxides of reactive elements at the surface of Fe-Cr alloys enhance the formation and the development of a continuous layer of protective Cr_2O_3 scale (Moon & Bennett, 1989).

- Reactive element dispersions can change the ionic structure of the scale; the large ionic radii of these metals can cause mechanical stress and cracking of the scale (Nagai, 1989).

b) Formation of Low Melting Point Components at the Metal-Scale Interface

- At reheating temperatures**,** the presence of alkali oxides (Na_2O, K_2O) at the interface may facilitate the formation of low melting point binary or ternary compounds with some oxides of refractory metals (Cr_2O_3, SiO_2, CaO). The presence of the liquid phase at the interface may enhance the oxidation of the metal substrate by internal oxidation (Levin *et al.*, 1964). When a scale consists of both solid oxide and molten phase, besides the electronic conduction in the solid oxides, ionic conduction may occur through the liquid phase and increase the rate of oxidation (Kubaschewski & Hopkins, 1962).
- The addition of P to Si-alloyed steel improves the hydraulic descalability because the P lowers the eutectic temperature of FeO/Fe_2SiO_4 during slab soaking. The presence of the liquid compound in the scale/steel interface improves hydraulic descaling (Fukagawa *et al.*, 1997).

2.1.2.7 Stress Development and Relief in Oxide Scale

During high temperature oxidation of steel a protective chromium oxide scale is formed mainly by cationic diffusion. Stresses are produced and build up in the oxide or metal phases due to the difference between the coefficients of linear expansion and molar densities of the oxide and metal (Ajersch, 1992). Stresses are enhanced if several oxides are present at the interface and can cause extensive cracking during cooling (Kubaschewski & Hopkins, 1962). Pieraggi and Rapp (1988) ascribed those stresses to vacancy coalescence at the scale-steel interface and at grain boundaries adjacent to the interface.

Two major effects of the oxide growth stresses are: (a) fracture and subsequently, spallation if large tensile stresses are formed in the scale; and (b) if cracks develop these can enhance oxidation as a result of access of the oxidant to the steel surface.

Relief of growth stresses in oxidizing samples can be through various mechanisms. These are; deformation of the substrate metal, plastic deformation of the oxide, separation at the scale metal interface and fracture of the scale (Pieraggi & Rapp, 1988).

2.1.3 Mould Fluxes

2.1.3.1 Introduction

Mould fluxes are synthetic slags used in continuous casting process of steel. Fluxes are generally added to the surface of the molten steel in a copper mould to provide lubrication between the mould wall and the steel shell (Branion, 1986).

Mould flux reduces the loss of heat from the surface of the steel, and influences the rate of horizontal heat transfer (to the mould) during the solidification of liquid metal in the casting mould. The mould flux also protects the liquid steel surface from re-oxidation with atmospheric oxygen and absorb inclusions (impurities such alumina) from the steel (Persson, 2007).

The mould flux forms a film in the channel between the mould and the steel shell, and after solidification forms a thin solid layer on the solidified steel surface. After continuous casting, steel is covered with a solidified thin layer on the top surface and with a tiny solid layer on the sides. These layers constitute residual mould flux contaminant (Budinski, 1999).

2.1.3.2. Residual Mould Flux on the Casting Slab

During continuous casting, steel is tapped from the ladle into a tundish before passing through the submerged entry nozzle (SEN) into the casting mould. Level control maintains a nearly constant steel meniscus in the mould and makes it possible to feed powder flux onto the liquid steel in the mould (Ogibayashi *et al.*, 1987). As the casting process progresses, new powder flux is gradually added to ensure that the steel surface is always completely covered with mould powder. Mould oscillation avoids sticking of the steel shell to the mould. The oscillation also facilitates the penetration of mould flux into the tiny gap between mould and steel shell (Mills *et al.*, 2005).

The configuration of the powder flux inside the mould is shown in Figure 2.2. Powders are continuously fed onto the top of the mould and form layers over the steel surface which gradually moves down the mould. The powder bed above the steel meniscus consists of four layers, raw powder layer, sintered layer, mushy layer (mixture of slag globules and carbon particles) and a pool of liquid slag (Mills *et al.*, 2005).

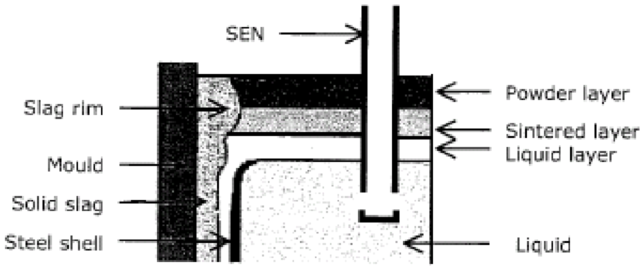

FIGURE 2.2*:* Continuous casting mould flux layers in copper mould (Mills *et al.*, 2005)

A thin layer of mould flux must preferably remain liquid against the hot steel shell throughout the entire length of the mould in order to act as lubricant (Ludlow *et al.*, 2004). The thickness of the solidified flux against the mould is usually much thicker than that of the liquid flux film and is typically of the order of 2 to 3mm (Schwerdtfeger *et al.*, 2003). The thickness of the liquid flux film is about 0.1mm (Rajil *et al.*, 2004).

2.1.3.3 Constitution of Industrial Mould Fluxes

Synthetic flux powders usually contain:

1. raw material with similar melting points (e.g. lithium feldspar, sodium feldspar, wollastonite) to provide more uniform melting in order to avoid accumulation of material at the meniscus
2. a minimum number of raw materials to achieve the required composition so to keep the recipe simple and simplify quality assurance (D'Haeyer, 1987).

The melting temperature of mould flux depends on its composition and is generally less than slab reheating temperature. The composition and melting temperature of three commercial fluxes are given in the table below.

TABLE 2.1: The constituents and melting temperature of commercial fluxes (Jiang *et al*., 2004).

	A	**B**	**C**
Wollastonite	6.5%	-	6.5%
Cement dust	-	4.0%	3.0%
Magnesium carbonate	2.0%	5.5%	6.0%
Quartz	-	3.0%	-
Fluorite	5.0%	8.5%	6.8%
Soda	7.0%	8.0%	12.0%
NaF	4.5%	-	3.5%
Li_2CO_3	-	2.5%	-
Premelted material	75.0%	68.5%	70.0%
Melting temperature	1168°C	1083°C	1055°C

Mould flux contains a mixture of basic oxides and acidic oxides, with varying chemical composition for different applications and steel types (Turkdogan, 1996). The silicate tetrahedron (SiO_4^{-4}) is the major building block in the molten mould flux. It controls physical properties of fluxes such as viscosity, thermal diffusivity, melting range, crystallization temperature, glass transition temperature, tensile strength of slag film, compressibility, surface and interfacial tensions (Persson, 2007). Basic oxides break up the silicate networks in the molten slag structure. Fluoride containing additives (CaF_2, Na_3AlF_6) are used as fluidisers; these also decrease the molten slag viscosity by breaking up the silicate network. During casting, the chemical composition of the mould flux is altered by fluoride volatilization and the absorption of impurities (Persson, 2007). Amphoteric oxides like Al_2O_3 contribute to the silicate structure. Alkali oxides regulate the melting behaviour of slag. Carbon is added in different concentrations to control the rate of fusion (D'Haeyer, 1987).

In steelmaking slag basicity is expressed by the equation below:

$$B_s = \frac{\%CaO + 1.4\%MgO}{\%SiO_2 + 1.5\%P_2O_5} \qquad (12)$$

Due to the fact that in powders flux CaO and SiO_2 are the main components and because P_2O_5 is absent, the simplified basicity of mould powders can be express as follows:

$$B_F = \frac{\%CaO}{\%SiO_2} \tag{13}$$

Powder flux basicity depends on the application and the plant conditions. It varies between 0.7 and 1.3 (Mills *et al*., 2005).

The average range of metallic oxides (and fluoride) in the industrial casting powders and their impact on the viscosity, the melting temperature and the solidification are given in the table below:

TABLE 2.2*:* Chemical composition of mould flux powder and typical effect of increasing flux component on the viscosity and the melting temperature *[www.kempro.com/mould.htm]*

	Component	**%**	**Viscosity**	**Melting point**
Glass formers	SiO_2	17- 56%	Increase	Decrease
	Al_2O_3	0 -13%	Increase	Increase
	B_2O_3	0 -19%	Decrease	Decrease
	Fe_2O_3	0 – 6%	Decrease	Decrease
Alkali	Na_2O	0 – 25%	Decrease	Decrease
	Li_2O	0 – 5%	Decrease	Decrease
	K_2O	0 – 2%	Decrease	Decrease
Basic oxides	CaO	22 – 45%	Decrease	Increase
	MgO	0 -10%	Decrease	Decrease
	BaO	0 -10%	Decrease	Decrease
	SrO	0 – 5%	Increase	Decrease
Fluidiser	F	2 -15%	Decrease	Decrease
	MnO	0 – 5%	Decrease	Decrease
Melting rate control	C	2 – 20%	Increase	Decrease
CaO/SiO_2			Decrease	Increase

2.1.3.4 Estimates of the Expected Mould Flux Concentration on Slabs

Mould flux consumption during casting is an indication of the quality of lubrication. Estimates show that about 90% of the flux consumed is used for the formation of the liquid flux film and the rest is mainly lost to the slag rim and trapped flux in the oscillation marks (Mills *et al*., 2003).

Mould flux consumption can be calculated using the expression below (Mills, 1998)

$$P_s = \frac{7.6\,f\,P_t}{R_m} \tag{14}$$

where P_s is the powder consumption per unit area of mould [kg/m^2], P_t is the powder consumption per steel mass [kg/tonne of steel], f is the fraction of the powder producing slag. R_m is the ratio of surface area to volume of the cast profile and is expressed by the relation (15) below (Mills, 1998).

$$R_m = 2(e_m + l_m)/e_m l_m \tag{15}$$

where e_m is the width of the mould[m], and l_m is the thickness of the mould [m].

Mould flux consumption increases when the casting speed, the mould oscillation and the flux viscosity decrease. It was noticed that mould flux consumption rate per oscillation cycle depends strongly on positive strip time and also correlates with frequency and negative strip time (Shin *et al.*, 2005).

Neumann *et al.* (1996) pointed out that the dependence of mould flux consumption per unit area (P_s) on the mould dimensions can also be expressed by the relation (16) below (Neumann *et al.*, 1996).

$$P_s = 0.44\exp(-0.04R_m) \tag{16}$$

The average thickness (f_l) of the liquid flux film in the mould can be evaluated by means of the equation (17) below (Mills, 1998).

$$f_l(m) = \frac{P_s}{\rho_{flux}} \tag{17}$$

where $\rho_{flux} \approx 2600$ kg/m^3 is the density of the melted liquid flux.

If we assume that, for the case considered in this project, the slab thickness and width are 0.3m and 1.5m respectively, equation (16) and (17) can be used to estimate the amount of mould flux on the slab surfaces. These give the mould flux consumption (P_s) of 0.32kg/m^2 and the average thickness of the liquid film in the mould (f_l) of 123µm.

During this investigation the mould flux surface dosage on the contaminated slabs varied between 0.05 kg/m^2 and 0.35 kg/m^2 (see Table 4.1 and Table 4.9).

2.1.4 Implications for this Work

From the literature survey, it is clear that the removal of scales is mostly linked to the scale-metal adhesion, which depends on the interfacial nature, characteristics of the scale after reheating and the segregation of numerous elements at the interface steel-scale.

Residual mould flux contaminant on steel before reheating may act to decrease or to increase steel-scale adhesion. Residual mould flux and alloying elements may act to decrease scale-metal adhesion as follows:

The presence at the interface of an oxide layer or dispersoids (that contain SiO_2, CaO, Na_2O and Cr_2O_3 in the inner layer) may act as the inhibitor of grain boundary diffusion (Nagai, 1989) and so reduce internal oxidation which acts as a key between scale and the underlying metal substrate when developing sticky scales with nodules deeply incrusted in the underlying alloy (Riquier & Dumortier, 1997).

The presence of MgO and SiO_2 in the scale during descaling can significantly increase the spallation of the scale and improve the descaling effectiveness (Nagai, 1989).

Acid and alkali oxides (Na_2O, K_2O, SiO_2) and fluorides can form some low melting mixtures. The presence of liquid at the scale/steel interface during high temperature descaling is expected to improve hydraulic descaling.

Residual mould flux and alloying elements may also act to increase scale-metal adhesion as follows:

a. Molten phases formed at the interface due to the presence of mould flux may break down the interface and accelerate internal oxidation.

b. Beside the electronic conduction in the solid-oxides, ionic conduction may occur through the liquid phase and increase the internal oxidation (Kubaschewski, & Hopkins, 1962).
c. The presence of Al_2O_3 and some molten oxide dispersions at the interface may improve scale adherence and minimize the porosity of the scale (Moon & Bennett, 1989).

2.2 REHEATING OF STAINLESS STEELS

2.2.1 Introduction

Reheating of steel before hot rolling is an essential step, which is not totally controlled and optimised despite the various improvements made in the last two decades (Bockel-Mac & Zamuner, 2002). Reheating aims to facilitate subsequent hot forming and to oxidize away some surface imperfections (Li *et al*., 2005).

2.2.2 Influence of Reheating Parameters on Descalability

The microstructure of the scale close to the interface, which affects the scale-steel adhesion and hence the descalablity, is influenced not only by the steel chemical composition, but also by the heating parameters (reheating temperature, reheating time and composition of the gas in the furnace atmosphere) (Dénes *et al*., 2003).

After reheating following by mechanical descaling of the stainless steels grade 412 and 304, it was found that:

The descalablity of the steel type 412 was very sensitive to the reheating parameters (mainly reheating time and the excess of oxygen in the furnace gas atmosphere). For this steel grade, the extent of the entangled region which arose at the interface scale-steel and made descaling quite difficult was found to increase for longer reheating times and higher excess oxygen contents.

In contrast, for the steel grade 304, the descalability was found to be mostly linked to the microstructure of phases formed close to the interface, the austenite grain structure, and not primarily on the conditions in the reheating furnace. For this steel grade, descaling proceeds along chromite layers (paths in the scale which consisted of oxide only without Ni-metal enriched tendrils) formed on the austenite grain boundaries. The formation of this chromite was enhanced for reheating with higher excess oxygen, longer reheating times and at high temperature (Pistorius *et al*., 2003).

2.2.2 Effect of Water Vapour

Tuck *et al.* (1969) found that the oxidation rate of most steels at a given temperature is greater in steam than in air or oxygen after long exposure times; and this effect can be increased if water vapour is present with O_2. It follows therefore that the scaling rate would be greater in oxygen/water vapour mixture than it would be in either of the gases separately (Tuck & Barlow, 1972). However, at temperatures lower than 950ºC and higher O_2 concentrations, increasing the water vapour content of the gas mixture had no effect on scaling rate (Sachs and Tuck, 1970). In oxidizing gas mixtures (oxygen containing more than 10 vol % H_2O) at 950ºC, the scale remained attached to the metal surface for considerably longer reaction times than in the absence of water vapour, and the scale growth progressed in accordance with the parabolic rate for pure Fe (Sheasby *et al*., 1984). The presence of water vapour leads to greater plasticity in the scale and consequently greater scale adherence to the substrate (Kofstad, 1988) whereas adherence was lost in samples scaled in oxygen alone. At 950ºC, thicker and more compact scale was formed on mild steel. These observations have been attributed to the penetration of pores in the scale by H_2/H_2O mixture, which enhances inward migration of oxygen (Tuck *et al*., 1969). Therefore in order to achieve scale growth that is comparable to that in reheating furnaces, the presence of water vapour in the laboratory furnace atmosphere is vital [(Sheasby *et al*., 1984), (Kizu *et al*., 2002)]. The concentration of water vapour required in the gas mixture to obtain product gas containing 3% excess oxygen, for example was calculated to be about 16.3 % (Appendix 1).

2.2.5 Surface Finish and Surface Structure

The structure and composition of the surface of the slab depend on the solidification mode and reheating conditions, and can change from one slab to another. This makes it difficult to simulate exactly industrial operating conditions (Riquier & Dumortier 1997).

Polished or ground surfaces are often used during oxidation studies, to provide a reproducible starting condition. However, it has been found that the nature of the surface finish does always affect the scaling process. Studies were carried out to find the influence of surface roughness on the adherence of oxides formed on type 1018, 304, and 430 steels, and it was found that oxide adherence could be enhanced by smooth surface or hindered by a rough finish (Sherwood *et al*., 1984).

Sherwood *et al*. (1984) found that deep scratches on a coarsely finished metal may act as stress raisers and set up high compressive stresses at the steel/scale interface, giving rise to scale fracture and subsequent spallation. When a scale grows by cationic diffusion, the new scale grows on the top of the old, which implies that the original surface is trapped at the scale/metal interface. Only in the case of extensive internal oxidation, is the surface finish expected to be less important.

2.3 DESCALING

2.3.1 Introduction

The primary scale formed on the slab during reheating (prior to roughing rolling) and secondary scale formed on steel during roughing rolling are often removed with high-pressure water sprays (hydraulic descaling), while the tertiary scale which forms during finishing rolling is removed by acid pickling prior to other processing steps (Chen *et al.*, 2001).

2.3.2 Hydraulic Descaling

2.3.2.1 Principle

Hydraulic descaling systems consist of a pump, which delivers high pressure water to a header bar over the steel, from which water is sprayed through a series of nozzles. In flat products each nozzle is designed to spray water in a flat sheet, allowing the jet from a nozzle to strike the steel in a straight line; the nozzles are angled, so that the impingement patterns from adjacent nozzles do not overlap, and the force of impact is not reduced. The jets are also generally directed towards the approaching steel (Morris *et al.*, 1996).

In Figure 2.3, the scale is removed from the front to the back while the slab is moved from the back to the front. The scale is removed on both sides of the slab, and the rear part of the slab is not yet descaled.

Hydraulic descaling is affected by the scale thickness, jet angle, jet velocity, steel temperature and time of exposure to water jet (Sheppard & Steen, 1970).

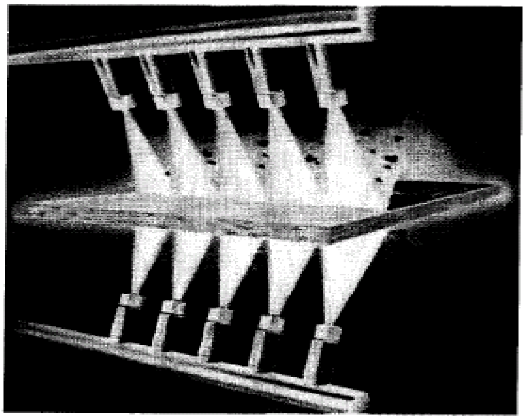

FIGURE 2.3: Double- sided industrial descaling process using several nozzles (Schürmann, 2000).

2.3.2.2. Descaling Header Designs

Figure 2.4 shows the typical nozzle arrangement with the list of terms and symbols.

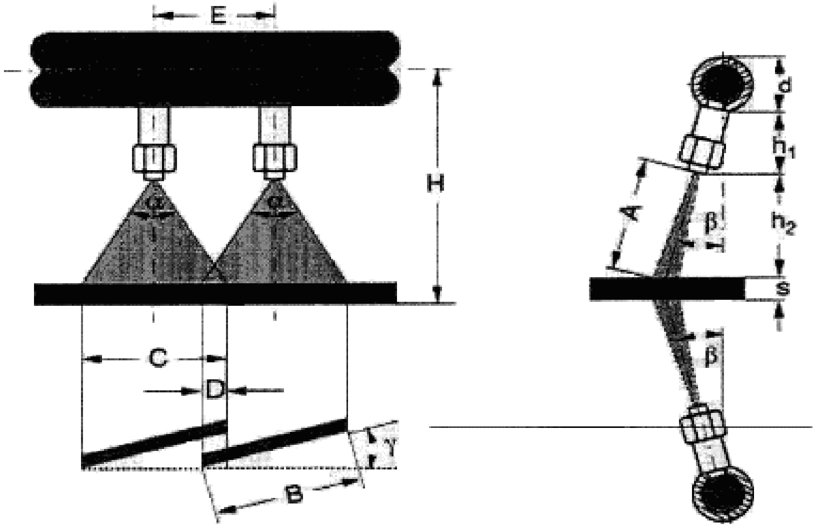

A = jet length
B = jet width
C = jet width in jet direction
D = overlapping
E = nozzle distance
H = distance from mid-spray beam
to lower edge of strip

S = strip thickness
d = outer diameter of pipe
h_1 = vertical height of nozzle
h_2 = vertical spray height
α = nozzle spray angle
β = angle of inclination
γ = offset angle of nozzle
against pipe rotation axis

FIGURE 2.4: Typical nozzle arrangement with list of terms and symbols (Frick, 2003).

Computer simulation software enables the prediction of the optimum nozzle arrangement as a function of variables which influence the design of a descaling nozzle arrangement. These variables are water pressure; total water flow; spray height; the slab width and thickness (Boulton *et al.*, 2004). The Figure 2.5 below shows an example of the output of a computer simulation program for a proposed nozzle arrangement.

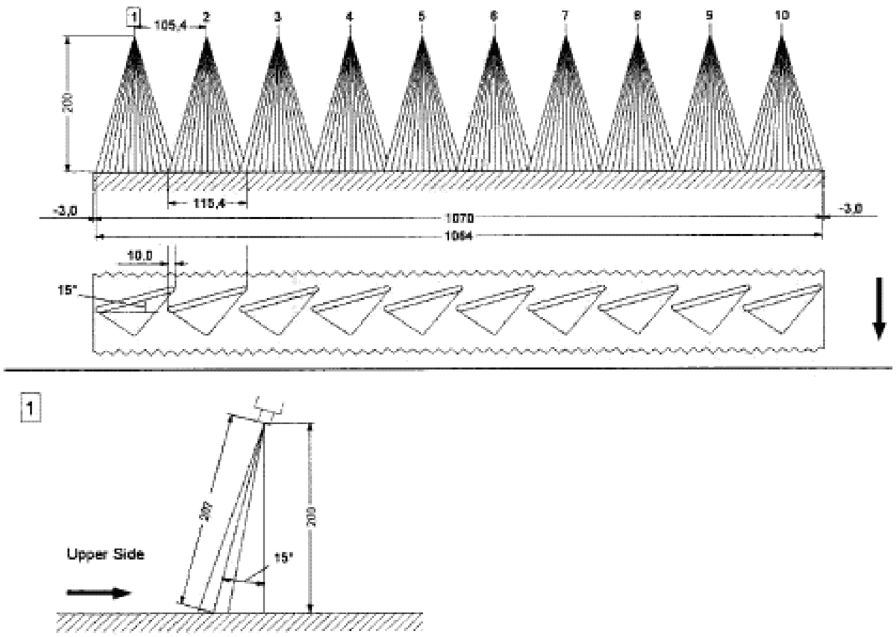

Nozzle part number:	642.887	Spray width (B):	120mm
Nozzle spray angle (α):	30º	Spray depth:	8.61mm
Pressure:	200 bar	Total force:	521 N
Flow rate:	158.39 l/min	Impact, av 85%:	0.74N/mm^2
Inclination angle (β):	15º	Max. impact:	0.97N/mm^2
Offset angle (γ):	15º	Total flow rate:	1583.9 l/min
Vertical spray height (h_2):	200mm	Overlap (D):	10.0 mm

FIGURE 2.5: Proposal of a typical descaling installation carried out by means of Lechler Descale program (Boulton *et al*., 2004).

a) <u>Nozzle spray characteristics</u>

Descaling nozzles can have orifices of different shapes but the best results are obtained with elliptically shaped ones, because a relatively constant impact pressure can be maintained across the jet (Sheridan & Simon, 1995). Impact pressure, which is a measure of the force with which the water impacts the steel stock, is a maximum when the nozzle geometry is vertical due to its scouring action on the chipped scale, so removing the scale (Sheppard & Steen, 1970).

As mentioned, the rolling mill descaling stations are usually designed with the nozzles inclined towards the approaching steel. The main reason is that detached scale is directed away from the rolling stand. If the stand is a sufficient distance from the descaler so it will not be affected by the detached scale, most efficient descaling is achieved with vertical nozzle geometry. The jet width and thickness increase linearly with nozzle stand-off distance (height) (Morris *et al.*, 1996). At a constant water flow rate and for given impact width, maximum impact pressure decreases linearly with nozzle height (Sheridan & Simon, 1995).

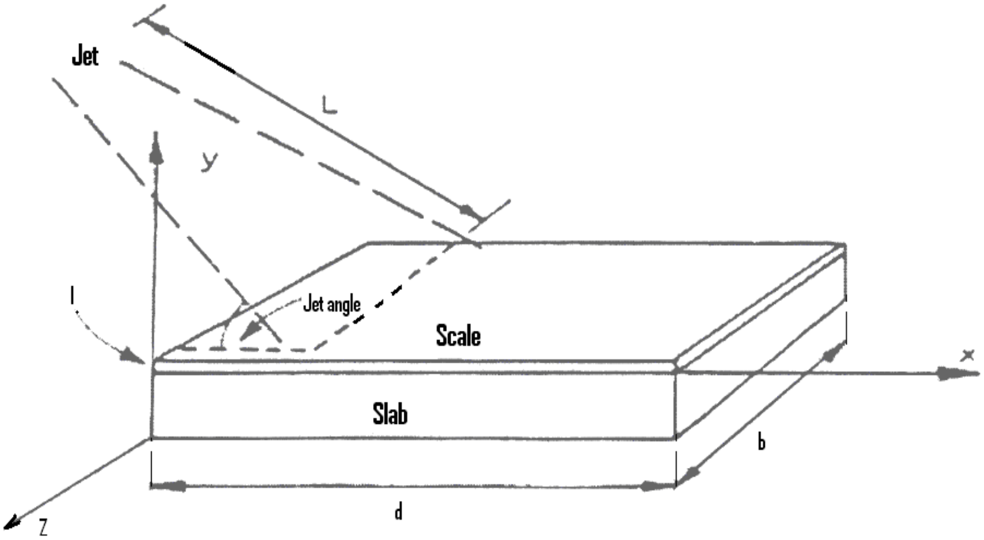

FIGURE 2.6: Geometry of the offset angle of the cooling jet (Sheppard and Steen, 1970).

It was found that the descaling capacity increases with the nozzle diameter but the efficiency is better with smaller nozzles. Hence, it is best to use a larger number of nozzles of smaller diameter with a reduced pitch between nozzles (Sheridan & Simon, 1995). Four nominal spray angles describing the width of spray are now very common. These are 22°, 26°, 30° and 40° nozzle tips, each are available in 13 standard flow sizes in order to achieve design flexibility; the spray width is identical for all nozzle tip sizes at identical pressures and spray heights (Frick, 2004).

In modern installations with spray heights around 80mm spray depths range between 3 and 4mm only (Sheridan & Simon, 1995). The water pressure and the water flow are approximately proportional to the impact. Table 2.3 shows the influence of water pressure on the impact for a spray height of 128mm.

TABLE 2.3: Influence of the system water pressure and the flow rate on the impact pressure (Frick, 2004).

Scale-master type	**Spray angle [°]**	**Water pressure [bars]**	**Water Flow [l/min]**	**Spray jet width [mm]**	**Spray Jet Thickness [mm]**	**Total force [N]**	**Max Impact [N/mm^2]**
694.566.27	26	100	18.00	57	3.80	42	0.26
694.566.27	26	200	25.50	58	3.60	84	0.54
694.566.27	26	300	31.20	58	3.40	126	0.84
694.566.27	26	400	36.00	59	3.20	167	1.17

Descaling jet impact pressure decreases when the jet thickness increases as shown in the graph bellow.

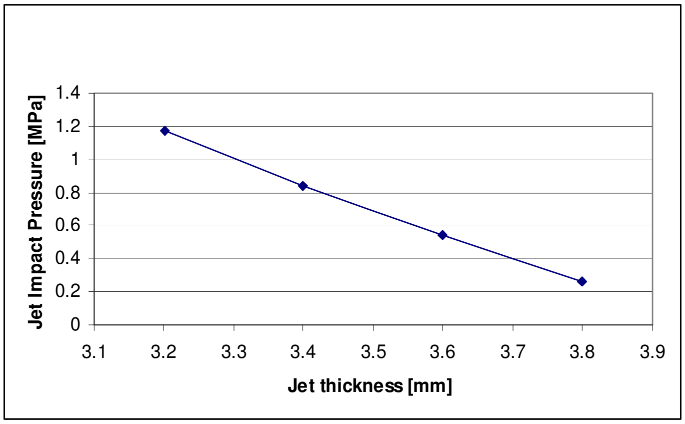

FIGURE 2.7: Variation of impact pressure trough the jet thickness at a system pressure (Scale-master type 694.566.27 nozzle 26° spray angle at 128 mm distance) (Frick, 2004).

The speed of the stock under the descaling spray and the water flow from the spray determine the volume of water applied to the steel surface. These two parameters and the width of the descaling spray are used to calculate the specific water impingement (U).

$$U(litre/m^2) = \frac{Q(litre/s)}{B(m).v(m/s)} \qquad (18)$$

The specific water impingement influences the rate of cooling of the steel surface and the effectiveness of the descaling process (Morris *et al.*, 1996).

b) Header diameter

For pipes with fixed flow rate and water pressure larger header diameters (150mm) yield lower velocities, and bring less turbulent flow than those with smaller diameter heads. Less turbulence gives better descaling action since more kinetic energy remains in the spray. Modern descaling systems endeavour to achieve an optimum velocity of 1.2 m/s in the header (Grigg *et al.*, 1987).

2.3.3 Mechanisms of High Pressure Water Descaling

2.3.3.1 Introduction

Hydraulic removal of the scale is dependent on both the impact pressure and quantity of applied water per unit area, the total stress produced by cooling action of water jets, the stress due to the impact force of the jet and the depositional compression stress (the oxidation stress) (Matsuno, 1980).

The theoretical possible mechanisms of high pressure water spray descaling are:

- Thermal gradient within scale (scale bending away),
- Differential contraction effect (scale breaking away),
- Disruption of scale by steam (scale rupture),
- Mechanical pressure effect (force of water crushes & fragments scale) (Morris *et al.*, 1996).

2.3.3.2 Thermal Effects

Thermal effects arise from water cooling and mechanical pressure effects. The scale on steel slabs, to greater or lesser extent, has the tendency to crack due to water-cooling. Scales on Si-killed steels are more susceptible to cracking into small pieces in air whereas scale on semi-killed steels do not crack easily on air-cooling (Fukutsuka *et al.*, 1981). The scale is subsequently washed away along the cracks due to the effect of the water.

During descaling, there exists a thermal gradient within the scale that leads to thermal contraction stresses and bending of the scale away from the steel. This thermal gradient arises as a result of the difference in temperature between the descaling water and the scaled steel or the scale when the steel is removed from the furnace (Morris *et al.*, 1996). The cooling and contraction of the scale cause it to curl and break away (Sheridan & Simon, 1995). Reducing the sample speed under the descaling water spray increases the effective volume of water directed to a given area of steel, which leads to a further reduction of the temperature and consequently increasing the descaling action. Formation of steam leading to disruption of the scale has the ability to supply sufficient energy to the scale for fracturing of the metal/scale interface. However, this mechanism is dependent on the ability of the water to penetrate pores and fissures within the scale and produce an undercutting effect (Morris *et al.*, 1996).

2.3.3.3 Mechanical Pressure Effects

On the other hand, when considering the effects of the mechanical pressure, it should be noted that the force exerted by the water jets on the surface of the scale could produce displacement of the scale if porosity or detachment exist. This mechanism would be expected in friable scale and its effectiveness would increase at higher water pressures. Furthermore, the scale may be crushed and shattered due to the pressure of the water jet on it and subsequently washed away (Morris *et al.*, 1996).

Increasing the water pressure means an increase of the kinetic energy and the impact pressure. Hence, more scale will be removed from the steel at shorter dwell time under the jets. This is illustrated further with the aid of the figure below:

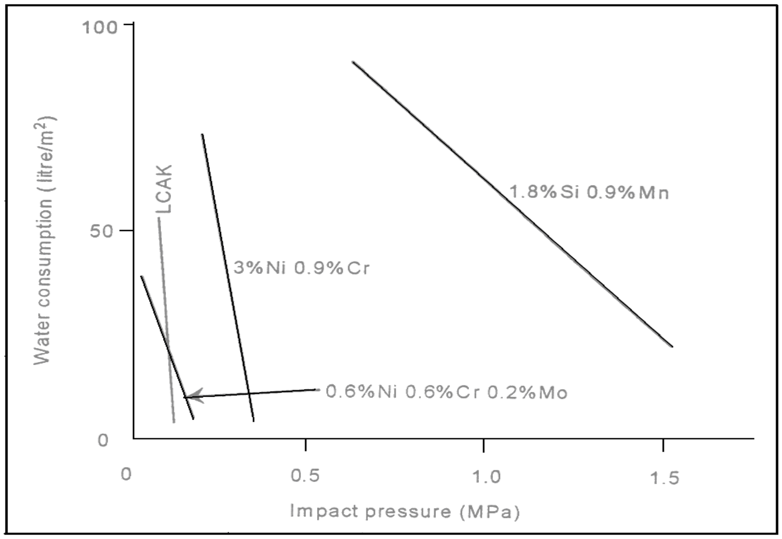

FIGURE 2.8: Conditions required for the effective descaling of different steel grades (Sheridan & Simon, 1995).

Figure 2.8 shows that plain carbon steels (labelled "LCAK" in the figure) are the most easily descaled whereas those containing considerable amounts of silicon or nickel are much more difficult to descale, that is they form more adherent scale. The effectiveness of the descaling of the low carbon steel depends on the impact pressure being high enough. This goes to confirm the mechanism of descaling by mechanical effects, whereas in the case of the steels that are more difficult to descale, especially the high silicon one, there is a compromise between the specific water consumption and the impact pressure. At low impact pressure (~ 0.8MPa), descaling this steel effectively required a large amount of water. This translates to longer dwell time of this steel under the water jets. At an impact of about 1.5MPa, a low amount of water (~25l/m ^{2}) was consumed, hence with a shorter dwell time. This effect of dwell time indicates that a comparatively slow process such as heat transfer through the scale may influence the descaling of steels (Sheridan & Simon, 1995).

Heat is transferred from the steel slab by conduction to the scale surface and by convection and radiation to the water spray. By assuming that heat conduction through the scale contributes to the scale removal on the steel surface, the descaling header pressure (Δp) and the time (t) required to obtain successful descaling for given reheating conditions would be linked to the square of the scale thickness (l^2) by the parameter $\Delta pt/l^2$. The predicted effect of the heat transfer is to quench the scale thereby leading to contraction, scale failure being as a result of thermal shock (Sheppard & Steen, 1970).

The thermal shock effect can be evaluated by estimating the time required to cool the scale to a given depth. If conduction through the scale is assumed to be the determining step, the time to cool the scale can be expressed by l^2/δ (where l and δ are the scale thickness and thermal diffusivity respectively). The heat capacity value of wustite from FactSage and thermal conductivity and density from Akiyama *et al.* (1992) were used to estimate the scale thermal diffusivity at 1100° C; the estimated value is $8.5x10^{-7}$ m^2/s

For a typical water jet thickness of 5mm and slab speeds of 0.1 to 1 m/s (Morris *et al.*, 1996), the time that the scale is exposed to water jet is between 5 and 50 ms. Based on the thermal diffusivity value, this time is only sufficient to quench 0.06 – 0.2 mm of the scale (compared to total thickness of the scale which after reheating, may be 5mm or more).

The above results suggest that thermal shock effect will be less effective than mechanical effect under hydraulic descaling conditions, as proposed by Blazevic (1987).

2.4. CONCLUSIONS ON EXPERIMENTAL APPROACH

From the above literature and based on the two legs of this project (i.e. the descaling efficiency and the effect of mould flux on scale-steel adhesion after reheating), the experimental approach therefore involved scale growth on contaminated slabs under gas mass transfer conditions similar to those in reheating furnaces, followed by the laboratory high pressure hydraulic descaling of the sample while hot. The evaluation of the residual scale amount and the characterisation of the structure and composition of the scale oxide layers were performed by means of scanning electron microscopy and X-ray microanalyses.

The reheating variables considered were temperature, time, excess oxygen and mould flux surface concentration.

The descaling variables considered were the water flow rate and the system pressure. The descaling spray height and the descaling speed were maintained constant.

The experimental techniques and procedures that were used are detailed in the next chapter.

Chapter 3: MATERIALS AND EXPERIMENTAL TECHNIQUES

3.1 INTRODUCTION

The experimental investigations included the following:

- Scanning Electron Microscopy (SEM-EDX) analysis and X-ray analyses (XRF and XRD) for surface characterisation of slabs (stainless-steel type 304),
- Decarburisation of powder mould flux at 600ºC in air in a muffle furnace followed by chemical analyses (XRF, ICP-AES and LECO elemental analysis for carbon and sulphur),
- Contamination of the upper steel surface with a paste prepared by mixing alcohol with decarburized powder flux, before reheating,
- Scale growth under reheating conditions, using large samples to avoid edge effects,
- Scanning Electron Microscopy (SEM-EDX) and X-ray diffraction for characterisation of the oxide layers,
- X-Ray photoelectron spectroscopy (XPS) analyses were used to determine the oxidation state of chromium in the removed scales,
- High-pressure water descaling of hot samples,
- Scanning Electron Microscopy (SEM-EDX) and X-ray diffraction for characterisation of the oxide layers and morphology at the interface after descaling,

Preliminary high temperature reheating trials were done on the contaminated and non-contaminate slabs under reheating conditions in order to test the water level in the gas atmosphere and to assess the melting of powder flux on the slab top surface under reheating conditions.

3.2 SAMPLE SIZE AND SAMPLE COMPOSITION

SEM-EDS analysis was used for chemical elemental analysis of slab and hot rolled samples used for reheating following by descaling, and XRF, ICP-AES and LECO analyses were used for quantitative analysis of decarburized powder fluxes used to contaminate the samples. XRF analysis was used to determine powder flux metallic oxide components, ICP-AES to determine fluorine and phosphorus, and carbon and sulphur were determined by combustion methods (LECO). The average chemical compositions of stainless steel and decarburised industrial mould fluxes used during this investigation are given in table 3.1 below.

In order to determine the effects of mould flux type on descaling and how the differences in mould flux composition affect the scale structure, synthetic mould fluxes were also prepared. Table 3.2 gives the composition of these synthetic mould fluxes.

TABLE 3.1: Stainless steel composition (mass percentages, balance iron) and decarburized mould flux compositions (mass percentages).

Steel		**Mould fluxes**			
Elements	[%]	Species[%]	Type 832	Type RF1	Type 810
Cr	18.16	SiO_2	35.92	33.97	34.10
Ni	8.09	CaO	32.53	38.98	35.34
Mn	1.305	Al_2O_3	5.92	7.32	6.98
Si	0.40	F	3.16	3.32	5.35
Mo	0.14	Na_2O	18.43	13.11	13.34
V	0.12	Fe_2O_3	0.55	1.46	1.52
Cu	0.09	MgO	2.6	0.96	1.43
C	0.044	TiO_2	0.19	0.14	0.30
N	0.050	MnO	0.057	0.035	2.81
Co	0.03	K_2O	0.13	0.55	0.17
P	0.022	P	0.053	0.038	0.06
Ti	0.01	Cr	0.073	0.005	0.015
O	0.0080	Ni	0.002	0.001	0.011
Al	0.004	V	0.007	0.002	0.017
S	0.0033	Zn	0.07	0.019	0.019
Nb	0.003	Sr	0.014	0.097	0.023
B	0.001	CaO/SiO_2	0.905	1.147	1.036

TABLE 3.2: Synthetic mould flux compositions (mass percentages)

Mould Flux	**CaO**	**SiO_2**	**CaF_2**	**Na_2O**
SMF1	40%	40%	20%	-
SMF2	40%	40%	-	20%
SMF3	50%	50%	-	-

The steel samples were cut to size from hot rolled plate using a band saw as well as a fixed abrasive disc cutter. Since stresses are developed at the edges and corners during scale growth, samples had large lengths and widths in comparison to the scale thickness (which could be as high as 0.5cm for longer reheating times). The steel samples were typically around 45mm x 45mm x 15mm large. The sample corners were bevelled away, to allow the samples to hang with their larger dimensions horizontal inside a tube furnace (to avoid mould flux dripping from the upper sample surface, where the flux was placed). Grooves, 1.5mm deep, on each side of the sample, served to secure the sample with Kanthal wire to a mullite rod. Figure 3.1 below shows a sketch of the sample, Kanthal wire and the mullite rod used to hang the sample in the furnace. Figure 3.15 on page 48, shows a photograph of a sample in the descaling device.

The stainless steel samples used in this investigation were slabs of continuous casting and plant-pickled plate samples (15mm thick), and were hence only degreased (with alcohol) before scaling. After reheating in gas atmosphere, the surface of the slabs and scale were characterised by SEM and X-ray analysis.

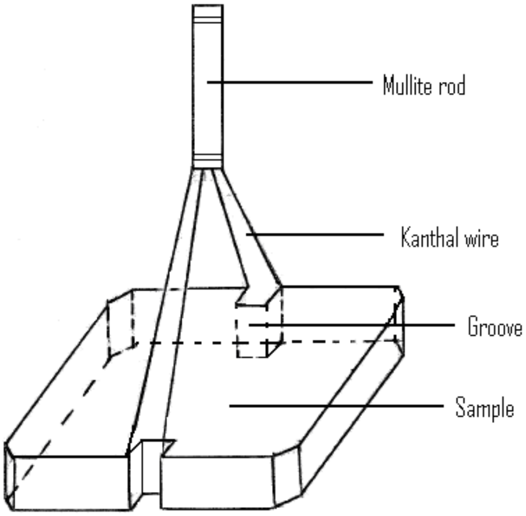

FIGURE 3.1: Sketch of the samples used during the experimental runs (not drawn to scale).

Casting powder (flux) was decarburised at 600ºC for 15 hours in air in a muffle furnace before the flux was applied to the steel surface.

Three types of industrial mould fluxes were used in this investigation to growth scale on 304 slab; type 832, STSP 810 (Stollberg) and RF1 (Syntherm). Synthetic mould fluxes SMF1, SMF2 and SMF3 were also used.

X-ray diffraction (XRD) of decarburized type RF1 flux (generally used for stainless steel type 321) revealed the following phases: $Ca_4Si_2O_7F_2$ (Cuspidine), $Na_2Al_2Si_2O_8$ (Nepheline) and CaF_2 (Fluorite). LECO analysis gave 0.1% carbon and 0.62% sulphur in this flux.

3.3 EXPERIMENTAL SET- UP FOR SLAB REHEATING AND DESCALING

3.3.1 Reheating Experimental Set-up used to Growth the Scale

The experimental set-up used to simulate industrial reheating conditions is shown in figure 3.2 below.

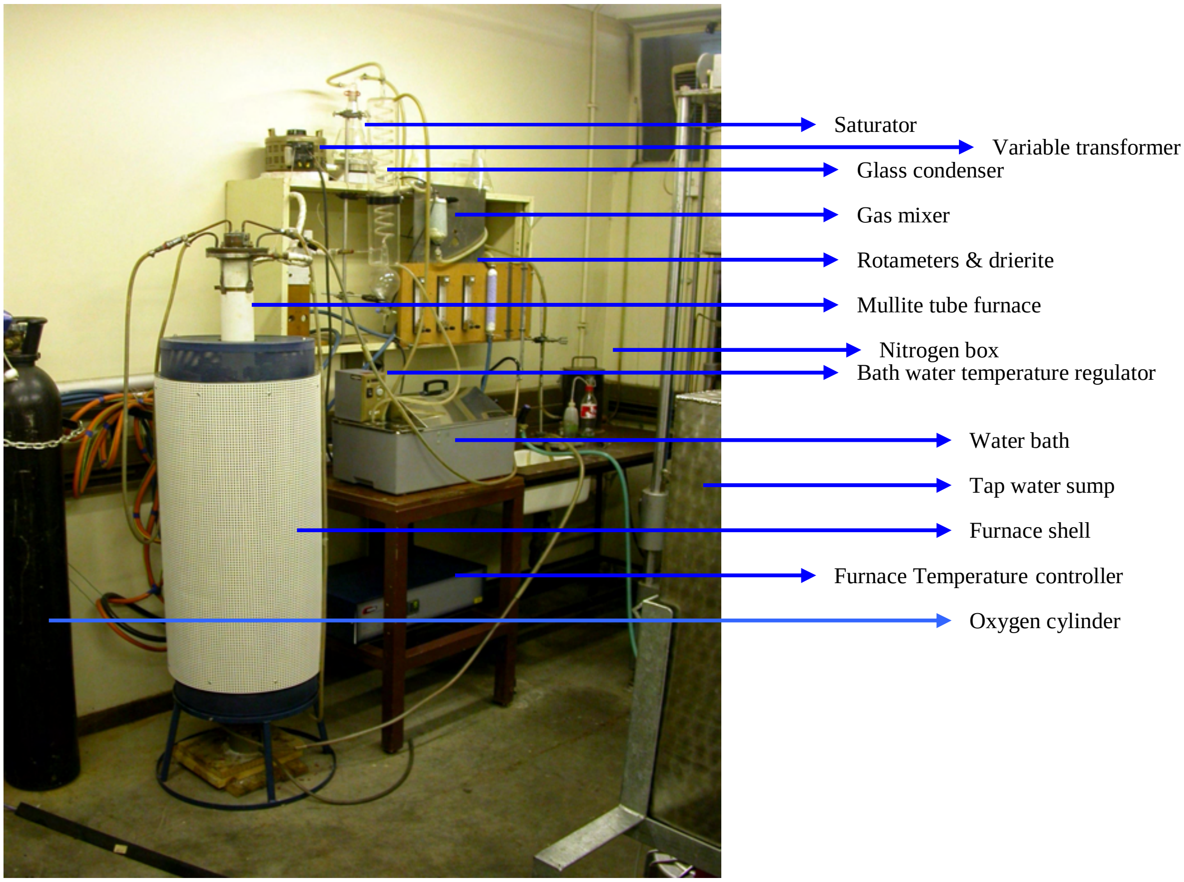

FIGURE 3.2: Photograph of the reheating experimental set-up

3.3.2. Gas Mixing System

The gas system was chosen to simulate the combustion product of methane (CH_4) in air with 3% or 4% excess free oxygen, that is, the gas contained CO_2, O_2, N_2 and water vapour. The gas flow rate was chosen to produce similar mass transfer conditions (which depend on the Reynolds number) to industrial furnaces. The total gas flow rate was equal to 5Ndm^3/min. The gases, CO_2, O_2, N_2, were chemical pure with the minimum purity of both oxygen and nitrogen equal to 99.5% and that of carbon dioxide 99.0%.

The three gas lines were then joined before the gas mixer. The flow rate of each gas was measured and controlled by the rotameters which were calibrated by means of a bubble-meter. Calibration was done in order to ensure that accurate amounts of gas are flowing through the reactor. To check gas flow rates, the gases were allowed to flow from the regulator on the gas cylinder through the rotameter to a graduated cylinder filled with liquid soap up to the gas inlet level. By passing the gas through the graduated cylinder, the soap produced bubbles which moved upward and exited through the outlet gas. This allows the gas bubble to travel through a specific length of the cylinder. From the inside diameter of the cylinder, the volume travelled by the gas during a specific interval was determined and so the flow rate was calculated as the ratio volume-time take by the gas to travel a certain distance in the graduated cylinder at the ambient temperature (25ºC) and atmospheric pressure of Pretoria (0.865 atm). The ratio was evaluated at a certain setting on the rotameter. The sketch of the system used to calibrate the gas flow rate is shown in figure 3.3 below.

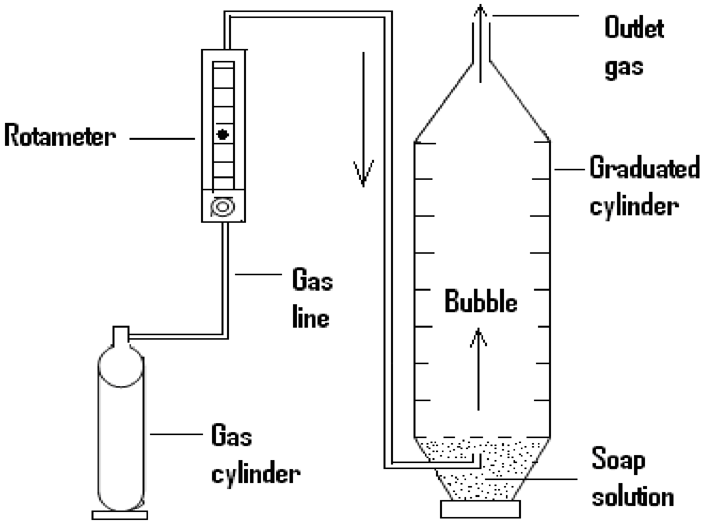

FIGURE 3.3: Schematic representation of the apparatus used to calibrate the gas flow rate (not drawn to scale).

Rotameter setting was determined by plotting gas flow rate versus rotameter reading. Correlations fitted to these results were used to calculate the position of the float in the rotameter for a specific flow rate.

The inline calibration of the rotameters was essential to ensure that the exact flow of the gas mixture was maintained, because a back pressure in the gas line would definitely affect the flow rate. The gas mixing set-up is shown schematically in figure 3.4. The appendix 1 details the process of rotameter calibration and settings

The gas mixer is a glass cylinder filled with glass beads to give turbulent flow of gases and proper mixing of the gases. After the gas mixture left the mixer, it then entered the saturator, which was filled with water kept near its boiling point.

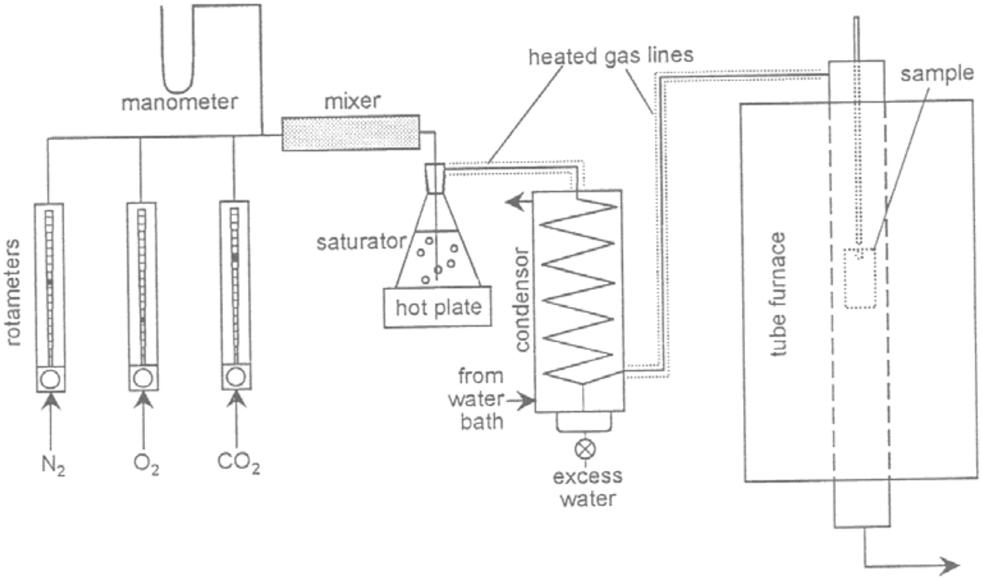

FIGURE 3.4: Experimental configuration used to grow scale in reheating furnace (Pistorius *et al.*, 2003).

Passing the gas through the saturator loads the gas with water vapour. By passing the mixture trough a temperature-controlled glass condenser, the excess water was removed and periodically drained off through the outlet at the bottom of the condenser.

A schematic representation of the temperature-controlled condenser is shown in the figure below:

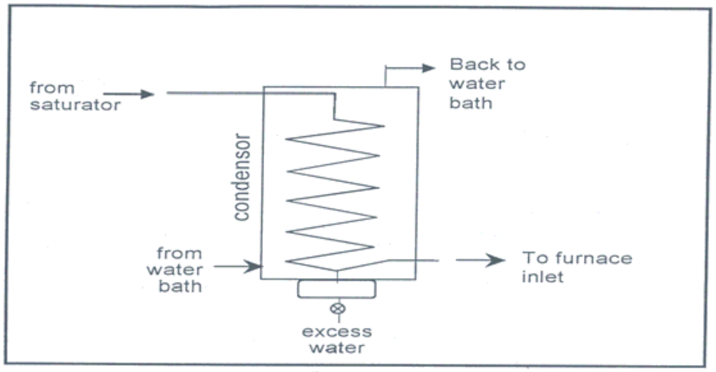

FIGURE 3.5**:** Schematic representation of temperature-controlled glass condenser (Pistorius *et al.*, 2003).

The temperature of the water circulating in the outer section of the condenser was maintained at 60ºC. This temperature control was accomplished by using a water bath. Between the exit of the condenser and the furnace inlet, a three-way brass valve was fitted. All the connections between the water saturator and the furnace were heated by using heavy insulated heating tape with a knitted Fibrox covering (Barnstead Thermolyne). The variable transformer controlling the heating tape temperature was set at 130 V so as to ensure that the temperature of the heating tape was approximately 80ºC. All connections between the regulators and the condenser were carried out using silicone rubber tubing, whereas those between the three-way valve and the furnace were done by using PFA-tubing. The PFA-tubing was used because its hardness made wrapping the heating tape around it easier. The gas mixture was checked to make certain it contained the correct amount of water vapour. To do this, the gas outlet at the bottom of the furnace was connected to a pre-weighed drierite (anhydrous $CaSO_4$) column, which was weighed again after the experiments. The amount of water that was absorbed by the drierite was established by the difference in weight. The theoretical and measured values of the water vapour in the gas mixture were 18.54g and 19.88 g (See Appendix 2).

3.3.3 Furnace Set-up

Reheating experiments was carried out in a vertical tubular furnace with a mullite working tube. The dimensions of the tube were 150 cm length × 9.0 cm O.D. × 7.6cm I.D. The inside diameter of 7.6 cm allowed for oxidation of samples with the following typical dimension: width = 45 mm, length = 45 mm and thickness = 15mm.

The furnace temperature was controlled by a Eurotherm 902P controller / programmer using a thermocouple that was positioned next to the furnace tube, close to the hot zone.

A schematic representation the furnace assembly is shown in figure 3.6.

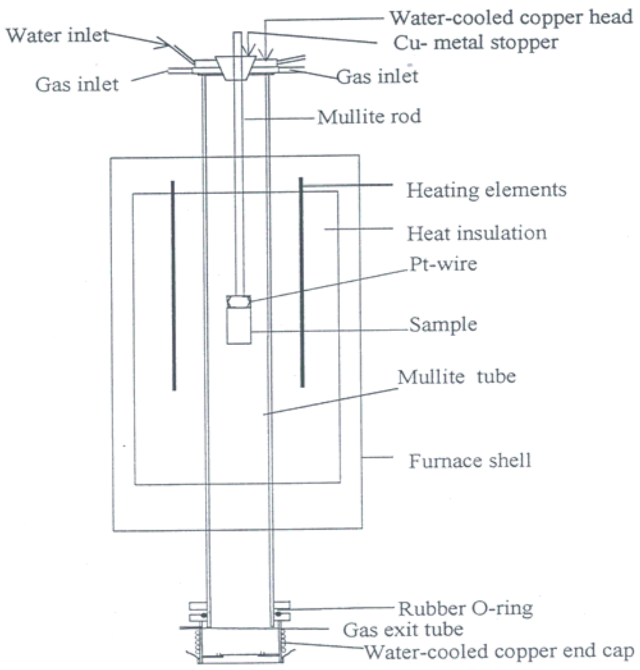

FIGURE 3.6: Schematic representation of furnace assembly (Pistorius *et al.*, 2003).

The exact position of the hot zone was measured by placing a hand-held type R (Pt-13% Rh) thermocouple at various depths in the furnace tube. The temperature profiles for programmed temperatures 1250°C and 1300°C are shown in figure 3.6.

The reference point from which the depth was measured was the top of the working tube.

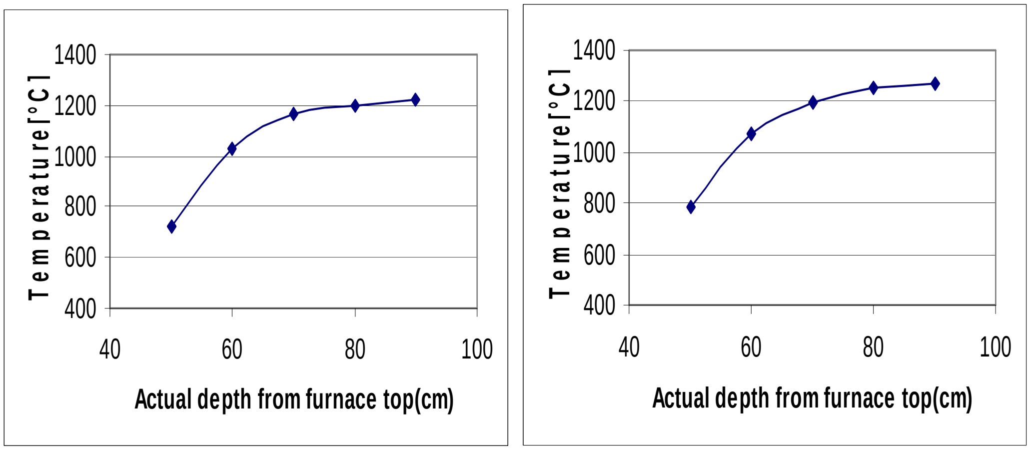

FIGURE 3.7: Temperature profile at programmed furnace temperatures of 1250°C and 1300°C

The measured temperature in hot zone as a function of programmed furnace temperature is shown in the chart below:

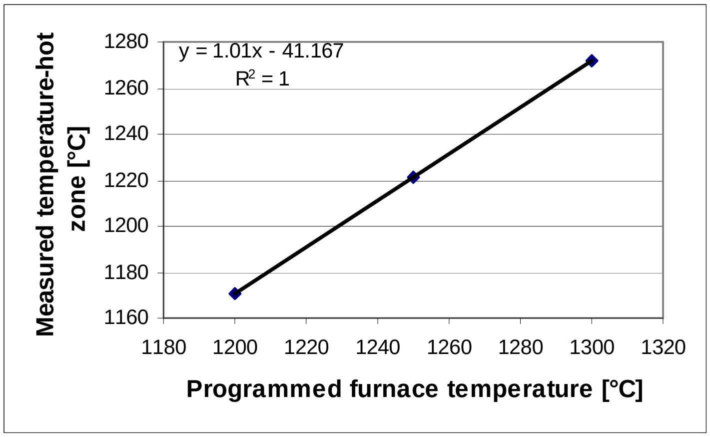

FIGURE 3.8: Measured temperature in hot zone versus programmed furnace temperature at a depth of 90cm below furnace top.

The average temperature of the hot zone measured with the hand–held thermocouple was within 30ºC of that indicated by the furnace controller.

The mullite furnace tube (9 O.D. x 7.6 cm I.D. x 150 cm lengths) was fitted with water-cooled copper heads at both ends. The bottom fitting extended below the mullite tube and was sealed with an O-ring lubricated with high temperature vacuum grease. The upper end cap was sealed to the open flat end of the tube, sealing on a rubber gasket between the tube and the fitting. A steel bracket attached to the furnace tube exerted pressure on the gasket. Braided tubing was used for connecting the cooling water inlet and outlet to the furnace. Quick-connect couplings were used to ensure that the cooling water tubes could easily be removed from the copper-end cap before removal of the sample for descaling.

3.3.4 High Pressure Hydraulic Descaling Set-up

Immediately after the scaling period, the samples were removed from the furnace and subjected to hydraulic descaling; cooling of the sample can lead to ineffectiveness of the descaling (Sheppard & Steen, 1970).

The experimental laboratory descaling unit is shown in figure 3.9.

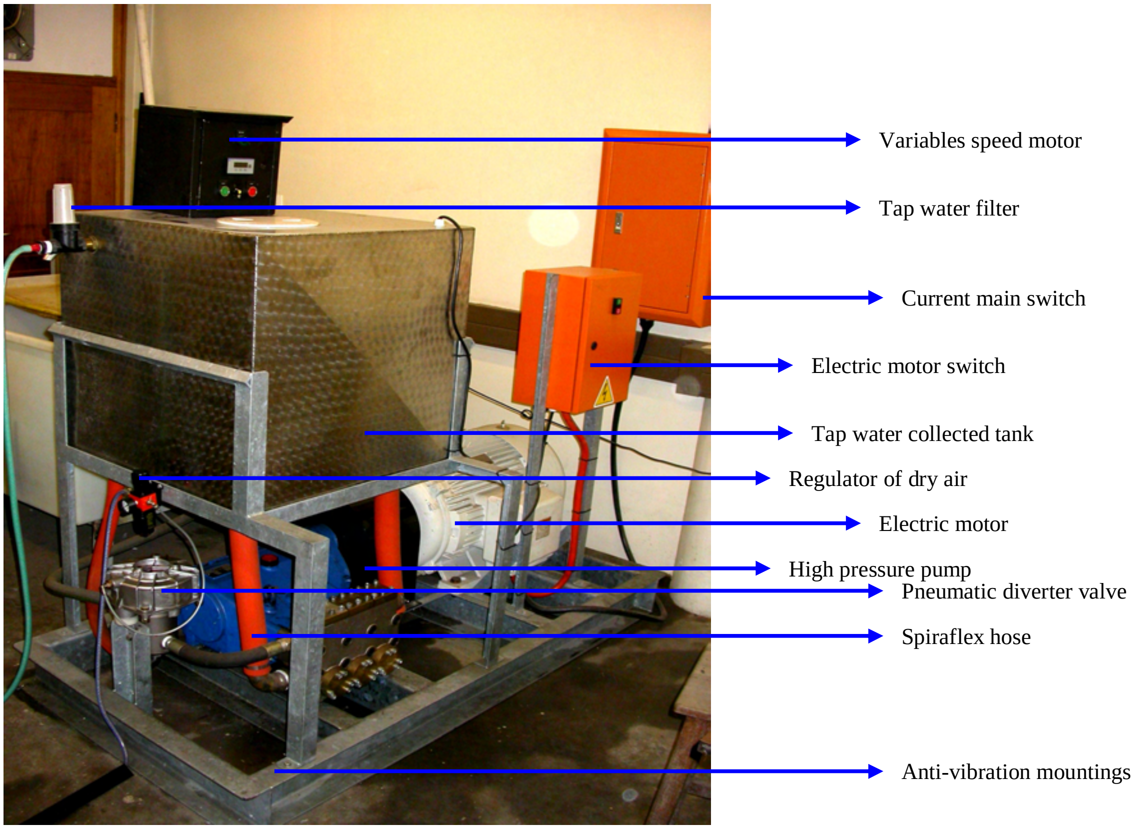

FIGURE 3.9: Photograph of the descaling assembly: pump and feed tank

3.3.4.1. Description of High Pressure Water Descaling Set-up

A schematic drawing of the descaling system is shown in Figure 3.10; the letters in the description below refer to the letters identifying different parts in the figure. The high pressure pump (J) was driven by a 55kW electric motor (L), Tap water (N) was filtered (K) and collected in a 400 litre sump (H) before each descaling run. Both pump and motor were fitted to a base frame mounted on anti-vibration mountings. The pressure/flow was adjusted via a pneumatic diverter valve (F). Dried compressed air from a regulator (G) actuated the diverter valve. High pressure water was piped from the pump unit to the hot steel samples through a 54 mm bore Spiraflex hose filled with two digital transmitters type 2020 TG (D) on either side of an orifice plate, which allowed the measurement of pressure and water flow rate. From the Spiraflex hose pipe water was sprayed through a single inclined nozzle (C). The nozzle was fixed to a steel rod by means of a coil-spring so that the nozzle height could be adjusted vertically; the nozzle was angled (15°, from vertical axis) [See figure 3.11]. The nozzle (LECHLER 694.726 with elliptical orifice) produced a water jet spray angle of 26° at 13.90 MPa. The vertical spray height was 96mm.

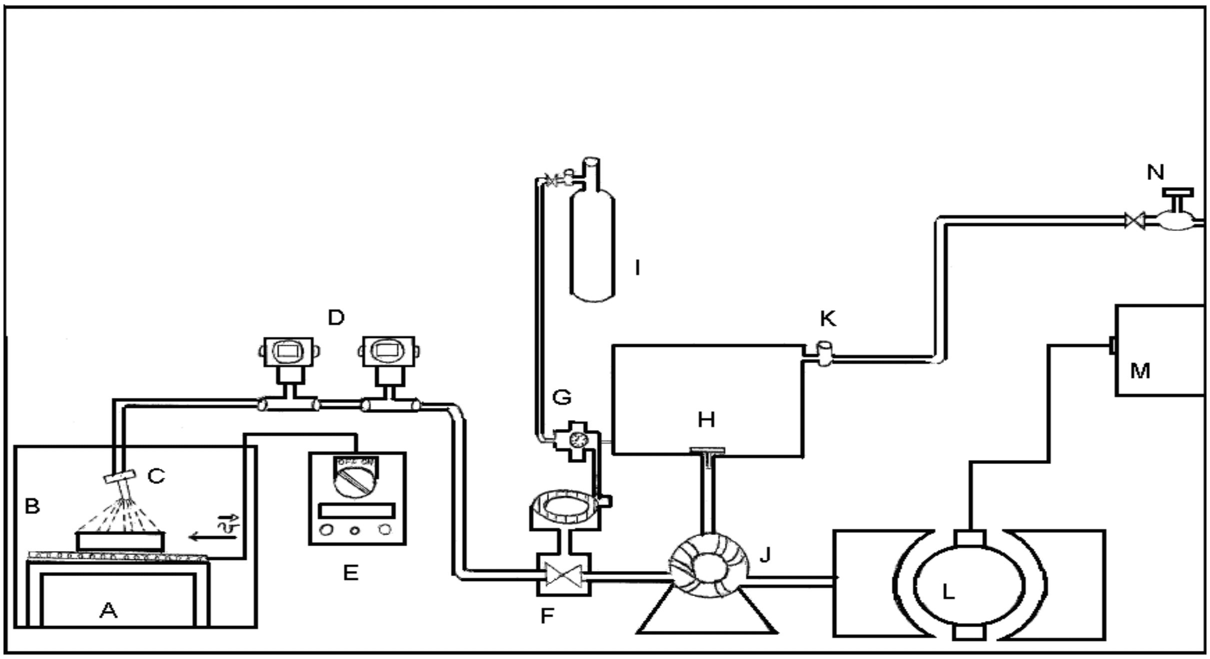

FIGURE 3.10: Schematic representation of the laboratory hydraulic descaler (not drawn to scale).

The hot steel sample for descaling was placed on a carriage (B) which moved underneath the descaling nozzle, by means of two parallel stainless steel runners. A variable speed motor and pulley (E) were used to propel the sample carriage (the speed was 0.8 m/s for stainless steel type 304). Upon descaling the water and scale fell into, and were collected in a 1050 litre holding tank (A).

3.4 EXPERIMENTAL RUN

3.4.1 Basic Matrix of Experiments

The experimental conditions for scale characterisation and for scale removal are shown in table 3.3 and 3.5 respectively.

Reheating for scale characterisation was performed at 1250ºC and 1280ºC using 3% and 4% free oxygen for 2, 3, 5 and 6 hours. Under these conditions, we expected to get a thick scale which should allow study of scale appearance, morphology and composition.

Descaling conditions were around 0.8m/s for the descaling speed, in line with the plant practice. Descaling vertical spray height was 96 mm and descaling water flow rate varied between 54 l/min and 66 l/min to get maximum impact pressures between 1.45 and 2.16 N/mm^2. The maximum impact pressure at the plant is 1.45 N/mm^2.

The basic outline of experiments is shown in table 3.3 below:

TABLE 3.3: Experimental matrix of reheating for scale characterisation

Temperature (ºC)	**% O_2**	**Reheating time (h)**
1250	3&4	2, 3, 5 & 6
1280	3&4	5 & 6

The experimental gas flow rate and rotameter settings used during reheating in 3%O_2 and 4% O_2 are given below:

TABLE 3.4**:** Gas flow rate and rotameter settings at 1 atmosphere for 3% and 4% free O_2 in the gas atmosphere

3%O_2	**Gas calibration & setting**	
	Gas flow rate	**Rot. setting**
N_2	3.92 dm^3/min	3.42 dm^3/min
O_2	0.16 dm^3/min	0.14 dm^3/min
CO_2	0.44 dm^3/min	0.32 dm^3/min

4%O_2	**Gas calibration & setting**	
	Gas flow rate	**Rot. setting**
N_2	3.91 dm^3/min	3.41 dm^3/min
O_2	0.22 dm^3/min	0.19 dm^3/min
CO_2	0.41 dm^3/min	0.33 dm^3/min

The basic outline of experiments is shown in Table 3.5 below:

TABLE 3.5: Experimental matrix for scale removal and descaling assessment

T[° C] Reheating	**% O_2 Reheating**	**Time[hr] Reheating**	**Descaling Speed [m/s]**	**Descaling Flow rate[l/min]**	**Descaling Spray height [mm]**
1250	3 & 4	2 - 6	0.8	54.40 - 65.96	96
1280	3 & 4	2 - 6	0.8	54.40 - 65.96	96
1300	3 & 4	2 - 6	0.8	54.40 - 65.96	96

Both descaling and reheating conditions were varied, but for the contaminated samples it was found that descaling effectiveness mainly depended on reheating conditions. Fifty-four experiments were done in total of which twenty-seven were for scale oxide characterisation, and twenty-seven were reheating followed with high pressure water spray for slab descaling. These were done under variable and constant reheating and descaling conditions.

3.4.2 Reheating Experiments

The temperature during reheating was generally monitored and controlled by means of the furnace thermocouple. However, in two runs an additional thermocouple was spot-welded to the sample surface, and it was found that the sample temperature was generally within 8°C of the furnace temperature.

The furnace was heated to the reheating temperature, and then the sample was placed in the furnace before starting gas flow. For both contaminated and uncontaminated samples, the temperature dropped (by about 15°C) when the sample was introduced and the gas flow was started - due to the opposing effects of the quenching effect of the introduction of non-preheated gas, and the exothermic scaling reaction. After approximately 8 minutes of the scaling, the temperature again reached its nominal value. At the end of the scaling period, the sample was removed from the furnace in a rapid and reproducible way, to avoid cooling before descaling.

3.4.3 Descaling Experiments

As mentioned earlier, the water pressure/flow during hydraulic descaling was monitored and controlled by a pneumatic valve.

Prior to descaling, the descaling water flow rate and system pressure were calibrated and monitored. The calibration procedure was as follows:

i. Set the pneumatic regulator valve pressure,
ii. Measure the level of water in the sump and the tank,
iii. Switch on the pump and use a stop watch to measure the water level variation in the tank and the sump,
iv. Read the corresponding pressures at the two digital transmitters,
v. Plot the curve of water flow rate versus regulator pressure and the curves of pressure at the first and the second transmitters versus the regulator pressure.

The photograph in figure 3.11 gives a view of the inside of the descaling tank.

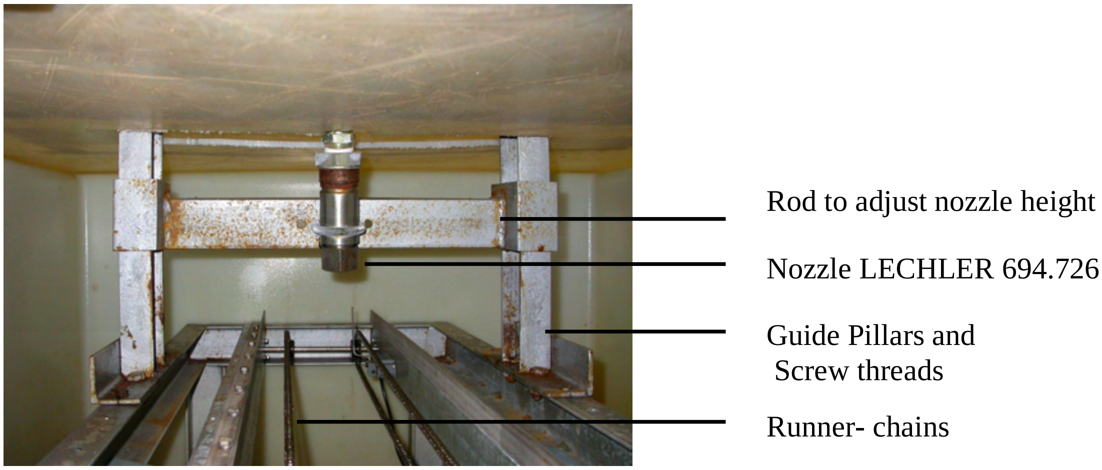

FIGURE 3.11: Descaling tank which shows the descaling nozzle, the adjustable spray height and the descaling speed chain.

The capacity of the high pressure pump used was 108 l/min of maximum water flow rate and 30 MPa pressure.

Table 3.6 below gives the descaling system pressure and water flow rate monitoring and calibration.

TABLE 3.6: Descaling system pressure and water flow rate calibration and setting

Pr	**P1s**	**P1**	**P2s**	**P2**	**Qt**	**Qb**	**ΔPs**	**ΔP**	**Qav**
[kPa]	[%]	[MPa]	[%]	[MPa]	[l/min]	[l/min]	[%]	[MPa]	[l/min]
49	13.9	8.3	13.7	8.2	40.4	44.3	0.12	0.072	42.4
137	26.0	15.6	25.8	15.5	55.2	57.6	0.18	0.108	56.4
196	38.6	23.1	38.3	23.0	66.6	70.9	0.225	0.135	68.8
245	43.4	26.0	43.1	25.9	71.3	72.4	0.24	0.144	71.9

Pr (kPa) dry air regulator pressure
P1s (%) setting pressure at the first digital transmitter
P1 (MPa) pressure at the first digital transmitter
P2s (%) setting pressure at the second digital transmitter
P2 (MPa) pressure at the second digital transmitter
ΔPs (%) variation of the setting pressure between two digital transmitters
ΔP (MPa) variation of the pressure between two digital transmitters
Qt (l/min) water flow rate measured at the first transmitter
Qb (l/min) water flow rate measured at the second transmitter
Qav (l/min) average water flow rate

Figures 3.12, 3.13 and 3.14 give the laboratory descaling calibration and settings curves. Figure 3.12 gives the water system pressure versus the pressure of dry air (read at the pressure regulator), Figure 3.13 gives the water flow rate at the descaling nozzle versus the air pressure (read at the pressure regulator), and Figure 3.14 gives the descaling water flow rates as a function of the difference in pressure between the second and the first transmitters

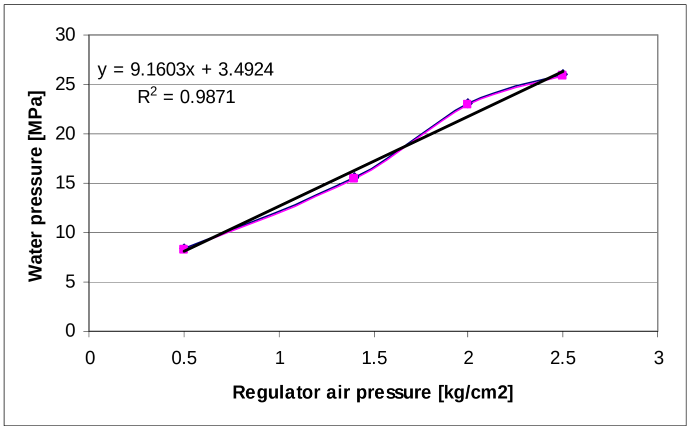

FIGURE 3.12: Water system pressure versus the regulator air pressure

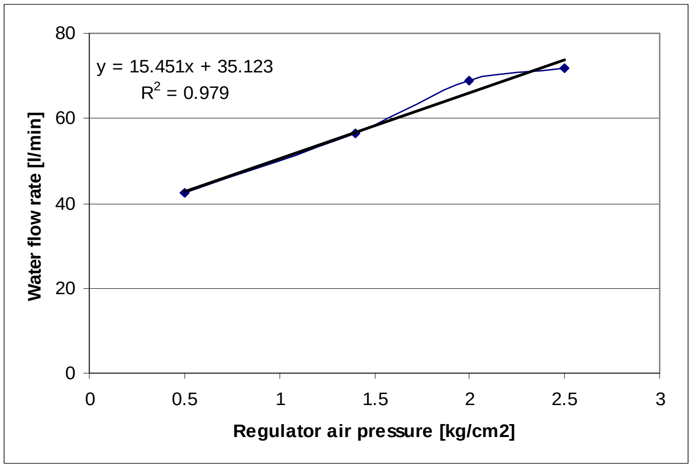

FIGURE 3.13: Descaling water flow rate versus the regulator air pressure

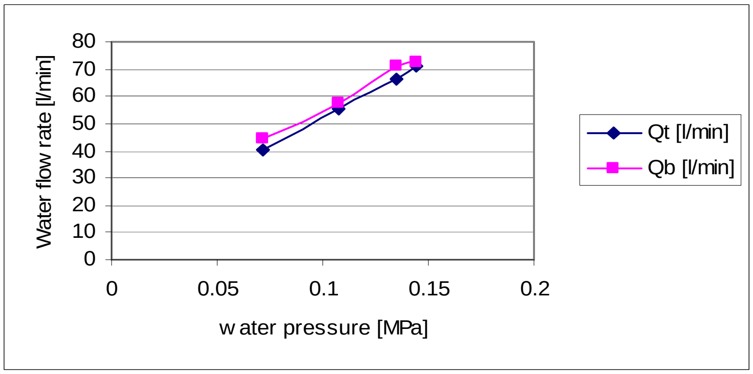

FIGURE 3.14: Descaling water flow rate versus the difference in pressure between the second and the first transmitter.

Two or three minutes before high pressure descaling the motor was started and the regulator air pressure manually set to the value which corresponded to the desired water flow rate. The hot sample was placed in the carriage and (quickly, and in a reproducible way) the motor pulley was started to move the hot sample at the require velocity until it reached the descaling nozzle. For a sample reheated at 1280°C, it was found that the sample temperature just before high pressure hydraulic descaling was approximately 1185°C. Just after descaling both the pump and the motor pulley were stopped. Once cold, descaled samples and the removed scales were collected for visual observation and analysis. The photograph on figure 3.15 shows a sample placed on the sample carriage.

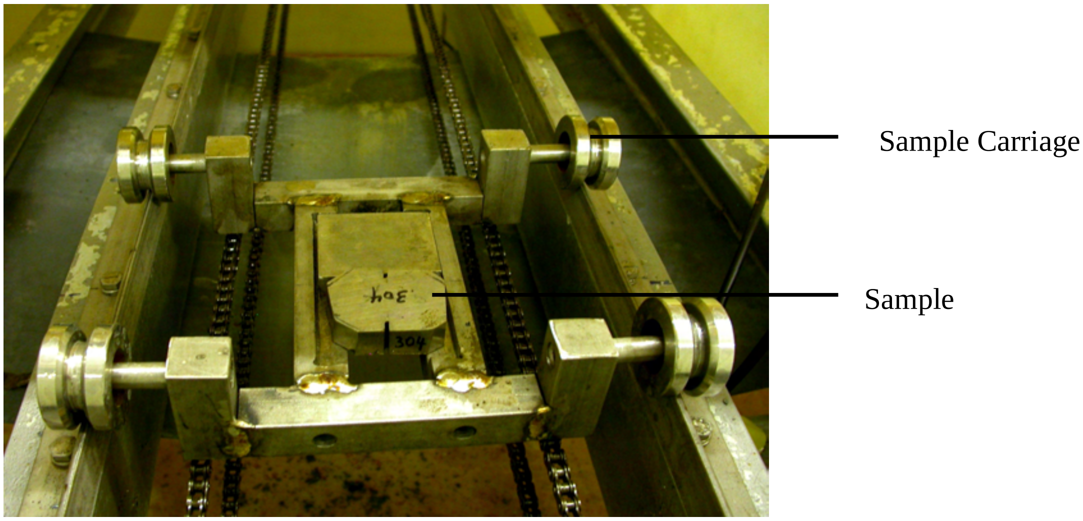

FIGURE 3.15*:* Sample placed on the descaling carriage which moves on the chain below the descaling nozzle

3.4.4 Analytical Techniques

After visual observation, descaled samples and removed scales were mounted in resin, and cross-sections polished for examination by scanning electron microscopy (SEM) in order to characterise the scale microstructure, composition and the metal-scale interfacial morphology. Scanning electron microscopy (SEM) observations were performed on a JSM-6300 scanning microscope. The specimens were mechanically polished using diamond paste, and some specimens were etched at room temperature for microstructure examination.

The average thickness of scale remaining on the descaled surfaces was found by means of image analysis (of SEM images). Energy-dispersive X-ray analysis (EDX) was used for point analyses of various phases in the scale.

X-ray diffraction (XRD) was used to identify scale and mould flux phases in contaminated and non contaminated samples. The target, voltage and current used were Co-Kα (Fe filter), 45kV and 40mA respectively.

Auger electron spectroscopy (AES) survey analyses were used to identify mould flux residues at the interface or in the scale. The beam voltage, beam current, tilt angle and the vacuum pressure used were 10kV, 10^{-6} A, 0° and 10^{-9} Torr, respectively. X-Ray photoelectron spectroscopy (XPS) survey, multiplex and deconvolution were used to determine the oxidation state of chromium in the removed scales.

X-ray fluorescence (XRF) and ICP-AES were used to analyse decarburized fluxes and scales after reheating. For XRF analysis, the oxide samples were ground to < 75µm in a tungsten carbide milling vessel, roasted at 1000°C to determine Loss On Ignition value and, after adding 1g sample to 6g $Li_2B_4O_7$, fused into bead. Major element analysis was executed on the fused bead using ARL9400XP + spectrometer. Another aliquot of the sample was pressed in a powder briquette for trace element analyses. Quantitative analyses of mould fluxes carbon and sulphur contents were done by means of LECO-Analysis.

Chapter 4: RESULTS AND DISCUSSION

4.1 REHEATING EXPERIMENTAL CONDITIONS AND RESULTS

The reheating conditions, for samples prepared for scale characterisation, are summarised in Table 4.1 (a list of symbols is given from p. xiii).

TABLE 4.1*:* Reheating conditions and mass gain results

Sample	**T[°C]**	**%O_2**	**mi [g]**	**t[h]**	**m_F [g]**	**Ss [cm^2]**	**e[cm]**	**ma[g]**	**Δm [g]**	**Gm [g/cm^2]**	**f_l[µm]**	**Cf [g/cm^2]**
S6	1250	4	93.928	2	0.194	11.31	1.3	95.09	0.968	0.086	66	0.017
S7	1250	4	85.425	2	0	11.31	1.3	86.8	1.375	0.122	0	0
S8	1250	3	82.734	2	0.194	9	1.3	83.702	0.774	0.086	83	0.022
S9	1250	3	68.749	2	0	9	1.3	70.124	1.375	0.153	0	0
S10	1250	4	68.896	2	0.192	12.87	1.3	71.11	2.022	0.157	57	0.015
S11	1250	4	72.074	2	0.183	8.4	1.3	73.593	1.336	0.159	84	0.022
S12	1250	4	71.424	2	0	12.87	1.3	73.761	2.337	0.182	0	0
S13	1250	3	62.884	2	0.163	14.82	1.3	64.108	1.061	0.072	42	0.011
S14	1250	3	134.26	2	0	12.87	1.3	136.88	2.619	0.203	0	0
R 1	1250	4	184.39	5	0.28	10.925	1.55	186.21	1.54	0.141	99	0.026
RP2	1250	4	130.19	3	0	12.95	1.3	134.25	4.06	0.314	0	0
RP3	1250	4	129.05	3	0.2	12.95	1.3	131.29	2.04	0.158	59	0.015
PR4	1280	4	166.81	6	0.16	18.81	1.2	172.02	5.05	0.269	33	0.009
RP5	1280	4	188.01	6	0	21.16	1.4	194.31	6.3	0.298	0	0
RP8	1280	4	160.08	6	0.22	14.85	1.4	164.09	3.79	0.256	57	0.015
RST14	1280	4	163.87	5	0.24	15.6	1.3	166.76	2.65	0.170	59	0.015
RST13	1280	4	157.77	5	0.23	15.66	1.3	163.31	5.31	0.339	57	0.015
RST100	1280	4	180.55	5	0.3	18.18	1.3	183.6	2.75	0.151	64	0.017
RTS100	1280	4	180.02	5	0.31	18.18	1.3	183.6	3.27	0.180	66	0.017
RTS99	1280	4	178.95	5	0.325	19.825	1.15	182.36	3.085	0.156	63	0.016
RTS122	1280	4	165.44	5	0.27	16.66	1.3	170.07	4.63	0.262	62	0.016
RST10	1280	4	182.5	6	0.33	19.04	1.3	183.6	3.58	0.188	67	0.017
RTS9	1280	4	179.7	6	0.30	18.25	1.15	182.36	3.08	0.169	63	0.016
RTS12	1280	4	175.4	6	0.32	20.04	1.3	170.07	4.63	0.231	62	0.016
PR1	1250	3	170.8	2	0.08	15.43	1.2	172.02	5.05	0.327	20	0.005
R2	1250	4	135.2	6	0.163	14.76	1.3	138.41	3.05	0.206	43	0.011
R3	1250	4	132.8	6	0	12.87	1.3	137.38	4.58	0.356	0	0

X-Ray diffraction analysis for phase identification of the detached scale (after cooling in the nitrogen-flushed box) was performed on solid scale oxides (see Appendix 4**).** Surface analyses (XPS) were done to determine the chromium oxidation state (see Appendix 5). Scanning electron microscopy (SEM-BSE, SEM-SEI and SEM-EDS) was performed to assess scale morphology, interfacial roughening and for elemental analysis of the scale-steel interface.

The following general observations were made: The effects of the different fluxes (industrial and synthetic) were similar. Visual examination of the samples after reheating and descaling showed that all synthetic fluxes gave better descaling (than for uncontaminated samples), and especially so the flux SMF1.

Even a small coverage of mould flux contaminant on steel surface was found to facilitate descaling. However, for average coverage below 20 µm the mould flux effect was found to break down, and descaling was difficult.

Figure 4.1 illustrates the scale layers on the steel after high temperature oxidation.

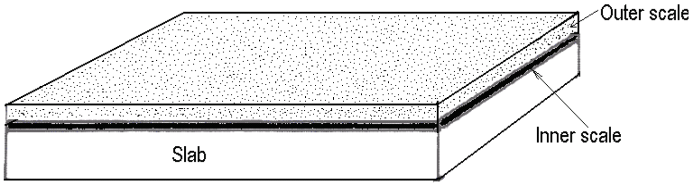

FIGURE 4.1: Sketch of the scale layers formed on the surface of the reheated sample.

Results of XRF analysis of the outer scale removed from the samples are presented in table 4.2. These samples were obtained after reheating of uncontaminated samples and contaminated samples (with mould flux type RF1) at 1250°C, 4% O_2 for 2 hours.

TABLE 4.2: XRF- analysis of the removed outer scale after cooling the sample in a nitrogen-flushed box following reheating at 1250°C for 2h, with 4% O_2 in gas.

%	S6	S7	S10	S11	S12
	Flux RF1	**No Flux**	**Flux RF1**	**Flux RF1**	**No Flux**
Cr_2O_3	12.820	7.500	9.730	10.850	12.510
Fe_2O_3	76.520	85.980	81.700	77.880	78.990
NiO	5.470	3.640	4.520	4.450	5.020
SiO_2	1.060	0.237	0.807	1.860	1.030
CaO	0.702	0.002	0.468	1.690	0.084
MnO	2.06	1.96	1.64	1.94	1.66
MgO	0.038	0.022	0.023	0.047	0.021
Na_2O	0.232	0.099	0.167	0.318	0.080
K_2O	-	-	0.004	0.011	0.005
Al_2O_3	0.142	0.005	0.363	0.254	0.113
V_2O_5	0.12	0.013	0.12	0.12	0.012
MoO_3	0.30	0.01	0.22	0.33	-
TiO_2	0.03	0.02	0.02	0.03	0.01
P_2O_5	0.45	0.43	0.2	0.15	0.36
SO_3	0.03	0.03	0.03	0.08	0.09
CuO	0.05	0.06	0.03	0.05	0.06
Total	100	100	100	100	100

The thicknesses of the removed outer scale on sample S6 (contaminated sample) and S7 (uncontaminated sample), both reheated for two hours, were measured after the outer scales were detached from the upper surfaces of these samples. The outer scale removed from S7 (uncontaminated) was 0.2mm thick and the scale remaining on the sample was 0.44mm thick, giving a total scale thickness of 0.64 mm on the upper sample surface after reheating. For sample S6 (contaminated), the removed scale was about 0.4mm thick, and the scale remaining on this sample was around 0.1mm thick, for a total scale thickness of 0.5 mm. This slight decrease in the extent of oxidation for samples with mould flux was also found for different reheating conditions, as discussed later in this chapter. The difference in behaviour between contaminated and uncontaminated slabs was also visible for short reheating times. For contaminated samples reheated for 2 hours with 3% free oxygen at 1250°C, some parts of the steel surface were found to be unoxidized, indicating a protective effect of the mould flux.

Similar XRF analyses were performed on the outer scales on the steel after reheating contaminated and uncontaminated samples, for mould flux type 832 and synthetic mould fluxes SMF1, SMF2 and SMF3. The results are presented in table 4.3. Samples RP2 and RP3 were reheated at 1250°C, for 3h, 4% O_2 in gas (the latter covered with flux type 832; C_f = 0.015g/cm^2). Samples RP5 and RP8 (the latter covered with flux type 832; C_f = 0.015g/cm^2) were reheated at 1280°C, for 6h, 4% O_2 in gas. Samples RTS99 (covered with synthetic flux containing 20% Na_2O), RTS 100 (synthetic flux with 20% CaF_2) and RTS122 (synthetic flux with 50% CaO-50% SiO_2) were reheated at 1280°C, for 5h, 4%O_2 in gas.

TABLE 4.3: XRF analyses of outer scale after reheating, for uncontaminated samples, and samples contaminated with industrial and synthetic mould fluxes. See text for detail of reheating conditions.

	RP2	**RP3**	**RP5**	**RP8**	**RTS99**	**RTS 100**	**RTS 122**
	No flux	Flux Type 832	No flux	Flux type 832	Flux SMF2	Flux SMF1	Flux SMF3
SiO_2	0.33	1.63	0.32	1.62	0.87	2.50	3.67
TiO_2	<0.01	0.02	0.01	0.03	0.01	0.04	0.02
Al_2O_3	<0.01	0.19	0.03	0.19	0.09	<0.01	0.09
Fe_2O_3	75.40	72.76	75.99	69.92	77.49	66.53	70.04
MnO	1.98	1.96	1.68	1.71	1.47	1.73	1.70
MgO	1.18	<0.01	<0.01	<0.01	<0.01	<0.01	<0.01
CaO	0.50	2.08	0.26	2.70	1.84	4.29	3.37
Na_2O	<0.01	<0.01	<0.01	<0.01	<0.01	<0.01	<0.01
K_2O	0.02	0.01	<0.01	<0.01	0.03	<0.01	<0.01
P_2O_5	0.88	0.75	0.74	0.94	0.78	0.93	0.66
Cr_2O_3	12.77	14.79	15.92	17.27	11.91	18.43	13.86
NiO	4.90	5.06	4.72	4.88	5.07	4.82	5.93
V_2O_5	0.10	0.11	0.12	0.15	0.16	0.13	0.12
SO_3	1.45	0.23	0.09	0.44	0.13	0.12	0.17
MoO_3	0.36	0.30	0.06	0.02	0.03	0.41	0.31
Cl	0.07	0.01	<0.01	0.03	0.03	0.03	0.01
CuO	0.06	0.07	0.07	0.07	0.07	0.04	0.07
Total	100	100	100	100	100	100	100

The XRF results in table 4.3 show that, for similar reheating conditions, there is little difference between the composition of the outer scale on samples with or without mould flux residues, apart from the presence (as expected) of CaO and SiO_2 in the scale of samples which had been contaminated with mould flux. The bar graphs in figure 4.2 and figure 4.3 illustrate the slight differences in mass percentage observed in tables 4.2 and 4.3 between the components of the removed outer scales on uncontaminated and contaminated samples.

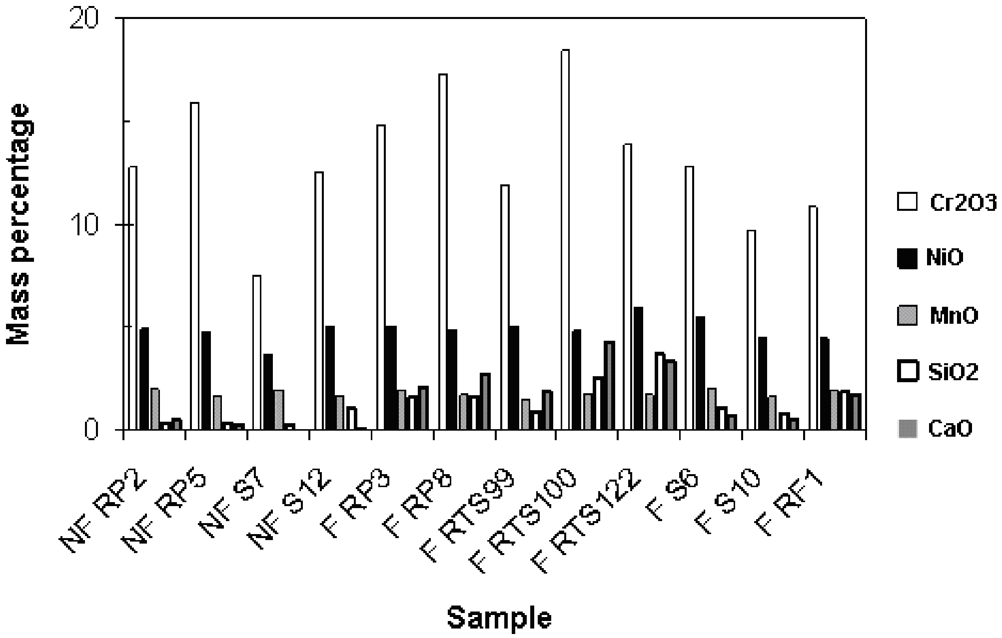

FIGURE 4.2: Mass percentage of Cr_2O_3, NiO, MnO, SiO_2 and CaO components of the removed outer scales on uncontaminated and contaminated samples

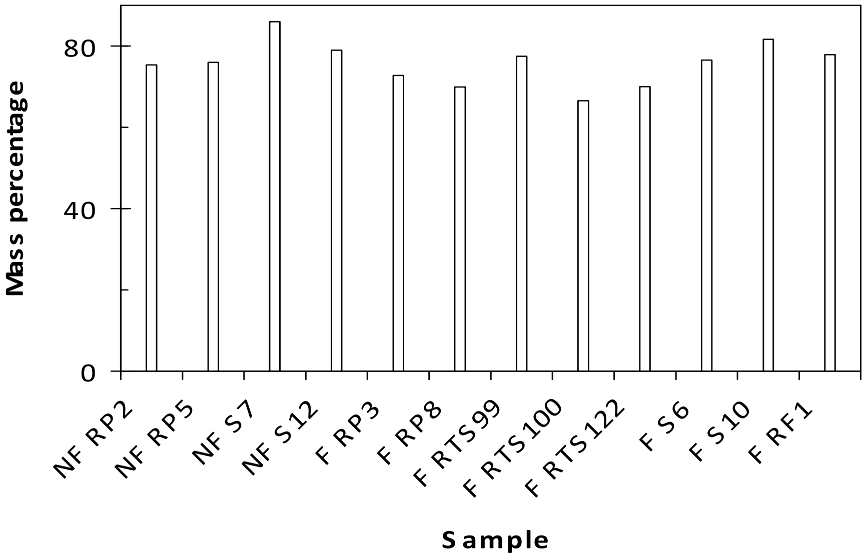

FIGURE 4.3: Mass percentage of Fe_2O_3 of the removed outer scales on uncontaminated and contaminated samples

Using SEM-EDS microanalyses on contaminated samples, residual mould flux was found at the steel-scale interface (see section 4.2.2.3 for details) and at the interface of two scale layers, Platinum wire markers, that had been placed on the sample surface before reheating were located at the interface of the inner and outer scale layers - demonstrating that the outer scale grew by cation diffusion, and the inner scale by internal oxidation.

4.2 DISCUSSION OF THE REHEATING RESULTS

4.2.1 Introduction

In this section, XRD analysis of the outer and inner scale layers, SEM-BSE micrographs of reheated samples close to scale-steel interface, and SEM-EDS[1] results in the scales are presented and discussed. Scales thicknesses were also measured.

4.2.2 Scale Characterisation

4.2.2.1 Thickness of Scales

Typical scale thicknesses after reheating in 3%O_2, for 6h at 1280°C, followed by descaling of samples D20 and D21 (SP =13.94 MPa, U = 26.22 l/m^2, I = 1.45 N/mm^2), were as follows:

---

[1] The light elements carbon, oxygen and fluorine were not analysed by SEM-EDS.

For the uncontaminated samples the removed scale was 875 µm thick, and the residual scale thickness was 580 µm, giving a total scale thickness after reheating of 1.455 mm. For the contaminated samples the removed scale was 1100 µm thick, and the residual scale thickness was 30 µm (in only a few places on the metal substrate; many places had essentially no residual scale), so up to 1.130 mm of scale had formed during reheating. This confirms the effect of mould flux residues to decrease oxidation slightly. Measurement of the decrease in sample thickness after reheating confirmed that the presence of mould flux causes a slight decrease in the scale growth rate.

From XRD analysis (see Figures 4.4 and 4.5) of the removed scales from the contaminated and the non contaminated samples, in both scale there were spinels (chromite) in the inner scales, and magnetite and haematite in the outer scale.

The outer scales were similar in phase composition (in line with the similarity in chemical composition, as reported in Tables 4.2 and 4.3), but the inner surfaces of the removed scales were quite different: metal phase (Ni-enriched tendrils, denoted by Fe γ in Figure 4.4) was found in the inner scale of the uncontaminated samples only, and not in the contaminated samples. This agrees with the microscopic appearance of scale cross-sections, as presented in the next section.

XRD-spectra of the underlying metal surface (with residual scale) and of the bottom of the removed scale showed in addition to the austenite phase, the presence a spinel phase on the non contaminated steel.

For the contaminated steel, XRD-spectra of the underlying metal and the bottom of the removed scale showed austenite and eskolaite (Cr_2O_3) (labelled “Fe_2O_3” in figure 4.4) and spinel (Figures in appendix 3).

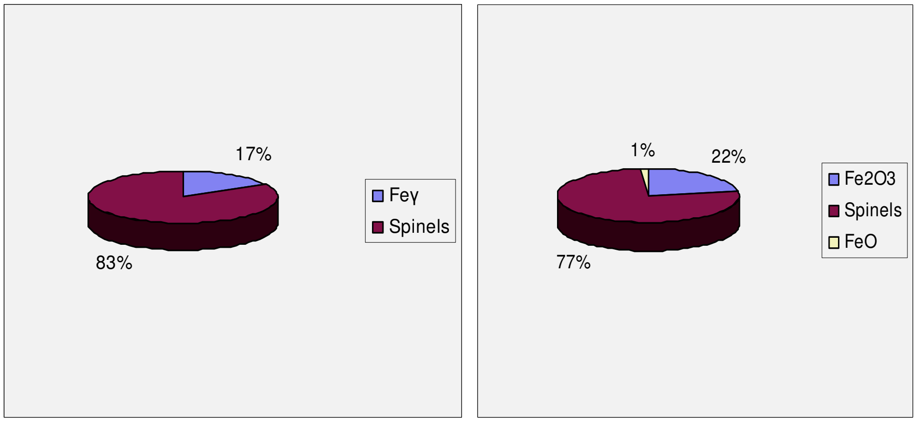

FIGURE 4.4: Phase compositions, from XRD, of the inner surface of the removed scale for the uncontaminated (left) and contaminated samples (right).

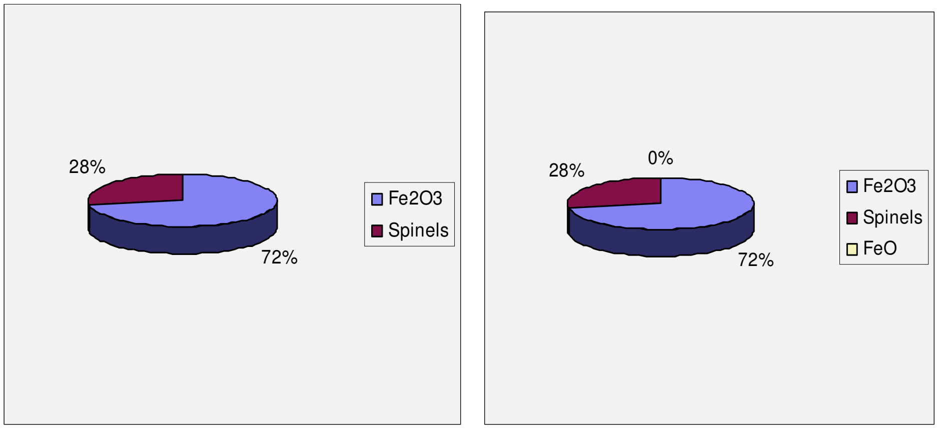

FIGURE 4.5: Phase compositions, from XRD, of the outer surface of the removed scale for the uncontaminated (left) and contaminated samples (right).

4.2.2.2 Microanalyses: Uncontaminated Sample after Reheating

Figure 4.6 shows a micrograph of the structure of the inner scale on an uncontaminated sample; the scale is towards the upper part of the image and the metal substrate towards the bottom part. Close to the scale-metal interface the scale mainly contained two phases: chromite (Fe-Cr spinel), originally formed along austenite grain boundaries by internal oxidation (darker phase), and metal tendrils formed by enrichment of the nobler metal (Ni) enrichment at the interface scale-metal substrate (bright phase). The composition of these two phases varies somewhat from the inner scale to the outer scale, but the metallic phase (tendrils) is always rich in Fe and Ni and the oxide phase (chromite) is rich in Fe and Cr.

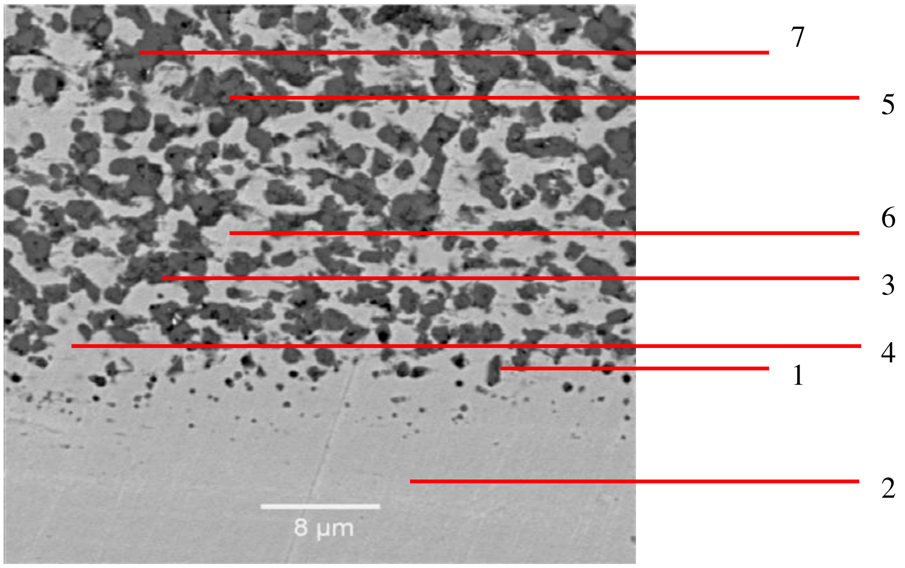

FIGURE 4.6: SEM backscattered electron micrograph of reheated sample – scale-steel interface; sample RP5 (no flux, 1280ºC, 4% O_2, 6h); analyses in Table 4.4.

TABLE 4.4: Average composition of different scale phases after reheating of uncontaminated sample (95% confidence intervals given). Sample RP5, 1280°C, 4%O_2, and 6h.

	Cr	**Ni**	**Fe**	**Si**	**Ca**	**V**	**Mn**
Point 2	4.1±1.7	14±4	81±2.5	0.2±0.12	0.1±0.14	0.02±0.14	0.21±0.3
Oxide 1	29.8±4.5	4.4±1.6	49.7±3.5	5.2±1.8	0.04±0.06	0.1±0.04	10.6±2.8
Oxide 3	52±5	1.4±1.4	38.4±6	1.4±1.3	0.12±0.15	0.8±0.7	5.9±3
Oxide 5	57.1±4.3	0.5±0.4	37.2±6	1.3±1.1	0.08±0.14	0.54±0.3	3.3±2.3
Tendril 4	8.5±4.9	11.74±2	78.9±3.5	0.33±0.3	0.06±0.1	0.12±0.2	0.42±0.5
Tendril 6	4.7±2.4	14.4±2.2	80±2.7	0.3±0.3	0.0±0.0	0.12±0.15	0.6±0.6
Point 7	11.9±3.4	0.9±0.4	82±6.8	2.55±5.4	0.08±0.1	0.16±0.2	2.4±1.5

4.2.2.3 Microanalyses: Contaminated Samples after Reheating

Figure 4.7 gives a micrograph of the inner scale on a sample which had been contaminated with mould flux before reheating. Comparison with Figure 4.6 (uncontaminated sample) shows the major difference to be the absence of Ni-enriched tendrils on the contaminated surface.

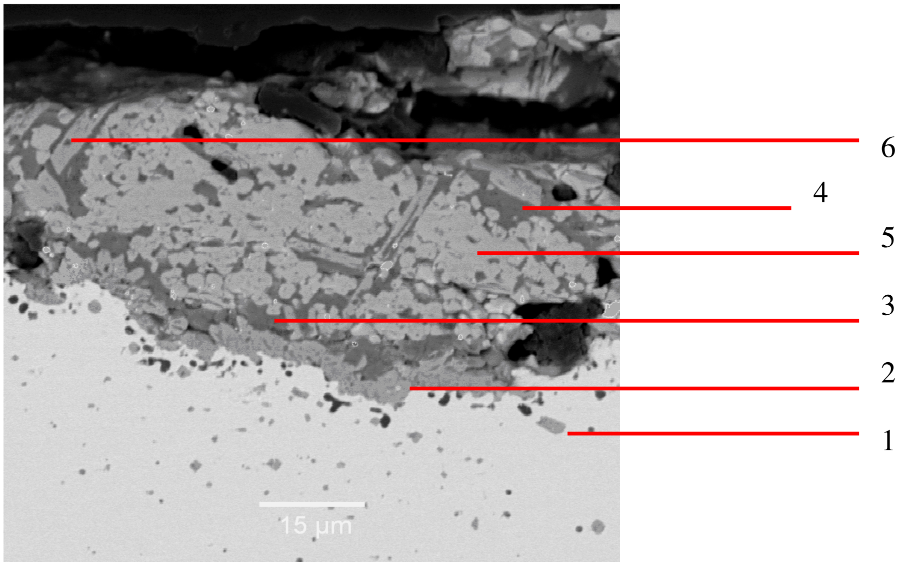

FIGURE 4.7: SEM backscattered electron micrograph of reheated slab sample – scale-steel interface; sample RP8 (flux type 832, 1280°C, 4%O_2, 6h); analyses in Table 4.5.

TABLE 4.5: Average composition of different scale phases after reheating of contaminated sample (95% confidence intervals given). Sample RP8, flux type 832, 1280°C, 4%O_2, $C_f = 0.015 g/cm^2$, 6h

	Cr	**Ni**	**Fe**	**Si**	**Ca**	**Na**	**Mn**
Internal Oxide 1	56.36±2.9	1.28±0.6	13.56±6.4	0.18±0.1	0.18±0.05	0.0±0.0	26.87±4.1
Interface 2	90.18±4.3	0.14±0.2	7.84±4.7	0.32±0.1	0.5±0.08	0.02±0.5	0.6±0.15
Flux 3	7.75±8.54	0.45±0.24	3.68±1.88	32.95±2	54.53±8	0.15±0.08	0.35±0.26
Flux 4	9.9±7.89	1.7±0.31	6.5±2.5	30.6±3	50.2±8	0.1±0.1	0.8±0.2
Oxide 5	40.13±0.6	16.1±0.5	38.38±0.5	0.33±0.3	0.63±0.24	1.5±0.3	4.35±0.5
Oxide 6	72.3±4.4	0.83±0.51	24.95±5.3	0.58±0.77	0.8±0.63	0.13±0.21	0.35±0.33

The internal oxide (point 1 in Figure 4.7) was similar in composition to that in the uncontaminated sample. However, other phases are present in the contaminated sample which are not found on the uncontaminated sample:

An oxide layer at the scale-steel interface – nearly pure chromium oxide (point 2).

Mould flux residues (points 3 and 4), with dissolved Cr, Ni and Fe; the absence of Na in the remnant flux is probably due to the volatilisation.

Mixed Ni-Cr-Fe-Mn oxide (point 5): Dominant mid-grey phase away from interface; apparently steel of which the oxidation was enhanced by mould flux.

Needle like crystals within the scale (point 6): These are rich in Cr (they are probably chromite, but with a higher Cr content than the spinel in the uncontaminated sample)

Similar scale structures were found for samples contaminated with synthetic mould fluxes, as detailed below in Tables 4.6, 4.7 and 4.8 and Figures 4.8, 4.9 and 4.10.

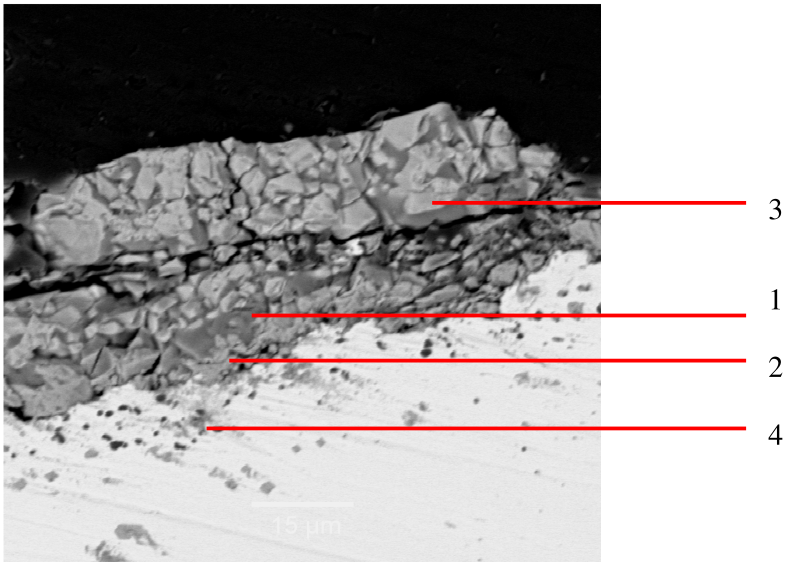

Figure 4.8: SEM backscattered electron micrograph of reheated contaminated sample – scale-steel interface; sample RTS9 (synthetic flux SMF2 with 20% Na_2O); analyses in Table 4.6.

TABLE 4.6: Average composition of different scale phases after reheating of contaminated sample (95% confidence intervals given), Sample RTS9, 20% Na_2O synthetic flux SMF2, 1280°C, 4%O_2, 6h, $C_f = 0.016 g/cm^2$.

	Cr	**Ni**	**Fe**	**Si**	**Ca**	**Na**	**Mn**
Internal oxide 4	52.53±1.5	1.93±0.74	18.78±2.3	1.35±1.8	0.3±0.2	0.05±0.01	23.88±3
Interface 2	86.98±4.5	0.93±0.8	8.8±2.4	0.78±0.8	0.85±0.64	0.2±0.19	0.28±0.28
Oxide 3	49.5±1.9	18.23±1.2	28.4±1.39	0.48±0.17	0.55±0.24	0.28±0.47	2.45±0.89
Flux 1	9.49±5.9	1.53±2	18.2±2.12	42.65±6	20.73±1.7	5.35±0.7	0.63±0.7

The scale on the sample contaminated with the Na_2O-containing synthetic flux (Table 4.6) contained the following phases:

The internal oxide (point 4) was similar in composition to that in the uncontaminated and other contaminated samples.

Nearly pure chromium oxide was found at the scale-steel interface (point 2), as for the sample contaminated with the commercial flux (Figure 4.7 and Table 4.5).

Similarly, the mould flux remnant (point 1) had lowered Na, and contained dissolved Cr, Ni and Fe, and the dominant mid-grey oxide away from interface (point 3) was a mixed Cr-Fe-Ni-Mn oxide.

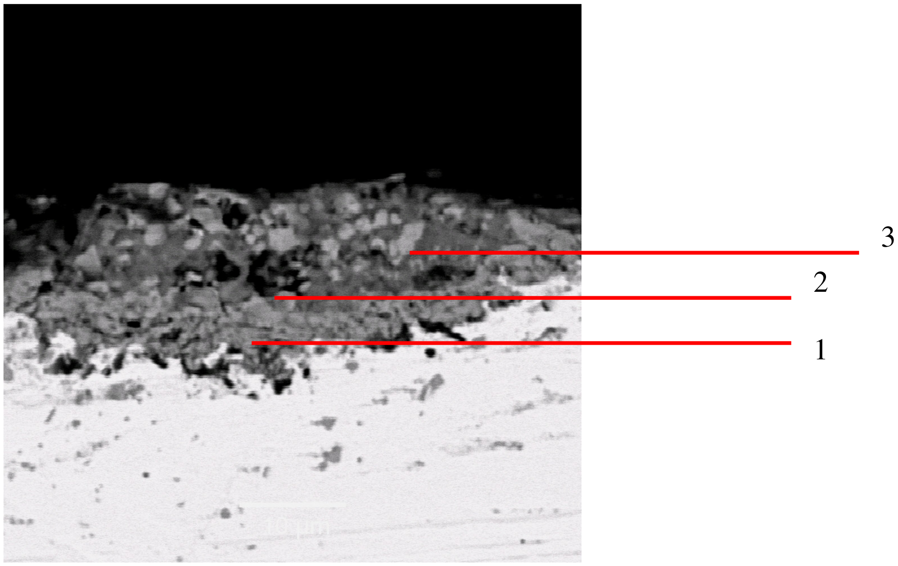

FIGURE 4.9: SEM backscattered electron micrograph of reheated sample – scale-steel interface; sample RST 10 (synthetic flux SMF1 with 20% CaF_2); analyses in Table 4.7.

TABLE 4.7: Average composition of different scale phases after reheating contaminated sample (95% confidence intervals given). Sample RST10, 20% CaF_2 synthetic SMF1, 1280°C, 4%O_2, 6h, $C_f = 0.017 g/cm^2$

	Cr	**Ni**	**Fe**	**Si**	**Ca**	**Na**	**Mn**
Interface 1	91.28±3.8	0.46±0.5	5.04±3.2	0.72±0.6	0.96±0.6	0.24±0.3	0.86±0.6
Flux 2	28.2±4	0.33±0.2	13.5±2.6	22.6±1.5	34.2±1.3	0.28±0.28	0.73±0.6
Oxide 3	42.1±70	5.45±2	40±6.3	1.2±0.6	2.63±0.7	0.03±0.05	8.3±20

The scale on the sample containinated with the CaF_2-containing synthetic mould flux (Figure 4.9 and Table 4.7) had three major phases:

Nearly pure Cr oxide at the scale-steel interface (point 1).

Mould flux residue, containing dissolved Cr, Fe and possibly Ni (point 2).

Cr-Fe-Mn-Ni mixed oxide away from the interface (point 3).

The scale on the sample containinated with the CaO-SiO_2 synthetic mould flux (Figure 4.10 and Table 4.8) had similar phases:

Internal oxidation product (point 4): Cr-Fe-Mn oxide, as in the other samples.

Nearly pure Cr oxide at the scale-steel interface (point 1).

Mould flux residue, containing dissolved Cr, Fe and Ni (point 2).

Fe-Mn-Ni mixed oxide away from the interface (point 3).

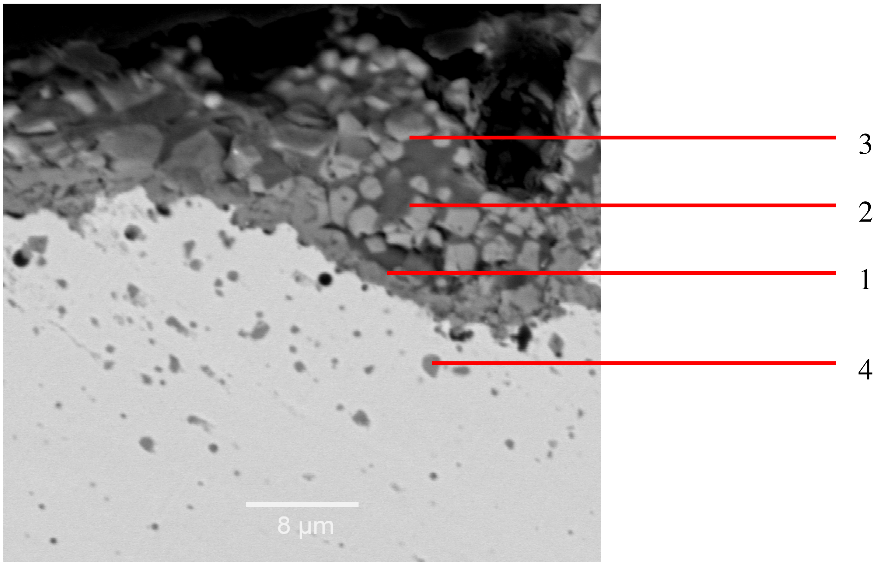

FIGURE 4.10: SEM backscattered electron micrograph of reheated sample – scale-steel interface; sample RTS 12 (50%CaO-50%SiO_2 synthetic mould flux SMF3); analyses in Table 4.8.

TABLE 4.8: Average composition of different scale phases after reheating of contaminated samples (95% confidence intervals given). Sample RTS 12, 50%CaO-50%SiO_2 synthetic mould flux SMF3 (6h, 1280°C, 4%O_2, $C_f = 0.016$ g/cm^2).

	Cr	**Ni**	**Fe**	**Si**	**Ca**	**Na**	**Mn**
Internal oxide 4	57.73±4.1	0.93±0.6	9.53±3.5	0.35±0.6	0.73±0.2	0.4±0.5	28.93±3
Interface 1	89.83±4.2	0.5±1	5.1±2.5	1.03±1.6	1.63±0.8	0.2±0.34	1±1.34
Flux 2	13.75±8	3.75±1.97	15.68±1.4	29.8±4.9	35.83±4	0.1±0.2	0.8±0.89
Oxide 3	54.55±1.5	11.35±1.7	29.8±2.3	0.53±0.4	1.38±0.2	0.68±1.1	1.38±0.98

Figure 4.11 illustrates internal oxidation after reheating at 1280°C for 6 h with 4%O_2 in the gas phase. The micrographs are for an uncontaminated sample, a sample contaminated with industrial flux type 832, and a sample contaminated with synthetic flux SMF2. From these images, there appears to be a tendency for a greater depth of internal oxidation in the presence of the mould flux. However, this effect was not quantified in this work.

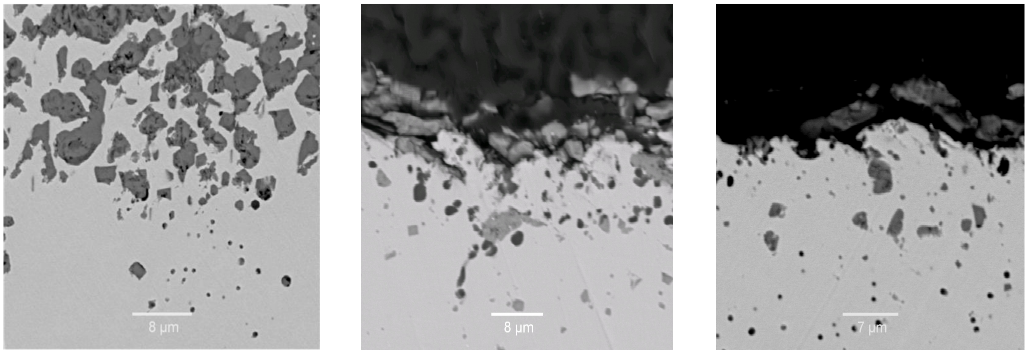

No Flux (RP5) Industrial flux (RP8) Synthetic flux (RST10)

FIGURE 4.11: Sample appearance (scale-steel interface) after reheating under similar conditions. Surface condition (from left to right): uncontaminated; contaminated with industrial flux (type 832); and contaminated with synthetic flux (SMF2). Backscattered electron images.

4.2.3 Summary of differences in scale structure

The difference in interfacial roughening (as distinct from tendril formation) between uncontaminated and contaminated samples was relatively small. In contaminated samples roughness at the interface generally appeared to be slightly greater than in the uncontaminated samples.

The difference in scale microstructure is illustrated by figure 4.12 and figure 4.13 below (scale is towards the upper part of the images and the metal substrate towards the lower part):

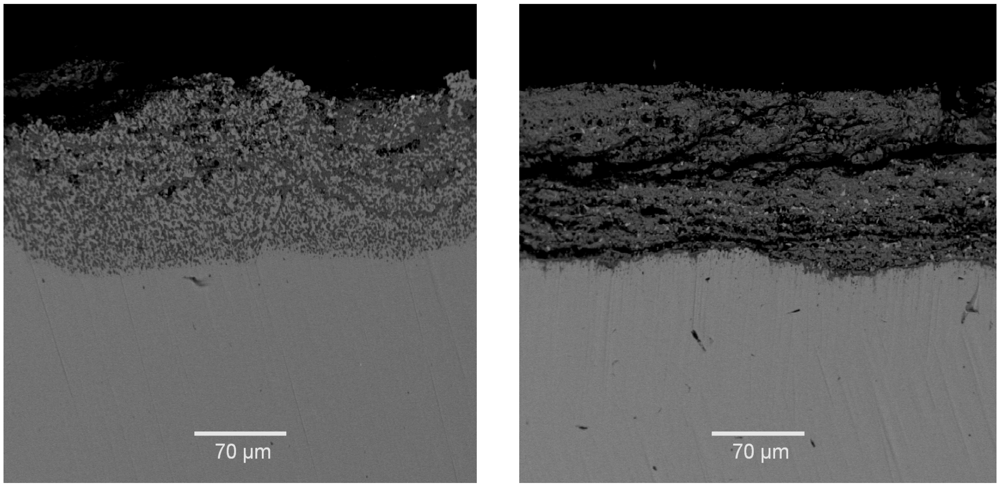

FIGURE 4.12: Difference in scale morphology for uncontaminated sample S7 (left) and contaminated sample S6 (right), after 4 hours reheating with 4 % free oxygen at 1250°C. Backscattered electron images.

The scales for contaminated and uncontaminated samples are very different, both in internal structure, and with respect to the compositions of the oxide phases. The absence of Ni-enriched tendrils in the scale of fluxed slab surfaces is a striking effect, with clear implications for descaling effectiveness. This effect apparently arises because mould flux contamination enhances the oxidation of nickel and chromium. Usually upon reheating nickel (being more noble than iron) accumulates in the remaining metal, while chromium (being less noble metal than iron) forms chromite by internal oxidation, at sites which include austenite grain boundaries. Both of these effects appear to be suppressed by the presence of mould flux on the sample surface: nickel in the scale is oxidised, and is not present in metal tendrils, and chromium oxide forms a continuous inner scale, between the mould flux remnants and the steel. In addition to the images shown in the previous section, further micrographs are given here to emphasise the differences.

For the uncontaminated samples, the inner scale exhibited scale entanglement with tendrils of unoxidized metal (see Figure 4.13), as expected from the high nickel content of this steel. In Figure 4.13 the metal tendrils are visible as the lighter regions entwined with darker oxide (chromite). Close to the steel-metal interface these tendrils typically contained 5-9% chromium and 12-14% nickel (balance iron).

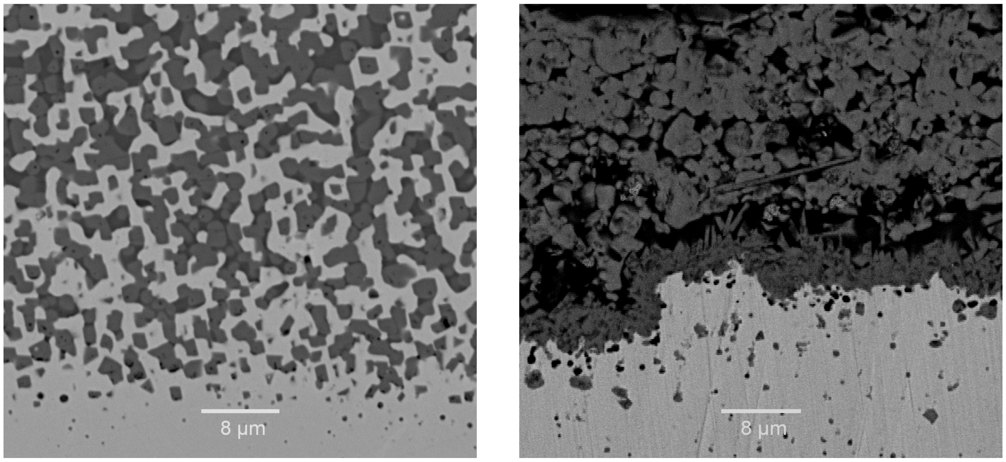

FIGURE 4.13: Appearance of the scale-steel interface on uncontaminated sample R3 (left) and contaminated sample R2 (right) after reheating at 1250°C, 4% O_2, 6 hours. Backscattered electron images.

In line with previous results (Pistorius *et al.*, 2003) narrow paths through the scale were found to be free of the nickel-enriched tendrils; these paths - corresponding to chromite in composition - follow the former austenite grain boundaries, and extend into the metal beyond the macroscopic scale-steel interface (see arrows in figure 4.14). These chromite paths should facilitate the descaling of non-contaminated samples to some extent.

For contaminated samples, close examination of the steel-scale interface did not reveal any oxide penetration into the steel, tendrils of unoxidised metal or the presence of the metal free paths-corresponding to chromite (see figures 4.13 and 4.14). In this case, however, there were longitudinal cracks (fissures) formed parallel to the surface (see figure 4.12). These would favour complete or partial descaling, depending on the location of the cracks close to or near the metal-scale interface. A complex structure can be seen at the scale-steel interface which contains needles, nodules, voids and discontinuities within the body of the scale (see figures 4.13 and

4.14). It is unclear whether these voids formed during reheating, or whether particles of scale were lost during sample preparation despite the precautions taken. Taniguchi (1985) claimed that the porosity or interfacial voids can bring the loss of adhesion and facilitate scale removal.

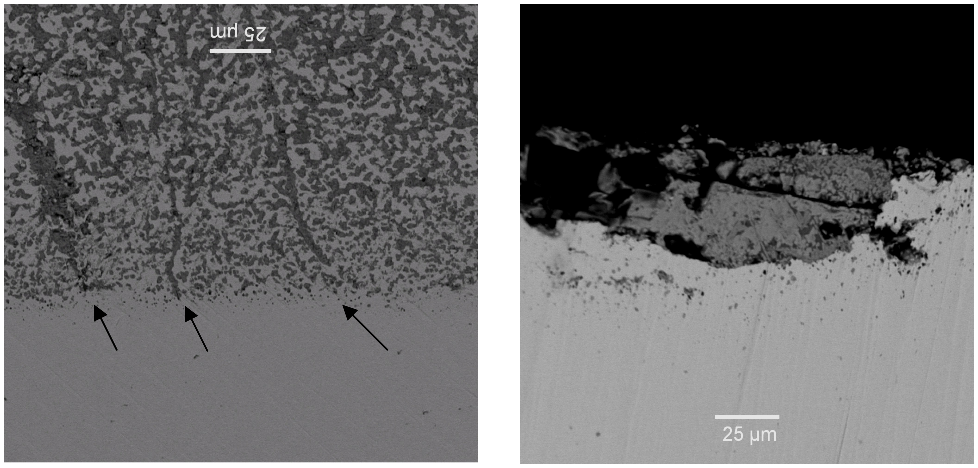

FIGURE 4.14: Interfacial microstructure of the uncontaminated side (left) and the contaminated side (right) of a plate sample (RP88) reheated at 1280°C, 4% O_2, 6 hours; after descaling (SP=13.94 MPa, U=26.22l/m^2; I=1.45N/mm^2, mould flux concentration on the contaminated side is C_f=0.011g/cm^2). Backscattered electron images.

For uncontaminated samples, the scale did not contain lateral or perpendicular cracks close to the metal substrate, which would presumably render the scale difficult to remove (figure 4.14). The inner scale appeared to be adherent as a result of entanglement and occlusion of metal particles in the scale. These metal particles (tendrils) were linked to form a network. The irregular metal/inner scale interface is expected to mechanically key the scale to the steel. There was also significant grain boundary oxide penetration. Thus, descaling should remove the outer scale and not the inner scale.

4.2.4 Analysis of the Removed scale for Chromium Oxidation State

The oxidising furnace atmosphere and presence of basic components (CaO and Na_2O) in the mould flux could lead to formation of the undesirable Cr (VI) species during reheating of contaminated samples (Page and Loar, 2004). X-ray photo-electron spectroscopy was hence used to determine the oxidation state(s) of chromium in the scale.

XPS analysis was performed on both contaminated and uncontaminated samples. A mathematical curve fit procedure for the $Cr2P_{3/2}$ photoelectron peak was performed; peak positions that are associated with average binding energies of 573.94eV, 575.65eV and 577.02eV were identified. Based on comparison of these binding energies with standard spectra of various chromium species (NIST Database, 1989), it can be assumed that the lowest binding energy 573.94±0.95eV is associated with chromium (0) (metallic phase present at the interface), the binding energy 575.65±0.36 eV is associated with chromium (III) (in Cr_2O_3), and the binding energy 577.02±0.41eV is associated with chromium (III) (in spinel phases).

The presence of chromium (VI) would correspond to an average binding energy of 579.7±1.2 eV. This was not found after XPS deconvolution analysis; hence oxidation of chromium to the hexavalent state is not the origin of the differences in scale structure.

The XPS analyses (see Appendix 4) also confirmed that the amount of metallic phase in the removed scale was higher in the uncontaminated scale than in the contaminated scale (in line with the observed absence of metal tendrils in the contaminated scale).

4.3 DESCALING EXPERIMENTAL CONDITIONS AND RESULTS

Uncontaminated samples and samples contaminated with industrial mould fluxes (type 832, type 810 and type RF1) were reheated and descaled under similar conditions in order to assess the descaling effectiveness. After initial experiments, it was found that the samples were more sensitive to reheating parameters than descaling parameters (such as water flow rate, samples speed and descaling spray height). Further descaling was hence performed with different reheating parameters and constant speed and spray height. Descaling conditions were maintained close to those used in the industrial practice for the stainless steel type 304.

The experimental reheating conditions (using 3% and 4% free O_2) are shown in table 4.9.

TABLE 4.9: Reheating conditions for uncontaminated and contaminated samples which were hydraulically descaled

	% O_2	**T[°C]**	**Time [h]**	**C_f [g/cm^2]**	**Mould flux type**
D1	3	1300	5	0.023	RF1
D2	3	1300	5	0.022	832
D17	4	1280	6	0	–
D18	4	1280	6	0.011	810
D3	3	1300	5	0	–
D4	3	1300	5	0.035	RF1
D6	3	1280	5	0.015	RF1
D7	3	1280	4	0.016	810
D8	3	1280	6	0.015	832
D19	3	1280	6	0	–
D9	3	1280	5	0.021	RF1
D10	3	1250	6	0.015	RF1
D20	3	1280	6	0.015	810
D21	3	1280	6	0	–
D11	3	1250	2	0.008	RF1
D12	3	1250	6	0.011	RF1
D13	3	1250	6	0.017	832
D15	3	1280	6	0.015	810
D16	3	1280	6	0.016	832
RP22	4	1250	3	0	–
RP33	4	1250	3	0.015	832
RP44	4	1280	6	0.005	SMF3
RP55	4	1280	6	0	–
D177	3	1280	6	0	–
RP88	4	1280	6	0.011	RF1
RTS99	4	1280	5	0.017	SMF2
RTS1000	4	1280	5	0.017	SMF1

Descaling conditions are shown in table 4.10; in all cases the vertical nozzle height was 96 mm and the stock feed rate 0.8m/s.

Table 4.10**:** Descaling conditions, and visual appearance of samples after descaling. Runs of which the labels are shown in bold were for samples not coated with mould flux.

	Pr[KPa]	**Qb[l/min]**	**SP[MPa]**	**U[l/m^2]**	**I[N/mm^2]**	**Appearance**
D1	111.80	54.40	13.90	26.22	1.45	Descaled
D2	112.29	54.50	13.98	26.26	1.454	Descaled
D17	112.29	54.50	13.98	26.26	1.454	Residual scale
D18	112.29	54.50	13.98	26.26	1.454	Descaled
D3	174.95	64.07	19.83	30.87	2.036	Residual scale
D4	174.95	64.07	19.83	30.87	2.036	Descaled
D6	176.42	64.30	19.97	30.97	2.051	Descaled
D7	175.25	64.11	19.86	30.89	2.039	Descaled
D8	186.33	65.81	20.90	31.70	2.147	Descaled
D19	187.30	65.96	20.99	31.78	2.157	Residual scale
D9	171.62	63.56	19.52	30.62	2.004	Descaled
D10	174.56	64.01	19.80	30.84	2.033	Descaled
D20	111.80	54.43	13.94	26.22	1.45	Descaled
D21	111.80	54.43	13.94	26.22	1.45	Residual scale
D11	173.58	63.86	19.71	30.77	2.023	Descaled
D12	167.69	62.96	19.16	30.33	1.967	Descaled
D13	166.71	62.81	19.07	30.26	1.957	Descaled
D15	161.81	62.07	18.61	29.90	1.911	Descaled
D16	162.79	62.22	18.70	29.97	1.92	Descaled
RP22	111.80	54.43	13.94	26.22	1.45	Residual scale
RP33	111.80	54.43	13.94	26.22	1.45	Descaled
RP44	111.80	54.43	13.94	26.22	1.45	Partially descaled
RP55	111.80	54.43	13.94	26.22	1.45	Residual scale
D177	161.81	62.07	18.61	29.90	1.911	Residual scale
RP88	111.80	54.43	13.94	26.22	1.45	Descaled
RTS99	112.29	54.50	13.98	26.26	1.454	Descaled
RTS1000	111.80	54.43	13.94	26.22	1.45	Descaled

4.4 DISCUSSION OF THE DESCALING RESULTS

4.4.1 Thickness of the Residual Scale

According to the results of this investigation, austenite grain structure, the presence of Ni and Cr in the steel and mould flux contamination play major roles in the descaling behaviour of type 304 stainless steel.

The micrographs in Figure 4.15 show the difference in removed scale morphologies after descaling of the uncontaminated and contaminated samples under similar reheating and descaling conditions.

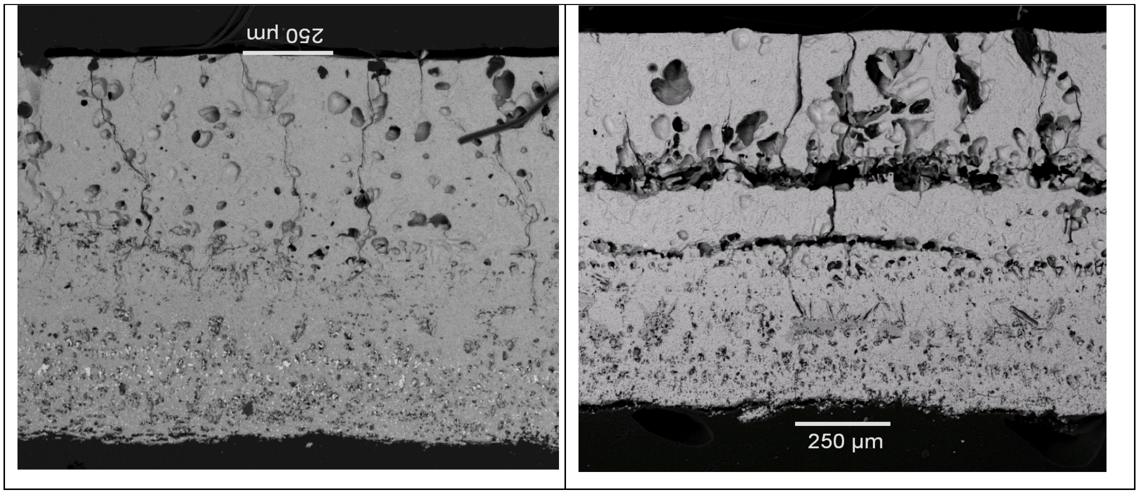

Figure 4.15: Cross-sections through scale removed from the uncontaminated sample D17 (left) and the contaminated sample RP88 (right; C_f=0.011 g/cm^2) after reheating (1280ºC, 4%O_2, 6h) and descaling (SP=13.94MPa, U=26.22/m^2, I=1.45N/mm^2). Backscattered electron images.

In the figure above the uncontaminated scale contains a layer of Ni-enriched tendrils in the inner scale (these are the bright spots in the lower part of the image), which confirms Ni enrichment at the scale-steel interface. The scale removed from the contaminated sample has no Ni-enriched metals tendrils in the inner scale. These observations are consistent with those presented in the previous sections.

Visual examination of the samples after reheating and descaling confirmed that the presence of mould fluxes promoted descaling (see Table 4.10).

4.4.2 Steel Surface after Descaling

Visual observation of the uncontaminated slab samples after descaling showed the presence of residual scale and a roughened surface. For the contaminated descaled steel, there were only a few places with residual scale, but the surfaces were mostly fully descaled. The microscopical appearance of cross-sections confirmed this (Figures 4.16 and 4.17), showing the adherent residual scale on the surface of the uncontaminated sample and the non-adherent residual scale on the surface of the contaminated sample. From measurements on cross-sections, the thickness of the residual scale on the uncontaminated steel was 440-550µm.

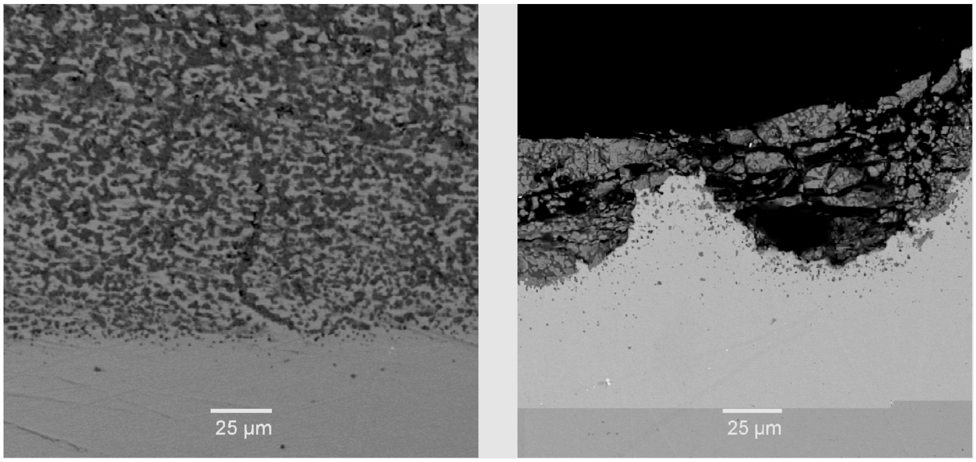

FIGURE 4.16: Difference in scale morphology of the residual scale after reheating and descaling of the uncontaminated (left) and contaminated (right); samples D16 and D177. Reheating and descaling conditions: 1280°C, 3% O_2, $C_f = 0.016$ g/cm^2 (on the contaminated sample), 6 h, SP = 18.61 MPa, U = 29.9 l/m^2, I = 1.91 N/mm^2. Backscattered electron images.

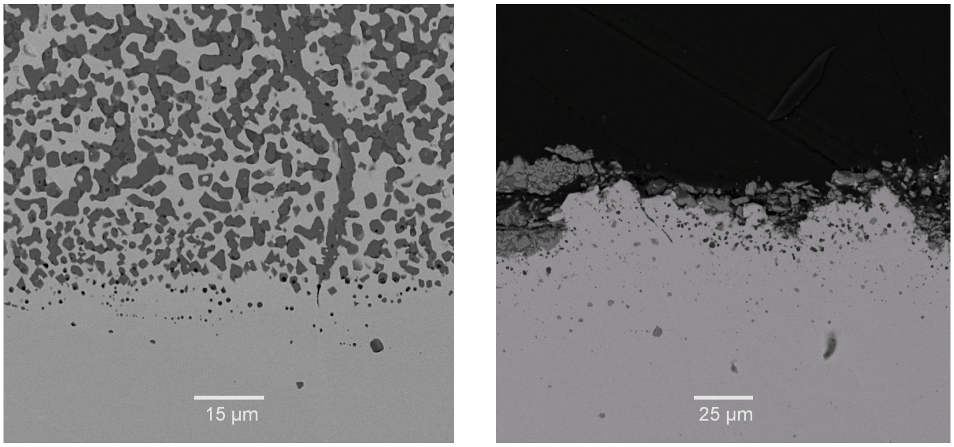

FIGURE 4.17: Residual scale on uncontaminated (left) and contaminated (right) plate surfaces of samples D19 and D8. Reheating and descaling conditions: 1280°C, 3% O_2, 6 h, $C_f = 0.015$ g/cm^2 (on the contaminated sample), I = 2.15 N/mm^2, U = 31.7 l/m^2. Backscattered electron images.

For contaminated samples, changes in temperature, time and the excess free oxygen (within the ranges studied) were found to have little effect on the oxidation rate and the descaling effectiveness, because descaling was always effective.

For uncontaminated samples, increases in temperature and longer reheating times were found to increase the extent of oxidation slightly, with poorer surface quality after descaling. A difference in the free oxygen content (3% and 4%) of the gas during reheating was found not to have major impact on the extent of oxidation.

The micrographs in figure 4.18 show the difference in the external appearance of the descaled surface for uncontaminated and contaminated samples (note that these are not cross-sections). The bright areas in the residual scale on the surface of the uncontaminated slab are Ni-enriched metal tendrils. These tendrils appear also in the inner part of the removed scale on the uncontaminated slab (see figure 4.15)

The bright areas on the contaminated slab surface are the chromium oxide layer (inner scale); EDX analysis gave a composition of 91.1% Cr; 6.2% Fe; 1.1% Si.

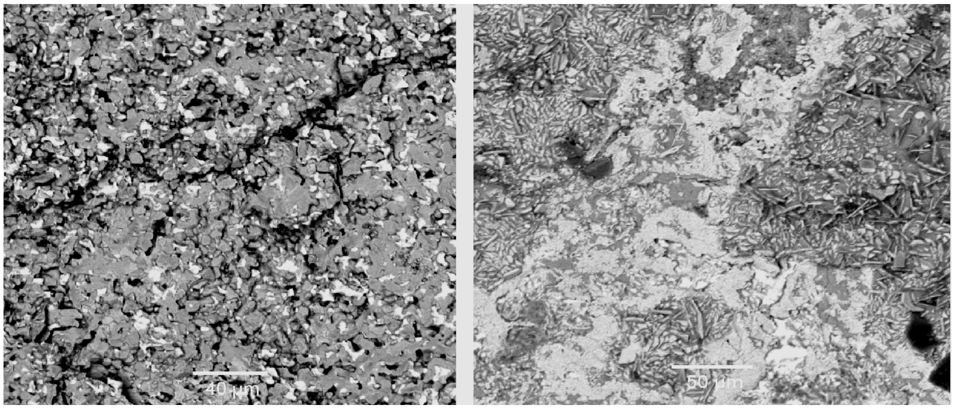

FIGURE 4.18: Difference in exterior appearance of descaled uncontaminated (left) and contaminated (right; $C_f = 0.011$ g/cm^2) slab samples D17 and D18; BSE images. Reheating and descaling conditions: 6 h, 4% O_2, 1280°C, SP = 13.98 MPa, U = 26.26 l/m^2, I = 1.45N/mm^2.

4.4.3 Effect of Descaling Variables

Descaling water system pressure, and hence impingement water flow rate, were varied in the first stage of this investigation and subsequently kept constant for the major part of the investigation, both to simulate industrial descaling conditions and also because it was found that descaling mainly depended on the reheating conditions rather than descaling conditions.

4.4.4 Mould Flux Effects on Descaling

In these experiments, the applied decarburised mould flux surface concentration varied between 0.005g/cm^2 and 0.035 g/cm^2, corresponding to average molten flux thicknesses of 19 µm to 135 µm on the steel surface. All mould flux surface concentrations explored during this project were found to give better descaling results, but the best results were found for mould flux surface concentration around 0.016 g/cm^2 or 60 µm of molten film on slab surface. Beyond 0.03 g/cm^2 or 115 µm, the slab surface was found to contain some black spots after descaling, possibly an excess of the unreacted mould flux on the steel surface. It should be noticed, in these experiments, below 0.008g/cm^2 (30 µm) of mould flux surface concentration it was difficult to obtain an even distribution of flux over the sample surface.

While all mould fluxes were found to give better descaling and steel surface quality, type 832 was found to be the best according to the descaled slab surface quality, followed by type RF1; descaled surface quality was assessed by visual examination of the samples, and SEM observation of both the metal-residual scale interface (cross-sectioned samples) and the exterior surface of the descaled samples.

4.5 PROPOSED MECHANISM BEHIND NICKEL OXIDATION

The direct cause of the much improved descaling for samples contaminated with mould flux is the disappearance of Ni-enriched metal tendrils. Clearly, the presence of mould flux promotes oxidation of nickel, and so avoids tendril formation. This effect does not depend on the details of the mould flux composition – the effect was found for industrial and synthetic mould fluxes, with and without CaF_2 and Na_2O. The underlying effect appears to be that NiO can dissolve in the mould flux, and that this favours nickel oxidation. There are limited data on this, but Lee *et al.* (2002) have summarised available data on the nickel oxide capacity of CaO-SiO_2-FeO slags. They propose that NiO dissolves in the slag through the oxidation reaction

$$Ni + 0.5\,O_2 + O^{2--} = NiO_2^{2-}$$

In this expression, O^{2-} anions provided by the slag (mould flux) react with the nickel oxidation products to form nickel oxide anions (NiO_2^{2-}) which dissolve in the mould flux; the presence of iron oxide in the flux (which develops during scale growth) also enhances dissolution of nickel oxide (Lee *et al.*, 2002).

According to this mechanism, the beneficial effect of the mould flux would depend on its basicity (although the effect is not particularly strong – the nickel oxide capacity of C_2S-saturated slag is only 3 times that of lower-basicity slag with $X_{\mathrm{CaO}}/X_{\mathrm{SiO_2}} = 0.5$ to 0.7 [ibid.]).

Chapter 5: CONCLUSIONS AND RECOMMENDATIONS

Mould flux residues strongly change the nature of the inner scale (due to enhanced oxidation of nickel). The change in the nature of the scale-steel interface was found to enhance the descaling of the contaminated slabs.

For all contaminated samples, visual descaling effectiveness was approximately 100%.

For uncontaminated samples, visual descaling effectiveness was at best approximately 40% at 1300°C; 3% free O_2; 5 h reheating; I=2N/mm^2.

Mould flux type 832 (low CaO/SiO_2 ratio, but high Na_2O and CaF_2 content) was found to give the best descaling effectiveness and steel surface quality amongst the three industrial mould fluxes used for this investigation. Of the three synthetic mould fluxes used, it was found that mould flux SMF2 (20% CaF_2,40% CaO and 40% SiO_2) gave better descaling and better slab surface quality, similar to that obtained with mould flux type 832.

The remnant scale on the reheated samples after cooling of the contaminated sample in nitrogen box was very thin and the scale did not cover the entire surface.

For the contaminated samples it was found that descaling efficiency mostly depended on the reheating parameters (especially the presence mould flux on the steel surface) rather than the descaling parameters. For surfaces dosed with mould flux, it appears that the impact pressure could be reduced in industry without compromising descaling efficiency.

These results suggest future work on the effect of mould flux on scale adhesion to reheated slabs of other grades of stainless-steels and especially for nickel-bearing stainless steels. For example, dosing mould flux onto surfaces covered with nickel-enriched metal tendrils should destroy these tendrils; it would be interesting to test this possibility, and whether basicity does have the expected effect. The flux melting point would also be of important: binary CaO-SiO_2 mixtures are not molten at reheating temperatures, but the presence of FeO (and even Fe_2O_3) decreases the melting point considerably.

REFERENCES

Abuluwefa H.T., Guthrie R.I.L., and Muccardi F., 1992, *Scale formation in a walking-beam furnace*, 34th Mech. Working and Steel Processing Conf. Proc., Quebec, Canada, 25-28 Oct. 1992, pp. 453-468.

Abuluwefa H.T., Guthrie R.I.L., and Ajersch F., 1997, *Oxidation of low-carbon steel in multi-component gases: Part 1. Reaction mechanisms during isothermal oxidation*, Metallurgical and Materials Transactions A, vol. 28A, pp. 1633-1641.

Ajersch F., 1992, *Scale formation in steel processing operations*, 34th Mech. Working and Steel Processing Conf. Proc., Quebec, Canada, 25-28 Oct. 1992, pp. 419-437.

Akiyama T., Otha H., Takahashi R., Waseda Y., and Yagi J., 1992, *Measurement and modelling of thermal conductivity for dense iron oxide and porous iron ore agglomerates in step reduction*, ISIJ International, vol. 32, pp. 829-837

Asai T., Soshiroda T., and Miyahara M., 1997, *Influence of Ni impurity in steel on the removability of primary scale in hydraulic descaling*, ISIJ International, vol. 37, pp. 272-277.

Birks N., and Meier G.H., 1983, *Introduction to oxidation of metals*. Edward-Arnold, London.

Page B.J., and Loar G.W., 2004, *Chromium compounds*, Kirk-Othmer Encyclopedia of Chemical Technology, vol. 6, pp. 526-571. John Wiley & Sons.

Blazevic D.T., 1987, *Rolled in scale- the consistent problem*, 4th International Steel rolling conference, June 1987, Vol. 1, pp. A38.1-13.

Bockel-Macal S. and Zamuner B., 2002, *Decarburization and iron oxide formation minimization in steel reheating furnaces*, 44th Mech. Working and Steel Processing Conf. Proc., Orlando, FL, USA, 8-11 Sept. 2002. pp. 1045-1056.

Boulton G., Davies R.G., Edwards W.J., Steigler P., and Wallace G.A., 2004, *Auditing rolling mills performance*, SEAISI Quarterly 2004, vol. 33, no.1, pp. 47-58.

Branion R.V., 1986, *Mold fluxes for continuous casting*, Iron & Steelmaker, vol. 13, no. 9, pp. 41-50.

Budinski K.G., Budinski M.K., 1999, *Engineering materials - properties and selection*, 6th edition. Prentice Hall. pp. 266-267

Chen R.Y., Yuen W.Y.D., and Mak T., 2001, *Oxide scale growth and its pickling characteristics of hot-rolled steel strip*, 43rd Mech. Working and Steel Processing Conf. Proc., Charlotte, NC, USA, 28-31 Oct. 2001, pp. 287-299.

Dénes E. and Kovács M., 2003, *A comprehensive study of oxide layers formed during the elaboration of low alloy and electrotechnical steel sheets*, Materials Science Forum, vol. 414-415, pp. 175-182.

D'Haeyer R., 1987, *Development of new mould powders for continuous casting*, Technical steel research, Commission of the European Communities, Report EUR 10326 EN, Liege, Belgium.

FACT thermo-chemical database, http://www.crct.polymtl.ca/fact.htm

Frick J., 2003, *Optimization of nozzle arrangements on descaling headers*, 4th International Conference on Hydraulic Descaling, London UK.

Frick J.W., 2004, *More efficient hydraulic descaling header designs*, Metallurgical plant and Technology International, vol. 27, no. 2, pp. 90-92.

Fujii C.T. and Meussner R.A., 1964, *Mechanism of high temperature oxidation of iron-chromium alloys in water vapour*, Journal of Electrochemical Society, vol. 111, pp. 1215-1221.

Fukagawa T., Okada H., and Fujikawa H., 1997, *Effect of P on hydraulic-descaling-ability in Si-added hot-rolled Steel sheets,* Journal of the Japanese Association: Tetsu-to-Hagane, vol. 83, no.5, pp.305-310.

Fukutsuka T., Nakamura T., Sato M., Kokubo I. and Ishida R., 1981, *Study of descaling of steel slabs before hot rolling*, Transactions of the Iron and Steel Institute of Japan, vol. 21, pp. 699-707.

Garber S., 1959, *Fundamental aspects of scale on mild-steel strip*, Journal of the Iron and Steel Institute, vol. 192, pp.153-160.

Grigg C.R., Sexton B.G., and Matteson L.E., 1987, *1420mm Hot Strip Mill Control of Rolled-in-Scale,* 4th International Steel rolling conference, pp. A39.1-8.

Hänsel M., Boddington C.A., and Young D.J., 2003, *Internal oxidation and carburisation of heat-resistant alloys*, Corrosion Science, vol .45, pp.967-981.

Hirth J.P., Pieraggi B., and Rapp R.A., 1995, *The role of interface dislocations and ledges as sources/sinks for point defects in scaling reactions.* Acta Metallurgica et Materialia, vol. 43, pp. 1065-1073.

Jentoftsen T.E., Lorentsen O-A., Dewing E.W., Haarberg G.M., and Thonstad J., 2002, *Solubility of some transition metal oxides in cryolite-alumina melts: Part I. Solubility of FeO, $FeAl_2O_4$, NiO and $NiAl_2O_4$*, Metallurgical and Materials Transactions B, vol. 33B, pp. 901-908.

Jiang M., Zhu C., and Han W., 2004, *Surface roughness of flux film in continuous casting mold*, Journal of Iron and Steel Research International, vol. 11(6), pp. 10-13.

Kemprocast mould powders, http://www.kempro.com/mould.htm, visited 06 April 2007.

Kizu T., Nagataki Y., Inazumi T., and Hosoya Y., 2001, *Effects of chemical composition and oxidation temperature on the adhesion of scale in plain carbon steels*, ISIJ International, vol. 41, pp. 1494-1501.

Kizu T., Nagataki Y., Inazami T., and Hosoya Y., 2002, *Intergranular and internal oxidation during hot-rolling process in ultra-low carbon steel*, ISIJ International, vol. 42, pp. 206-214.

Kofstad P., 1966, *High temperature oxidation of metals*. Wiley, New York.

Kofstad P., 1988, *High temperature Corrosion*, pp.109, 396. Elsevier, London.

Kubashewski O. and Hopkins B.E., 1962, *Oxidation of metals and alloys*, Second edition. Butterworths, London.

Levin E.M., Robbins C.R., and McMurdie H.F., 1964, *Phase Diagrams for Ceramists*. American Ceramic Society, Columbus, Ohio.

Lee S.H., Moon S.M., Park J.H., and Min D.J., 2002, *Thermodynamic behavior of nickel in $CaO\text{-}SiO_2\text{-}Fe_tO$ slag*, Metallurgical and Materials Transactions B, vol. 33B, pp. 55-59.

Lee VHJ., Gleeson B., and Young DJ., 2005, *Scaling of carbon steel in simulated reheat furnace atmospheres*, Oxidation of Metals, vol. 63, pp. 15-31.

Li L-F., Jiang Z-H., and Riquier Y., 2005, *High-temperature oxidation of duplex stainless steels in air and mixed gas of air and CH_4*, Corrosion Science, vol. 47, pp. 57-68.

Ludlow V., Harris B., Riaz S., and Normanton A., 2004, *Continuous casting mould powder and casting process interaction: why powders do not always work as expected*. VII International Conference on Molten Slags Fluxes and Salts, Cape Town, January 2004. pp. 723-730.

Luthra K.L., and Briant C.L., 1989, *The role surface segregation and stresses in scale adherence*, Material Science Forum, vol. 43, pp. 299-326.

Ma G., 2005, *Cr (VI)-containing electric furnace dust and filter cake: characteristics, formation, leachability and stabilisation*. PhD Thesis, University of Pretoria. Available at http://upetd.up.ac.za/thesis/available/etd-10182006-163226/

Matsuno F., 1980, *Blistering and hydraulic removal of scale films of rimmed steel at high temperature*, Transactions of the Iron and Steel Institute of Japan, vol. 20, pp. 413-421.

Mills, K.C., 1998, *Mould fluxes for continuous casting and their effect on product quality*, Alex McLean Symposium Proceedings, Toronto, Ontario, Canada, July 12-14, 1998, pp. 195-204.

Mills, K.C., Fox A.B., 2003, *The role of mould fluxes in continuous casting – so simple yet so complex,* ISIJ International, vol. 43 no. 10, pp. 1479-1486.

Mills K.C., Fox A.B., Li Z., and Thackray R.P., 2005, *Performance and properties of mould fluxes*, Ironmaking and Steelmaking, vol. 32, pp. 26-34.

Moon D.P., and Bennett M.J., 1989, *The effects of reactive element oxide coating on the oxidation behaviour of metal and alloys at high temperatures*, Materials Science Forum, vol. 43, pp. 269-298.

Morris P., Bagshaw P., and Marston H., 1996, *Descaling of steels in rolling mills*, Report EUR 15836, ECSC agreement no.7210EA/818, European commission, Technical Steel Research, Office for Official Publications of the European Communities, Luxembourg.

Nagai H., 1989, *Effect of rare earth metals and oxides addition on the high temperature oxidation of Ni-Cr and Fe-Cr alloys*, Materials Science Forum, vol. 43, pp. 75-130.

Neumann F., Neal J., Pedroza M.A., Castillejos A.H., Acosta F.A., 1996, *Mold fluxes in high speed thin slab casting*, Proc. 79th Steelmaking Conf., Pittsburgh, PA, 24-27 Mar. 1996, pp. 249-257.

NIST X-ray Photoelectron Spectroscopy Database version 2.0, US Secretary of Commerce, 1989.

Ogibayashi S., Mukai T., Mimura Y., Nagano Y., Yamaguchi K, Takahashi T., Koyama K. and Nakano T., 1987, *Mold powder technology for continuous casting of low-carbon aluminum-killed steel*, Nippon Steel Technical Report, no. 34 (July 1987), pp. 1-10.

Persson M., 2007, *Investigations of slag properties and reactions*, Doctoral Thesis, Royal Institute of Technology, Sweden.

Pickens J.W., 1984, *The micro-structural characteristics of oxide scale formed during bar processing*, 25th Mech. Working and Steel Processing Conf. Proc., pp. 39-65.

Pieraggi B., and Rapp R.A., 1988, *Stress generation and vacancy annihilation during scale growth limited by cation-vacancy diffusion*, Acta Metallurgica, vol. 36, pp. 1281-1289.

Pistorius P.C., Quagraine N.-A., and Coetzee C., 2003, *Descaling of stainless steel following simulated reheating*, Journal of the South African Institute of Mining and Metallurgy, vol. 103, pp. 607-615.

Rajil S., Fox A.B., Mills K.C., Lee P.D., and Deo B., 2004, *The factors affecting powder consumption of mould fluxes*, Scandinavian Journal of Metallurgy, vol. 33, pp. 85-91.

Rapp R.A., 1984, *The high temperature oxidation of metals forming cation diffusing scales*, Metallurgical Transactions A, vol. 15A, pp. 765-782.

Riquier Y., and Dumortier C., 1997, *Influence of reheating on surface structure and composition of austenitic stainless steel products*, Matériaux et techniques, vol. 85, no. 11-12, pp. 15-22.

Sachs K., and Tuck C.W., 1968, *Surface oxidation of steel in industrial furnaces*, Proceedings of the Conference of Iron and Steel Institute on Reheating for Hot Working, Iron and Steel Institute, London, pp. 1-17.

Sachs K., and Tuck C.W., 1970, *Scale growth during reheating cycles*, Werkstoffe und Korrosion, vol. 21, pp. 945-954.

Sano N., Lu W-K., Riboud P V., and Maeda M. (eds.), 1997, *Advanced physical chemistry for Process Metallurgy*, Academic Press, London, pp. 71-74.

Schwerdtfeger K.L., 2003, *Heat withdrawal in continuous casting of steel,* A Cramb (ed.), The Making, Shaping and Treating of Steel, 11th ed., Casting Volume. The AISE Steel Foundation, 2003:1-41.

Shin H.J., Lee G.G., Kang S.M., Kim S.H., Choi W.Y., Park J.H., Thomas B.G., 2005, *Effect of mold oscillation on powder consumption and hook formation in ultralow-carbon steel slabs*", Iron and Steel Technology, vol. 2, no. 9, pp. 56-69.

Sheasby J.S., Boggs W.E., and Turdogan E.T., 1984, *Scale growth on steels at 1200°C: rationale of rate and morphology*, Metal Science, vol. 18, pp. 127-136.

Sheppard T., and Steen W.M., 1970, *Hydraulic descaling of steel: A preliminary experimental survey*, Journal of the Iron and Steel Institute, vol. 208, pp. 797-805.

Sheridan A.T., and Simon P., 1995, *Descaling of steel in rolling mills*, European Steelmaking Developments and Perspectives in Rolling and Reheating, Commission of the European Communities, Luxembourg, pp.233-244.

Sherwood W., and Shatynski S.R., 1984, *The effect of temperature on oxide scale adherence during descaling operations*, vol. 21, no. 1, pp. 39-51.

Schürmann S., 2000, *Measurement and mathematical approximation of the impact of descaling nozzles*, 3rd International Conference on Hydraulic Descaling, London, 14-15 September 2000.

Taniguchi S., 1985, *Stresses developed during the oxidation of metals and alloys*, Transactions of the Iron and Steel Institute of Japan, vol. 25, pp. 3-13.

Tuck C.W., and Barlow J., 1972, *the effect of reheating furnace atmosphere on the adhesion of scale to steel*, Iron and Steel, vol. 45, no. 1, pp. 31-38.

Tuck C.W., Odgers M., and Sachs K., 1969, *The oxidation of iron at 950°C in oxygen/water vapour mixtures*, Corrosion Science, vol. 9, pp. 271-285.

Turkdogan E.T., 1996, *Fundamentals of steelmaking*. Institute of Materials, London. pp. 138-179.

Whittle D.P., and Wood G. C., 1967, *Complex scale formation on iron-18 percent chromium alloy*, Journal of the Electrochemical Society, vol. 114, pp. 986-993.

Zitterman J.A., Bacco R.P., and Boggs W.E., 1982, *Factors affecting scale adhesion on steel forgings*, Journal of Metals, vol. 34, no. 4, pp. 22-26.

APPENDICES

APPENDIX 1

GAS FLOW RATES FOR SIMULATED REHEATING ATMOSPHERE

In this section, the required gas flow rates in the reheating furnace was calculated with 3% and 4% excess oxygen to ensure complete combustion of methane in air. Calculations based on the combustion of methane are presented below.

Reaction: $CH_4 + 2O_2 = CO_2 + 2H_2O$

Input: CH_4, Air (21%O_2, 79% N_2)

Output: CO_2, O_2, H_2O, N_2

Basis: 100g of CH_4

Table 1A and 1B below give the results of the mass balance calculation for respectively 4% and 3% O_2 in the off gas.

TABLE 1A: Methane combustion with oxygen excess in the off gas of 4%

INPUT	**CH_4**	**Stoich. O_2**	**Stoich. N_2**	**Stoich. Air**	**Excess air**	**Total Air**
n (mol)	6.25	12.5				
V (Ndm^3)		280	1053.33	1333.33	346.67	1680.00
OUTPUT	**CO_2**	**O_2**	**N_2**	**H_2O**	**Off gas**	**Total gas**
Mol (mol)	6.25			12.5		
V (Ndm^3)	140		1327.20	280	1473.33	1820
% offgas	7.70	4	72.92	15.39		100
% dry offgas	9.09	4.73	86.18	0		100

TABLE 2A: Methane combustion with oxygen excess in the off gas of 3%

INPUT	**CH_4**	**Stoich. O_2**	**Stoich. N_2**	**Stoich. Air**	**Excess air**	**Total Air**
n (mol)	6.25	12.5				
V (Ndm^3)		280	1053.33	1333.33	245.56	1578.89
OUTPUT	**CO_2**	**O_2**	**N_2**	**H_2O**	**Off gas**	**Total gas**
n (mol)	6.25			12.5		
V (Ndm^3)	140		1247.32	280	1473.33	1718.89
% offgas	8.1	3	72.60	16.30		100
% dry offgas	9.73	3.58	86.67	0		100

Based on these values, the total volume of gas fed to the furnace is calculated as follows:

Dimension of tube: OD = 9cm, ID =7.6cm, Length = 150cm; speed of gas in the tube 0.1 m/s (1250°C, 1 atmosphere)

V_t, total volume of gas = area × speed

$V_{tot} = 8.13\times10^{-5}$ Nm^3/s.

For oxygen excess of respectively 4% and 3%, the flow rates of the individual gases to the furnace should be:

TABLE 3A: Gas flow rates with 4% and 3% oxygen excess in the offgas

4% O_2 Excess	**Nm^3/s**	**dm^3/min**
V_{N2}	5.9×10^{-5}	3.6
V_{CO2}	6.3×10^{-6}	0.38
V_{O2}	3.3×10^{-6}	0.20

3% O_2 Excess	**Nm^3/s**	**dm^3/min**
V_{N2}	5.9×10^{-5}	3.6
V_{CO2}	6.6×10^{-6}	0.38
V_{O2}	2.4×10^{-6}	0.15

The following tables show the rotameter calibrations, as determined using a bubble tower:

CO_2 calibration

Pressure drop [mmHg]	Rotameter setting. [ml/min]	Bubble Meter [ml]	Average Time [second]	Measured rate [l/min]
51	50	50	43.584	0.06883
53	100	50	20.53	0.14613
60	200	50	10.0148	0.29956
66.5	400	50	5.4775	0.5477
73	600	50	3.655	0.82079

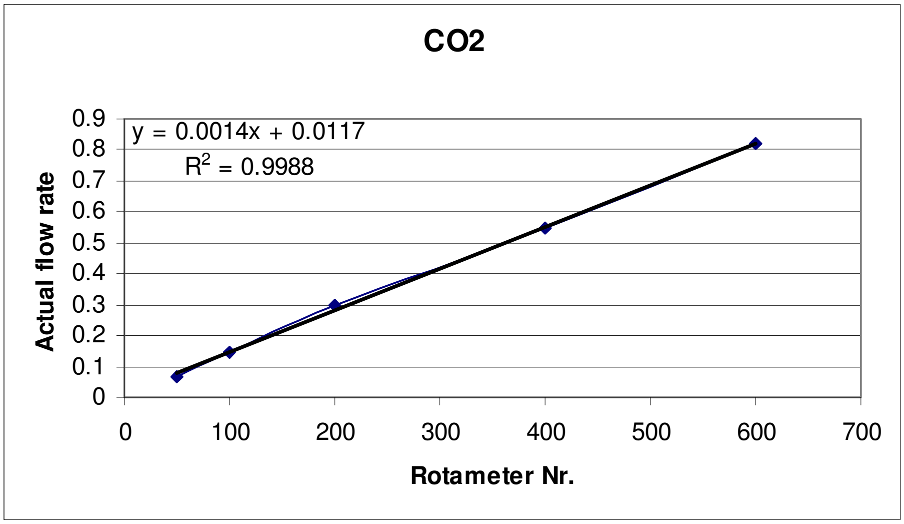

O_2 calibration

Pressure drop [mmHg]	Rotameter Nr. [ml/min]	Bubble meter [ml]	Average time [second]	Measured rate [l/min]
53	20	50	75.332	0.03982
55	50	50	53.2433	0.05635
57	100	50	25.6925	0.11677
60	150	50	17.1567	0.17486
61	200	50	12.8125	0.23415

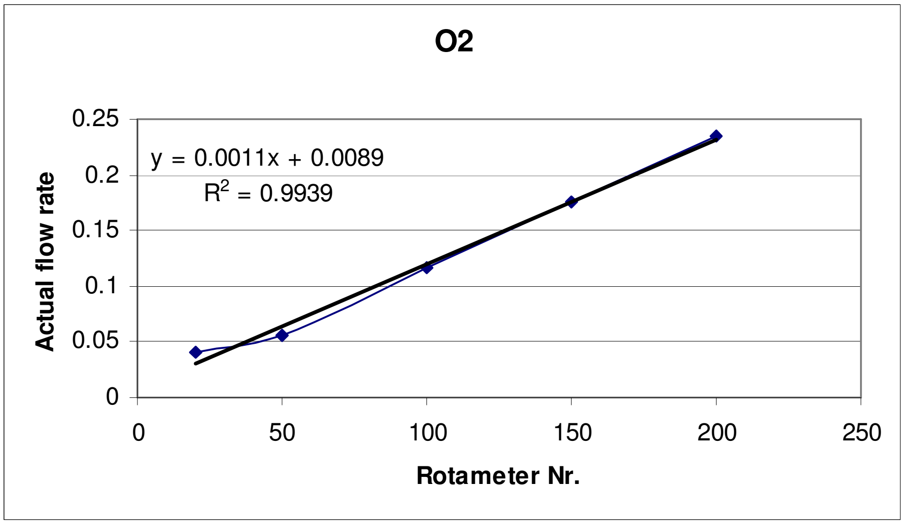

N_2 calibration

Pressure drop [mmHg]	Rotameter Nr. [l/min]	bubble meter [ml]	Average time [second]	Measured rate [l/min]
57	0.8	300	12.202	1.47517
60	1	300	10.023	1.79587
70	2	300	6.21	2.89855
78	3	300	4.14	4.34783
87	4	300	3.065	5.87276
94	5	300	2.185	8.23799

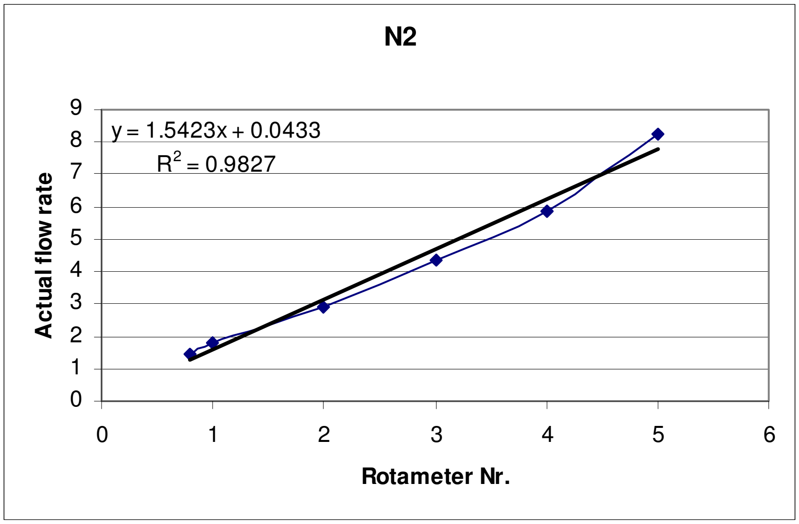
N2
y = 1.5423x + 0.0433
R² = 0.9827
Actual flow rate
0
1
2
3
4
5
6
7
8
9
Rotameter Nr.
0
1
2
3
4
5
6

APPENDIX 2

WATER CONTENT OF THE GAS MIXTURE

Preliminary high temperature reheating experiments were carried out by passing the exit gas (at the bottom of furnace) through a pre-weighed drierite column in order to check that the correct amount of vapour entered the furnace. The gas composition was chosen to obtain 3% O_2 excess in the furnace off-gas. The column was weighed again after the experiments were completed. The amount of water that was absorbed by the drierite column was given by the difference in the two masses.

Mass of drierite	257.01g0g
Mass of drierite + water	276.89g
Mass of water	19.88g

In this experiment, the value of 19.88g was compared with the calculated value of the mass of water that was expected in the gas mixture at the laboratory temperature and pressure.

From the ideal gas law (pV = nRT), for an ambient pressure of 0.86 atm and temperature of 298 K, the number of moles of the dry gas mixture was calculated as follows:

Total dry gas flow rate (l/min)	**Time (min)**	**Total dry gas volume (l)**	**Moles of dry gas**
5	30	150	5.3

Based on the expected percentage of water in the gas mixture of 16.3% (based on the condenser temperature) the expected amount of water is then calculated as follows:

[5.3/(1-16.3/100)] × (16.3/100) = 1.03 moles

The expected mass of water calculated from the gas mixture is then:

1.03 × 18 = 18.54g

APPENDIX 3

XRD spectra of the scales

After reheating before hydraulic descaling, oxides scale were removed from contaminated and the uncontaminated samples for phase identification by means of X-ray diffraction analysis. The removed scale was pulverised before X-ray diffraction. The residual scale which remained on the sample surface after removing the outer scale was also analysed. Some pieces of removed scale were not pulverised, to allow the inner surfaces (closer to the steel) of the removed scale to be examined by X-ray diffraction.

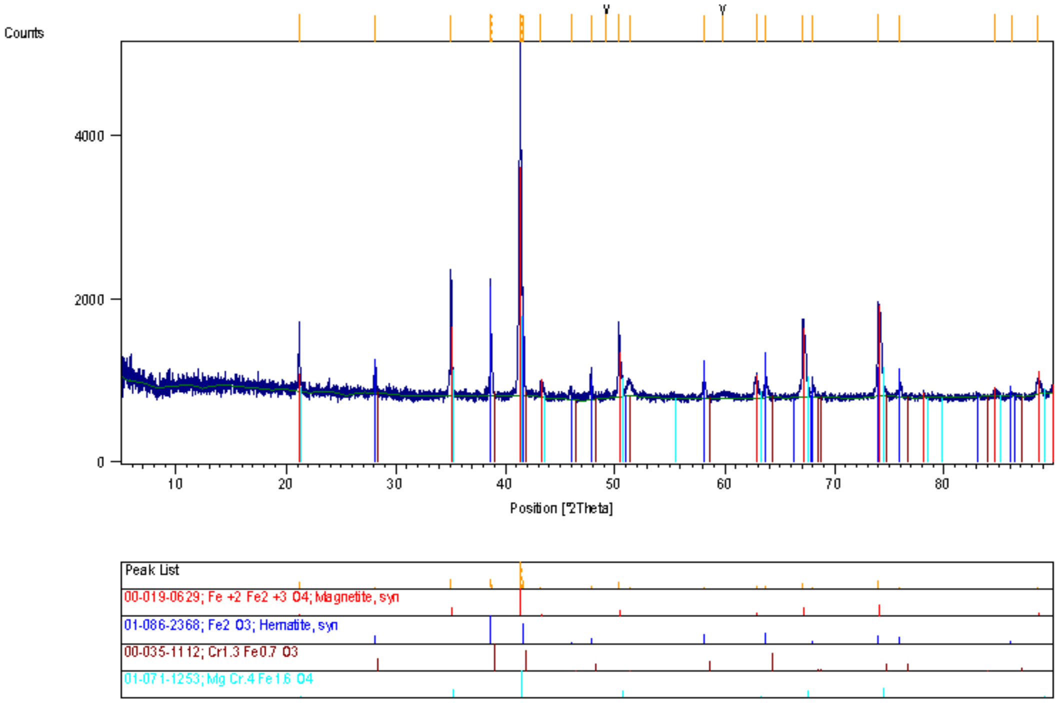

XRD pattern: scale removed from uncontaminated sample RP2. Main phases are magnetite, hematite, and Cr_2O_3.

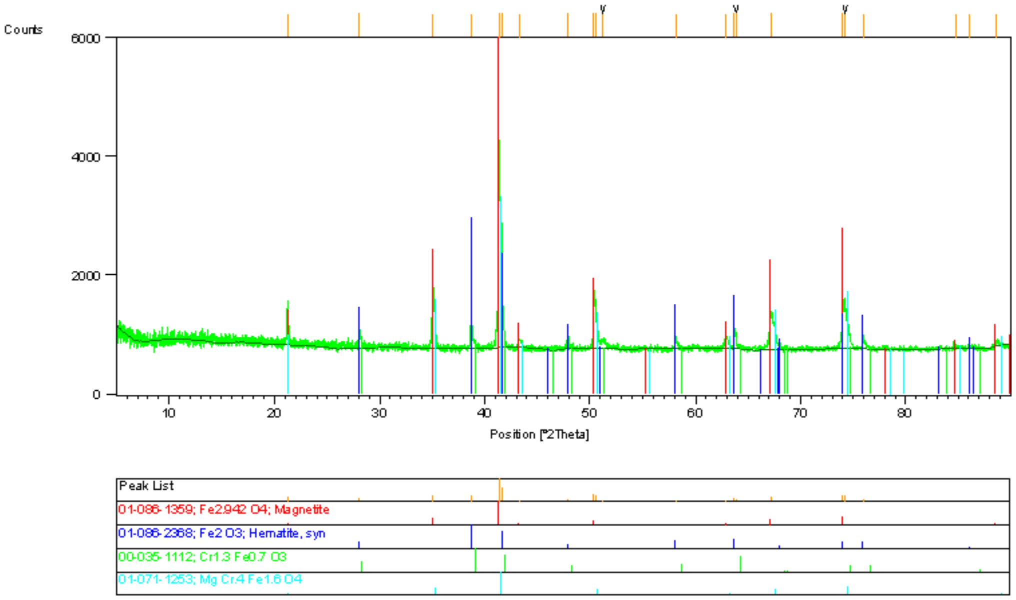

XRD pattern: scale removed from contaminated sample RP3. Main phases are spinel ("magnetite"), hematite and Cr_2O_3

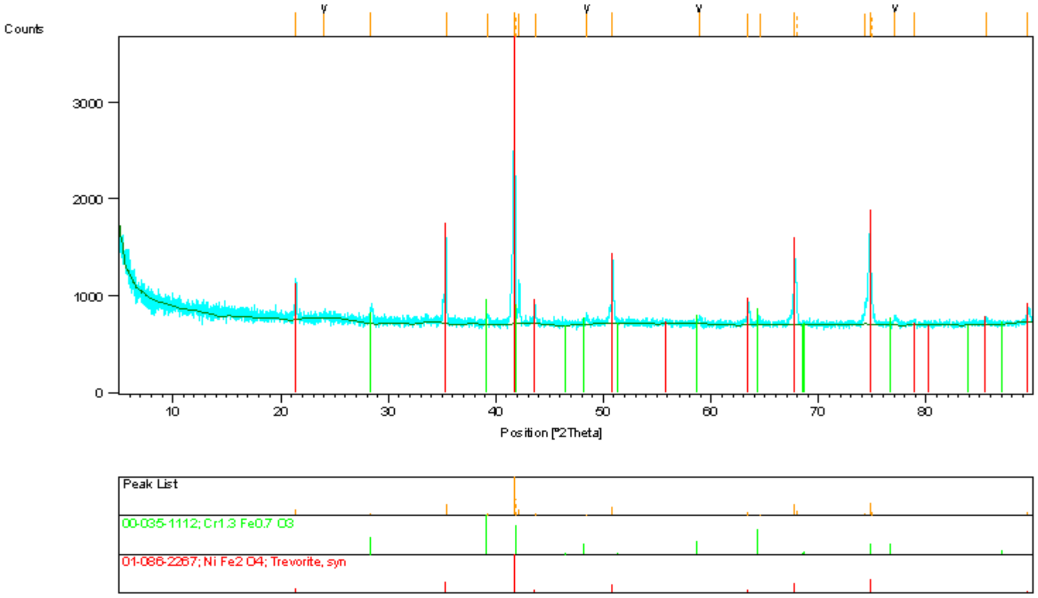

XRD pattern: inner surface of scale removed from contaminated sample D2. Main phases are Cr_2O_3 and spinel (here labelled "trevorite").

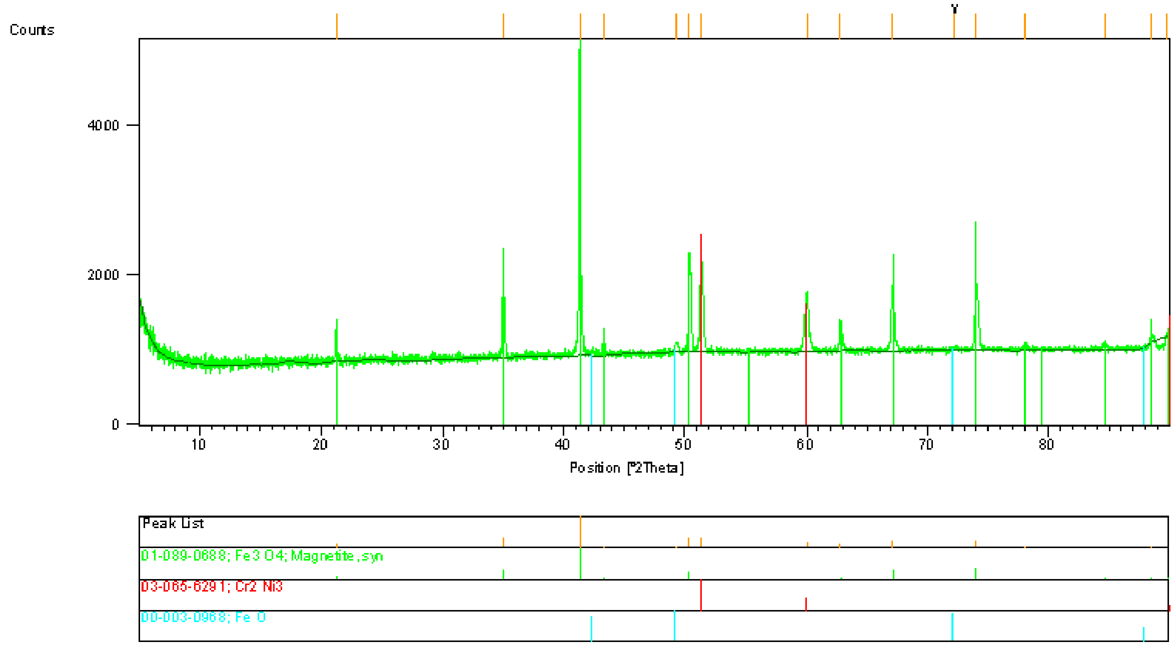

XRD pattern: inner surface of scale removed from the uncontaminated sample D1. Main phases are spinel (magnetite) and austenite (here labelled "Cr_2Ni_3")

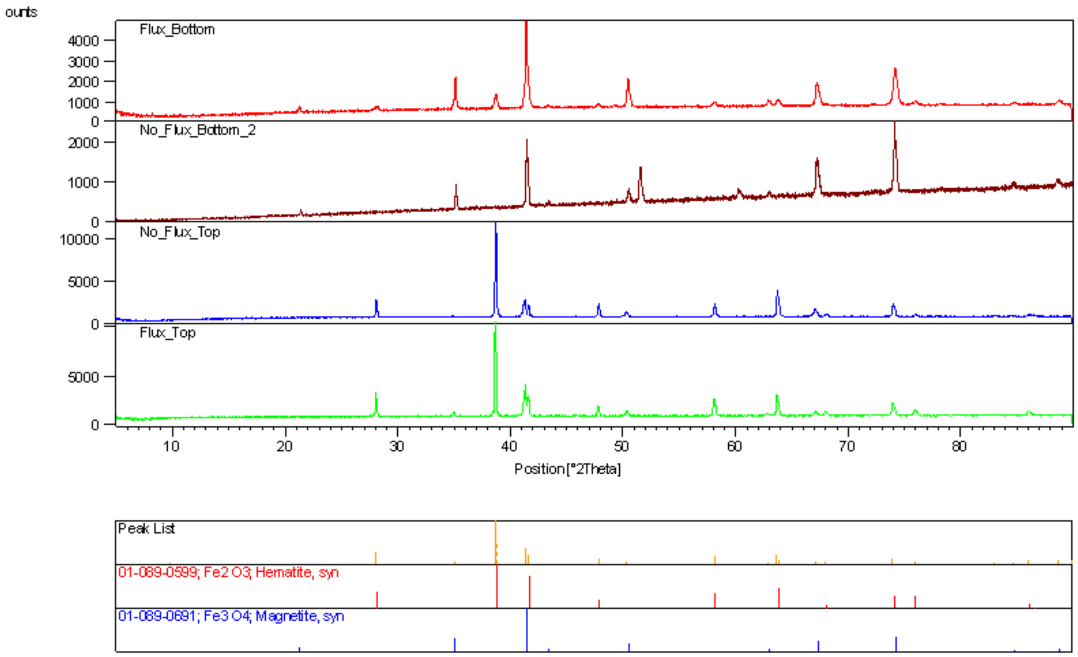

Comparison of XRD patterns of scales removed from contaminated samples (bottom and top side) and uncontaminated samples (bottom and top side)

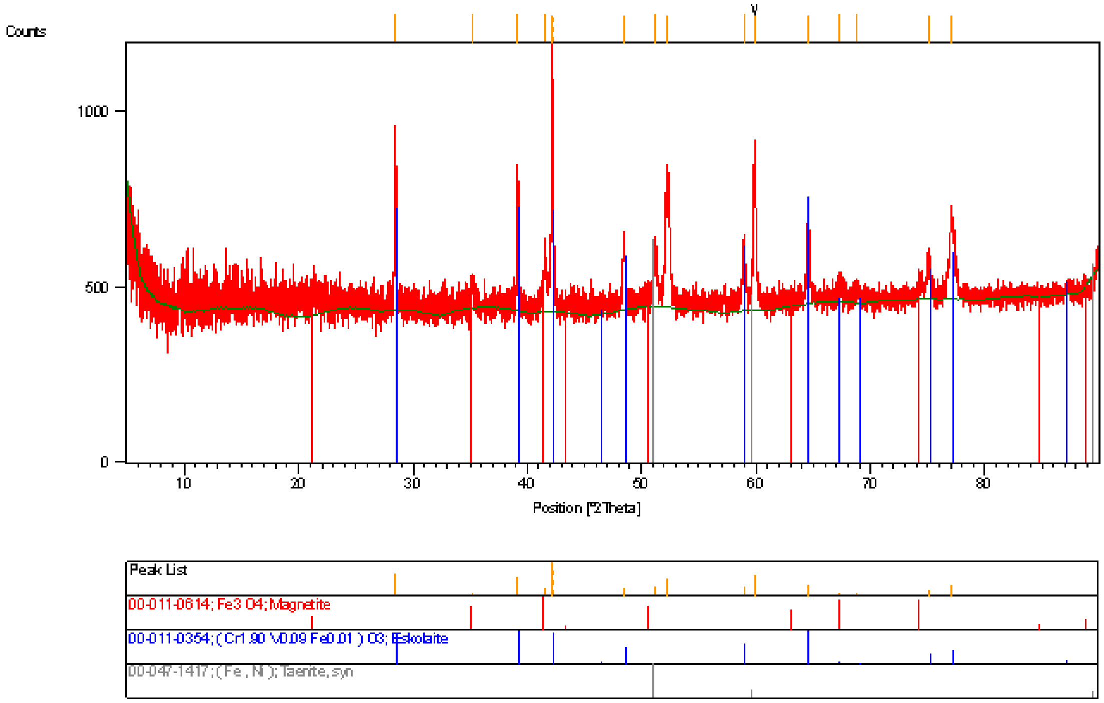

XRD pattern: residual scale after descaling top side of the contaminated sample D1. Main phases are spinel ("magnetite"), Cr_2O_3 ("eskoilite") and austenite ("taenite")

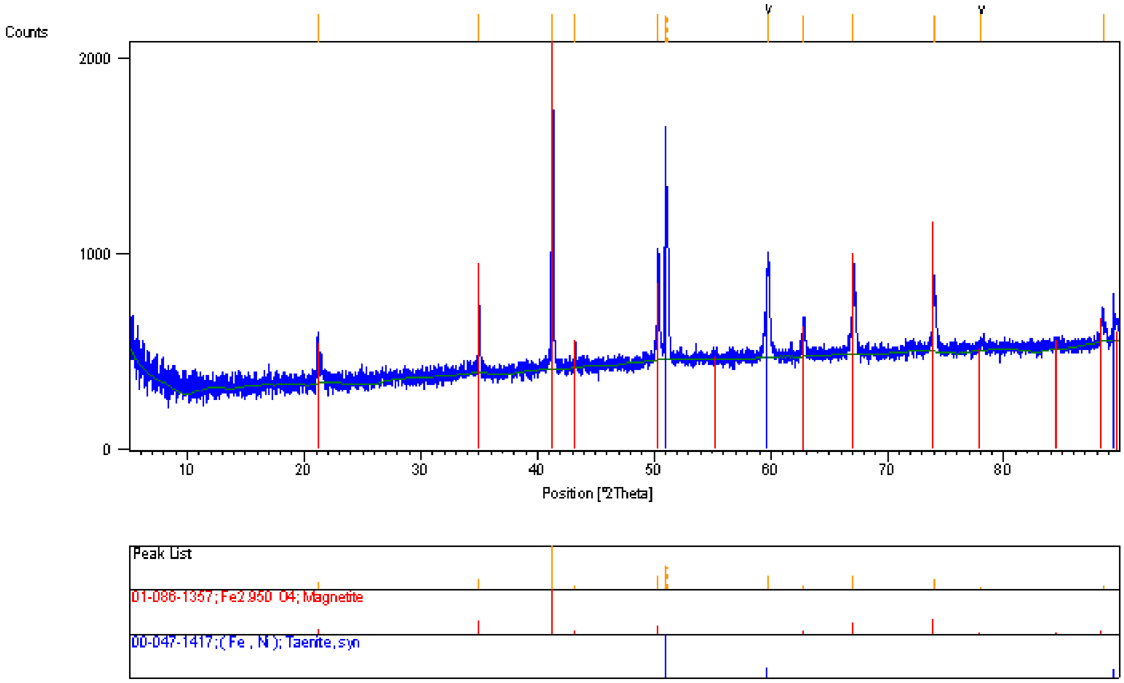

XRD pattern: residual scale after descaling top side of the uncontaminated sample D1. Main phases are spinel ("magnetite") and austenite ("taenite").

APPENDIX 4

XPS ANALYSIS OF THE SCALE FOR CHROMIUM QUANTIFICATION

XPS survey, multiplex and deconvolution analyses were performed on samples RP2, RP3, RP5 and RP8 for the determination of chromium oxidation state. Samples RP2 and RP3 were reheated at 1250°C, for 3h, 4% O_2 in gas (RP3 covered with flux type 832**;** C_f = 0.015 g/cm^2). Samples RP5 and RP8 (RP8 also covered with flux type 832; C_f = 0.015 g/cm^2) were reheated at 1280°C, for 6h, 4% O_2 in gas. The following XPS spectra give the results of the analyses performed on samples RP5 and RP8.

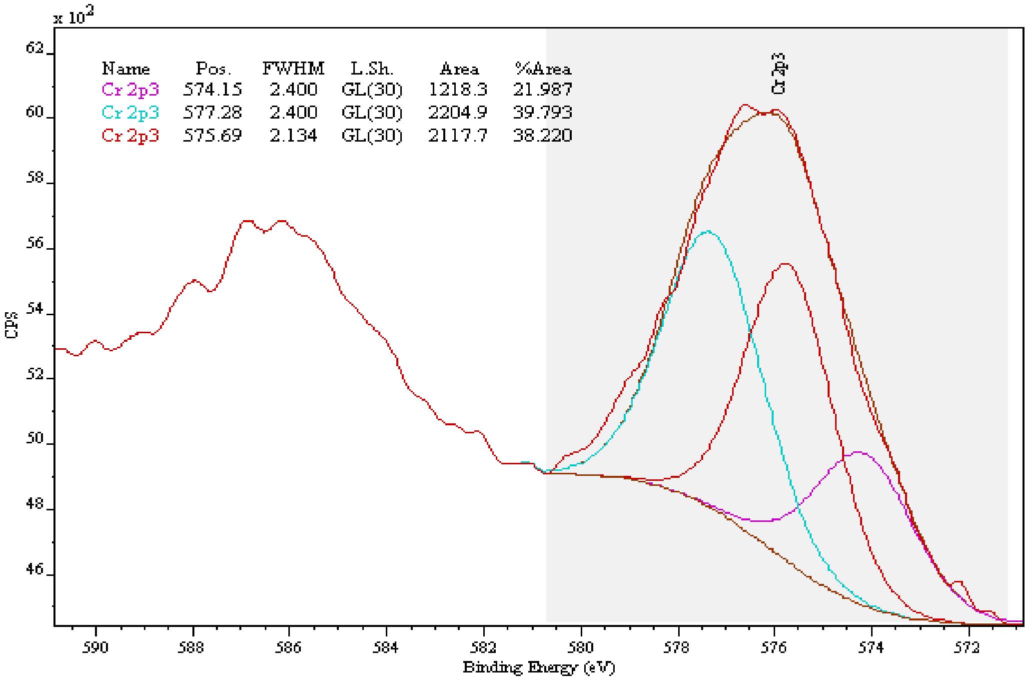

XPS deconvolution for chromium quantification of the uncontaminated sample RP5 reheated at 1280ºC, 4%O_2, for 6 hours

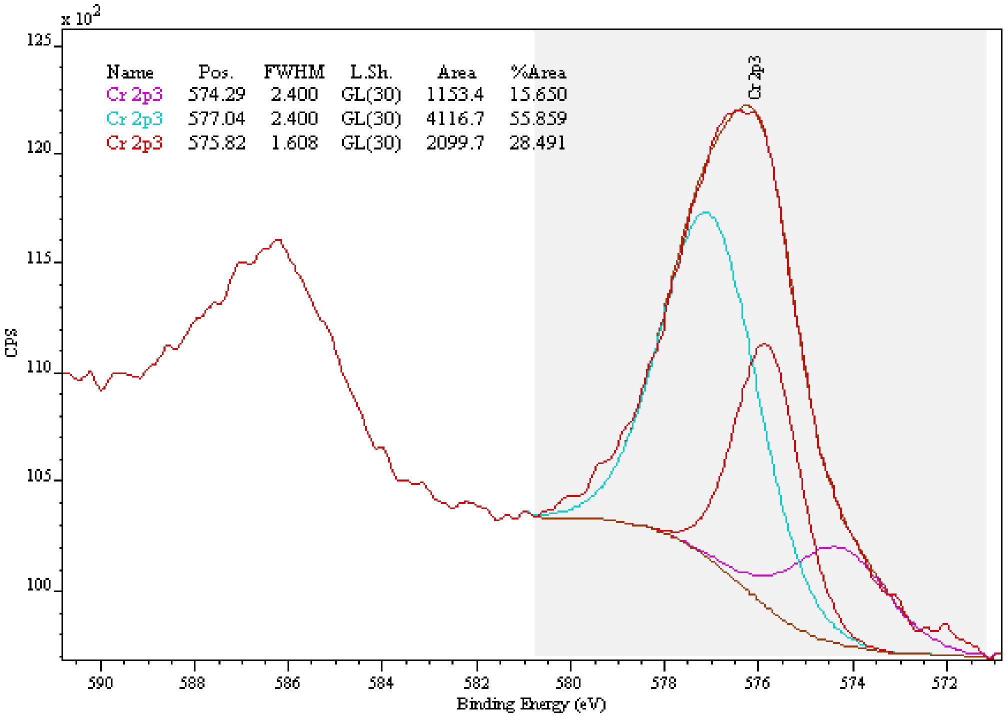

XPS deconvolution for chromium quantification of the contaminated sample RP8 reheated at 1280ºC, 4%O_2, for 6 hours

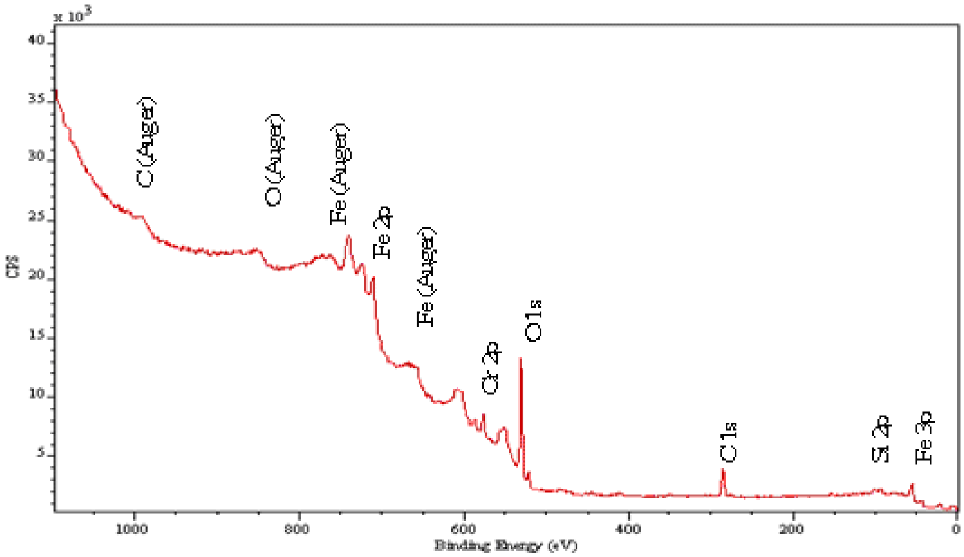

XPS Survey of the scale removed from the uncontaminated sample RP5 reheated at 1280ºC, 4%O_2, for 6 hours.

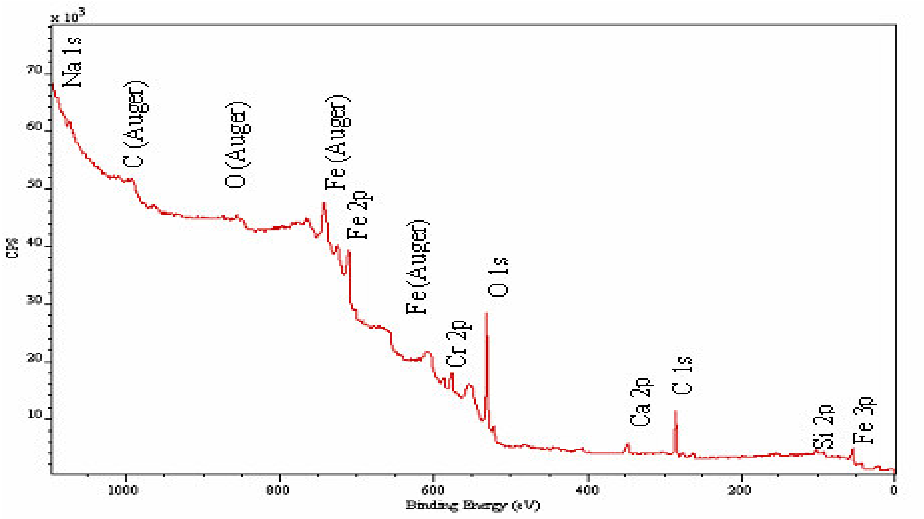

XPS Survey of the scale removed from the contaminated sample RP8 reheated at 1280ºC, 4%O_2, for 6 hours